7-11-2013

Investigating the Existence of Coherent Phonon Scattering in Silicon Using Phononic Crystals

Drew Goettler

Drew Goettler
Candidate

Mechanical Engineering
Department

This dissertation is approved, and it is acceptable in quality and form for publication:

Approved by the Dissertation Committee:

Zayd Leseman, Chairperson

Adrian Brearley

Chris Hall

Ihab El-Kady

Roy Olsson, III

INVESTIGATING THE EXISTENCE OF COHERENT PHONON SCATTERING IN SILICON USING PHONONIC CRYSTALS

by

DREW GOETTLER

B.S. Math and Astronomy, Drake University, 2001
M.S. Mechanical Engineering, The University of New Mexico, 2008

DISSERTATION

Submitted in Partial Fulfillment of the
Requirements for the Degree of

Doctor of Philosophy

Engineering

The University of New Mexico
Albuquerque, New Mexico

May, 2013

ACKNOWLEDGEMENTS

Sandia National Laboratories is a multi-program laboratory managed and operated by Sandia Corporation, a wholly owned subsidiary of Lockheed Martin Corporation, for the U.S. Department of Energy's National Nuclear Security Administration under contract DE-AC04-94AL85000.

I want to thank my advisor, Dr. Zayd Leseman, for presenting this opportunity to me. It was an honor to be one of his students and to learn from him. I appreciate his guidance and support. I also want to thank my committee members for their support as well. They provided advice, suggestions, and a deeper understanding of the material.

I am thankful for the financial support provided by Sandia National Laboratories. This work never would have happened without it. I also want to thank the staff at Sandia for their help as well.

There were many others along the way who helped me get to this point. A partial list includes: Ying-Bing Jiang, Mehmet Su, Charles Reinke, Khawar Abbas, Seyedhamidreza Alaie, Ron Salesky, and Mohammadhosein Ghasemi. Whether it was help with simulations, FIB/SEM support, collecting data, AFM support, or encouraging me when things were not going as planned, the help was appreciated and did not go unnoticed.

Without my wife’s support I would not be on this end of the dissertation. She was there for the joys, long working nights, and times of frustration. I am truly thankful for all she did.

I thank God for placing these amazing people in my path and providing strength.

INVESTIGATING THE EXISTENCE OF COHERENT PHONON SCATTERING IN SILICON USING PHONONIC CRYSTALS

by

Drew Goettler

B.S., Math and Astronomy, Drake University, 2001

M.S., Mechanical Engineering, The University of New Mexico, 2008

Ph.D., Engineering, The University of New Mexico, 2013

ABSTRACT

In silicon the majority of heat energy is transported by phonons, which are discrete lattice vibrations. Phonon scattering due to the presence of voids in silicon can further alter the material's thermal conductivity. There is a question about the possibility of some of this scattering being coherent rather than purely incoherent. Coherent phonon scattering is defined as constructive interference of phonons scattered from the inclusions in the phononic crystal. The intent of this work is to investigate the existence of coherent scattering in Si via phononic crystals. A phononic crystal is a periodic array of inclusions inside a host material. The inclusions could be a second material or a void. In this work five different supercell phononic crystals comprised of holes in silicon will be used to investigate the existence of coherent phonon scattering. Each of the supercells had nearly identical critical lengths in order to keep the amount of incoherent scattering equal among all of the PnCs. Porosity differences among the supercells were also minimized. All of

the PnCs were fabricated with a focused ion beam (FIB). During fabrication a protective layer of Ti was used to protect the Si from unintentional Ga doping from the FIB. The Ti layer also helped generate voids with more vertical sidewalls. A set of experiments was performed to measure the thermal conductivity of each PnC. Thermal conductivity measurements were carried out on a silicon nitride suspended island platform with platinum resistance temperature detectors and coated with aluminum nitride. A silicon slab was concurrently measured with each PnC, and relative thermal conductivity values were determined. The addition of the PnC decreased Si's thermal conductivity to less than 22% of its original value. An analysis of the results shows there is a reduction in thermal conductivity beyond the effects of porosity and incoherent scattering. This enhanced reduction in thermal conductivity is due to coherent phonon scattering in PnCs.

Table of Contents

Table of Figures

List of Tables

1. Introduction to Heat Flow Through Phononic Crystals (PnCs)

1.1. Phononic Crystal Applications

What is a phononic crystal? First, one needs to know what phonons are and what a crystal is in order to properly describe a phononic crystal, or PnC. First, let us start with a broad working definition for a phononic crystal to introduce the topic. Detailed descriptions of crystals and phonons will follow the introduction. A PnC is a piece of material that can manipulate mechanical vibrations. A considerable amount of theoretical and experimental work has been done with PnCs to actively control these mechanical vibrations over a wide range of frequencies and wavelengths. Devices such as waveguides [1, 2, 3], filters [4, 5, 6], cavities [7, 8, 9], focusing elements [10], cloaking [11], and support loss attenuators [12] demonstrate a few ways how people are using PnCs to manipulate mechanical waves. If the frequencies of the mechanical vibrations are in the radio frequency regime, then phononic crystals can be used to filter out or guide RF signals [13, 14].

There is also a lot of interest in using PnCs to manipulate the thermal transport of materials. Multiple groups have shown significant reductions in the thermal conductivity of Si using porous nano structures and PnCs [15, 16, 17, 18]. It has been hypothesized that by using phononic crystals, heat transfer can be minimized with minimal changes to electrical conductivity since the mean free path of electrons is less than the mean free path of phonons in Si [19, 20]. This opens up the possibility of exploiting thermoelectric effects in Si.

The thermoelectric effect occurs when 1) a temperature gradient across a material generates an electric potential or 2) when an electric potential generates a temperature gradient. A temperature gradient generating an electric potential is called the Seebeck effect, and a voltage generating a temperature gradient is called the Peltier effect[21]. How well a thermoelectric performs is determined by its figure of merit, *ZT*. *ZT* is a dimensionless figure of merit and is defined as[22]

$$ZT = \frac{\alpha^2 \sigma}{\kappa} T \qquad (1.1)$$

where α is a material's Seebeck coefficient, σ is electrical conductivity, κ is thermal conductivity, and T is temperature. A higher *ZT* value means that a material is more efficient at power generation or cooling. For a given material, decreasing its thermal conductivity without altering its Seebeck coefficient or electrical conductivity would increase its thermoelectric efficiency.

1.2. Introduction to Crystals

A crystal refers to a repeating structure with translational symmetry. The repeating structure is know as the basis[23], and the basis can range anywhere from a single atom to a tile array on a kitchen floor. In a crystal, the basis resides at discrete lattice points. It is important to note that the lattice points are not physical entities like the basis. Instead, the lattice points are mathematical representations used to describe the location of a basis. Each point in a lattice can be defined by a lattice vector, $\boldsymbol{R}$*, and in three dimensions (3D), the vector $\boldsymbol{R}$ is comprised of three vectors $\boldsymbol{a_1}$, $\boldsymbol{a_2}$, and $\boldsymbol{a_3}$[23].

* A note on notation: Vector variables are given a ***bold*** font. For example, $\boldsymbol{R}$ is the position vector while *n* refers to a scalar quantity.

$$\boldsymbol{R} = n_1\boldsymbol{a_1} + n_2\boldsymbol{a_2} + n_3\boldsymbol{a_3} \quad (1.2)$$

In **Equation (1.2)**, n_1, n_2, and n_3 are integers. For an m-dimensional crystal, m vectors, $\boldsymbol{a_m}$, are needed to describe $\boldsymbol{R}$. Any crystal generated with $\boldsymbol{R}$ will have translational symmetry. Also, the lattice will look the same at the lattice points described by $\boldsymbol{r}$ and $\boldsymbol{r'}$ if $\boldsymbol{r'} = \boldsymbol{r} + \boldsymbol{R}$[24].

Another important property of crystals is the unit cell. A unit cell, or primitive cell, contains a single lattice point, and it is a parallelepiped defined by the vectors $\boldsymbol{a_1}$, $\boldsymbol{a_2}$, and $\boldsymbol{a_3}$[23]. The unit cell is the smallest repeating structure of the crystal. Use of a unit cell facilitates easier comparison of various crystal structures.

A visual description of the ideas presented in the previous paragraphs is shown in **Figure 1.1**, which is a two-dimensional (2D) crystal. In **Figure 1.1a**, the black dots represent the lattice points generated by $\boldsymbol{R}$, which is comprised of the solid blue unit vectors $\boldsymbol{a_1}$ and $\boldsymbol{a_2}$.* Observation of the lattice from the lattice points indicated by the dashed blue vectors $\boldsymbol{r}$ and $\boldsymbol{r'}$ yield identical observations if there is an infinite array of points in the plane of the paper. Also shown in **Figure 1.1a** is the unit cell (gray box) generated by $\boldsymbol{a_1}$ and $\boldsymbol{a_2}$. It contains ¼ of each corner lattice point, and so the total number of lattice points in the unit cell is one. **Figure 1.1b** is the basis (a large and small red circle) for the 2D crystal shown in **Figure 1.1c**.

* Because all of the lattice points fall on the corners of squares whose edges are coincident, this lattice is commonly termed a 'square' lattice.

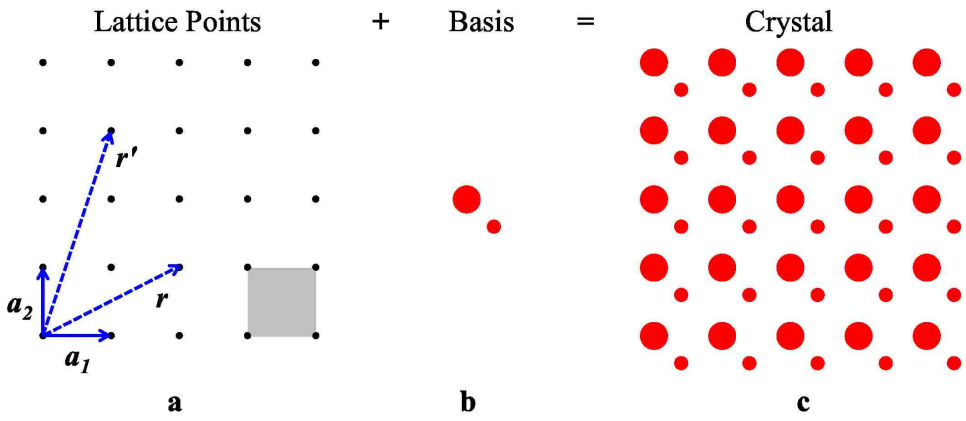

Figure 1.1: Description of a 2D crystal structure. a) Lattice points (black dots) generated by a_1 and a_2, which are the unit vectors of *R*. The lattice looks the same from the points described by vectors *r* and *r'*. The gray box represents the unit cell generated by a_1 and a_2. b) Basis for the crystal. c) Crystal generated by combining the lattice (a) and the basis (b).

All of the fabricated crystals in this work are based on a 2D square lattice, Repeating this lattice into the third dimension (in and out of the page) would create a simple cubic lattice. Some authors may refer to square lattices as simple cubic lattices. However it is more appropriate to call these 2D lattices, such as the one shown in **Figure 1.1a**, a square lattice. Additional details on the phononic crystal lattice and unit cells used for this work are discussed in Chapter 3.

1.3. Introduction to Phonons

Phonons, which can be classified as quasi-particles, are quanta of the vibrational modes of atoms in solids and in some liquids. On the atomic scale, one can think of a solid crystalline material as an interconnected network of masses and springs, where the masses are the atoms (or molecules) and the springs are the forces between neighboring atoms (or molecules). Transport of energy through the network of masses and springs occurs as oscillations – waves. On the atomic or quantum scale, there are discrete energy states, which means there are also discrete oscillations of the 'springs' between particles. These discrete, vibrational energy states are phonons.

At a given temperature, the particles in a material are vibrating at many frequencies. By summing up all of the discrete vibrations or phonons, one can determine the energy in the material. Since the phonons are frequency dependent, one can determine the energy by summing over all frequencies. Performing this summation requires knowledge of the phonon density of states and the phonon probability distribution. The density of states describes how the phonon states are distributed, and the phonon probability distribution describes the probability of a particular state being filled or occupied. By using a phononic crystal to change the phonons' density of states, silicon's thermal conductivity can be altered significantly [15, 17, 20, 25].

Phonons traversing a material will experience various interactions or scattering events. The two main categories are elastic scattering and inelastic scattering [26]. Elastic scattering events include lattice imperfections, dislocations, impurities, and boundaries. Elastic scattering preserves the phonon's frequency and energy. Inelastic scattering involves the interaction of three or more phonons, and the frequencies of the phonons are changed during inelastic scattering.

Most of these scattering events, both elastic and inelastic, are incoherent. Incoherent phonon scattering occurs when the scattering is not dependent on prior scattering events. With incoherent scattering, there is no correlation between the phonon's phase before and after scattering. Phonons scattering off impurities in a Si crystal is an example of incoherent scattering. Another example is phonons scattering diffusely off a rough surface. In Si at room temperature, the mean free path, *mfp*, between scattering events is around 300 nm [27], but there is evidence that phonons with longer mean free paths also contribute to Si thermal conductivity [21, 28, 29]. By increasing

the number of scattering events, one can inhibit the propagation of phonons across a material and reduce the material's thermal conductivity. Si is a good example. In its crystalline state, bulk Si has a thermal conductivity near 150 W/m-K [30, 31]. Amorphous Si, however, has a thermal conductivity near 2 W/m-K [32]. The same atoms are involved, but the amount of disorder in amorphous Si is much higher. Adding impurities, or dopants, such as phosphorus and boron, to crystalline Si is another way to reduce silicon's thermal conductivity [30, 33, 34]. The addition of impurities creates more phonon scattering events. A third way to reduce the thermal conductivity of Si is simply to reduce the thickness of the Si [27, 35]. By reducing the thickness of the material, there is an increase in the number of phonon-boundary scattering events.

Unlike incoherent phonon scattering, coherent phonon scattering is less understood [36]. Recent work on using periodic structures to alter the thermal conductivity in various materials, however, is starting to shed light on coherent phonon scattering [15, 17, 37, 38, 39]. In Reference 17, it is hypothesized that overlapping Bragg resonant frequencies in the ΓX and ΓM directions for a 2D square lattice of vias in Si open a bandgap in the allowable frequencies of the vibrational states and therefore prohibit propagation for a range of phonon frequencies. Reference 37, which also deals with vias periodically spaced in Si, proposes that the majority of the reduction in thermal conductivity of porous materials is associated with low frequency phonon scattering off the pore boundaries. Reference 38, which deals with alternating layers of AlAs and GaAs, observed measured thermal conductivity values that were consistent with a coherent phonon heat conduction process.

Before proceeding further, it is important to define what coherent phonon scattering means. When waves are described as coherent, this typically implies that the waves have the same wavelength (monochromatic) and are in phase with one another. When dealing with heat conduction in Si, there is a broad frequency, or wavelength, range of phonons that contribute to heat transfer, so it is not appropriate to think of coherent phonon scattering in the same manner. In Reference 38, coherent phonon heat conduction was investigated in a superlattice (SL) of GaAs and AlAs. In the article the key question for heat conduction was whether to treat each interface in the SL as a diffuse boundary (incoherent phonon transport) or to treat the entire superlattice as a new material with its own phonon dispersion caused by the interference of phonon waves propagating through the whole structure (coherent phonon transport) [38]. Although various types of scattering may occur within the periodic material (superlattice, phononic crystal, etc.), the fact that periodicity is present alters the phonon propagation through the material. Hopkins et al. also put this idea forth in their earlier work on Si/air PnCs [15]. The reduction in silicon's thermal conductivity beyond the effect of porosity and diffuse scattering at pore boundaries was attributed to the coherent phononic effects of the periodically porous structure [15]. In effect, coherent phonon scattering occurs when the scattering of phonons is dependent on previous scattering events. Coherent phonon scattering is defined as constructive interference of phonons scattered from the inclusions in the phononic crystal.

The intent of this work is to further investigate the existence of coherent phonon scattering in silicon using phononic crystals by observing changes in the thermal conductivity of Si/Air PnCs. If coherent scattering does exist, then it will be possible to

see its effects by observing the thermal conductivity of various unique phononic crystals. Coherent scattering occurs when periodicity is present, and all crystals have periodicity. If the scattering of the phonons is purely incoherent, then adding in the periodicity of the phononic crystal will not alter the thermal conductivity.

To study the coherent effect, a series of thermal conductivity measurements were performed on Si with various PnC patterns. These PnCs have length scales on the order of the mean-free-path length of phonon-phonon interactions in Si at room temperature. Fabricating PnCs with this length scale was accomplished with the use a focused ion beam. Details on the PnC patterns and the fabrication process are discussed in the following chapters.

2. Description of PnCs to be Used for Investigating Coherent Phonon Scattering

The focus of this chapter is to describe the unit cells used to investigate the existence of coherent phonon scattering in silicon. The choice of unit cells was based on the ability to distinguish the potential effect of coherent scattering on thermal conductivity from other factors that can affect thermal conductivity such as critical length and porosity. Critical length is the minimum feature size of the unit cell, and porosity is a measure of the amount of material removed. The first part of the chapter provides reasoning for the unit cells that were ultimately chosen. In the latter half of the chapter are design considerations and design constraints.

2.1. Choice of Proper Unit Cells

In order to investigate the existence of coherent phonon scattering, it was necessary to use multiple unique crystals with similar characteristics. Since coherent scattering requires periodicity, which is a characteristic of crystals, multiple crystals were required to show a distinct trend. With only one or two crystals, it is possible to draw multiple different conclusions, none of which would be definitive. As the number of different unit cells increases, a distinct and unique trend can emerge from the data. Besides being unique, all of the crystals required similar characteristics such as porosity and critical length. Both of these characteristics affect a material's thermal conductivity [15, 17, 27, 28, 40]. If the unique crystals did not have similar critical lengths and porosities,

then it would have been impossible to distinguish the effect of the crystal from the other effects.

The first step in choosing the proper unit cells was deciding which lattice types to use. Previous work that looked at the difference in thermal conductivity between two different 2D lattices, square lattice and hexagonal, stated thermal conductivity was insensitive to pore alignment [28]. Since that work suggested there was no difference in thermal conductivity between the square lattice and hexagonal unit cell, another set of unit cells was needed that could potentially show a measurable difference. Ideally the unit cells would have no variation in the critical length and porosity, and a square lattice with a center point allowed for these to occur. By adding in a small via to the center of the square lattice, it was possible to achieve a length along the diagonal that was equal to the minimum distance between two large vias. Also, adding a small via created minimal porosity variations.

Five different two-dimensional (2D) unit cells based on the square lattice design along with their associated names are shown in **Figure 2.1.** The black regions of **Figure 2.1** are the areas to be etched into the Si samples to create the interpenetrating vias or inclusions. Differences among the unit cells are the number of interpenetrating vias. These perturbations of the square lattice unit cell generated various supercells, which became the new unit cells. All of the length definitions are shown in **Figure 2.2**. The variable, a, represents the horizontal and vertical center-to-center spacing (or pitch) between the large vias, d_1 (r_1) is the diameter (radius) of the large via, d_2 (r_2) is the diameter (radius) of the smaller interpenetrating via, c_v is the critical length between two large vias, and c_x is the critical length along a diagonal line between a large and small via.

Ideally, c_y and c_x are equal. By keeping the critical length constant in all of the unit cells, a comparison of the measured thermal conductivity measurements will be independent of the critical length. **Table 2.1** lists all of the unit cells along with their dimensions and corresponding porosities. Details on the various relationships among different length definitions and porosity calculations are discussed in the latter portion of this chapter.

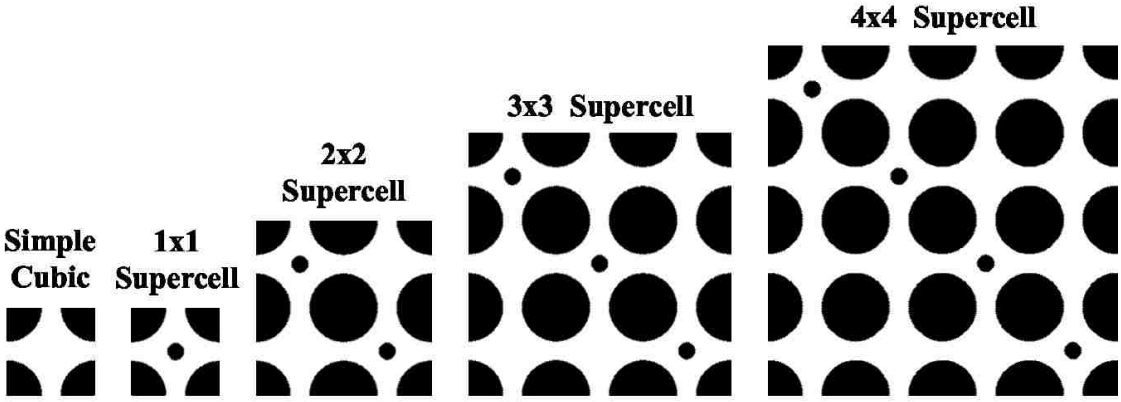

Figure 2.1: Images and names of unit cells used to investigate the existence of coherent phonon scattering. Black circles represent the vias or air holes in Si. All of the supercells are based on a 2D square lattice.

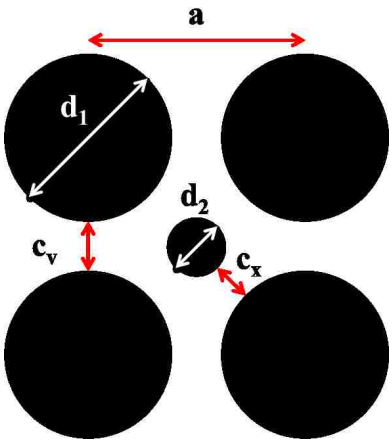

Figure 2.2: Length definitions for supercells. *a* is the pitch, d_1 is the diameter of the large via, d_2 is the diameter of the smaller interpenetrating via, c_y is the critical length between two large vias, and c_x is the critical length along a diagonal line between a large and small via. Ideally, c_y and c_x are equal.

Table 2.1: List of all five unit cells with the desired dimensions and porosities in 2D.

Unit Cell	a (μm)	d_1 (μm)	d_2 (μm)	c_v (μm)	c_x (μm)	2D Porosity ϕ
Square lattice	1.1	0.85	0.206	0.25	0.25	0.469
1x1 Supercell	1.1	0.85	0.206	0.25	0.25	0.497
2x2 Supercell	1.1	0.85	0.206	0.25	0.25	0.483
3x3 Supercell	1.1	0.85	0.206	0.25	0.25	0.478
4x4 Supercell	1.1	0.85	0.206	0.25	0.25	0.476

2.2. Rationale for Critical Length and Porosity

After choosing the basic structure of the unit cells and supercells, the next step was determining the dimensions such as the pitch and critical length. Multiple reasons existed for choosing the supercell dimensions listed in **Table 2.1**. First, previous work showed that a two-dimensional square lattice of air holes in Si with difference lattice constants and diameters showed a decreased in the thermal conductivity of bulk Si [15, 17, 25]. For a given critical length, an increase in the lattice constant decreased the thermal conductivity of Si [17, 25]. Based on this, a lattice spacing of 1.1 μm should show a further decrease in silicon's thermal conductivity.

One dimension not listed in **Table 2.1** is thickness. In order for the critical lengths c_v and c_x to be the true critical lengths, they must describe the minimum feature size. This required the thickness to be larger than the spacing between vias. The thickness, though, was small enough for the PnCs to resemble a 2D surface. Each supercell had a thickness near 366 nm, which is more than 100 nm greater than the desired 250 nm critical length.

Determination of the critical length was based on the mean free path of phonons in Si near room temperature. At 300 K the phonon mean free path in Si is near 0.3 μm [27]. If the critical length of the pattern is much larger than the phonon mean free path, then

the phonons would simply traverse the PnC without scattering off the inclusions. If the critical length is much smaller than the phonon mean free path, the critical length rather than the PnC pattern will dominate the heat flux. In another reference calculations were performed to estimate the cutoff mean free path, L_p, responsible for a percentage, *p,* of the total heat flux for bulk silicon and a 1 μm nanowire [41]. A plot of L_p for various percentages (10, 50, and 90) as a function of temperature is shown in **Figure 2.3**. The vertical gray rectangular line is drawn at a temperature of 300 K, which is near the temperature at which the experiments for this dissertation were performed. According to Reference 41, phonons with mean free paths up to 0.25 μm (horizontal line in Figure 2.3) at 300 K account for between 10% and 50% of the heat flux in bulk Si and between 50% to 90% of the heat flux in a 1 μm nanowire (NW). Although the graph in **Figure 2.3** does not show a plot for a 2D structure, it is assumed a 2D structure would follow similar trends as the 3D bulk Si and 1D 1 μm NW since the graph is based on incoherent boundary scattering [41] and not a function of the dimensionality of the structure being measured. Dames et al. indicate in their work that further lowering the critical dimension of the nanowire would only serve to increase the contribution of phonons with mean free paths of 0.25 μm or less. This suggests the thermal conductivity of a PnC with a critical length of 0.25 μm will be highly influenced by phonons with a mean free path of similar size. Thus, it is important that all of the unit cells have equal critical lengths. Since the critical length of each unit cell in this study is the same, the critical length will equally influence each unit cell and can be neglected when comparing thermal conductivity values amongst the unit cells.

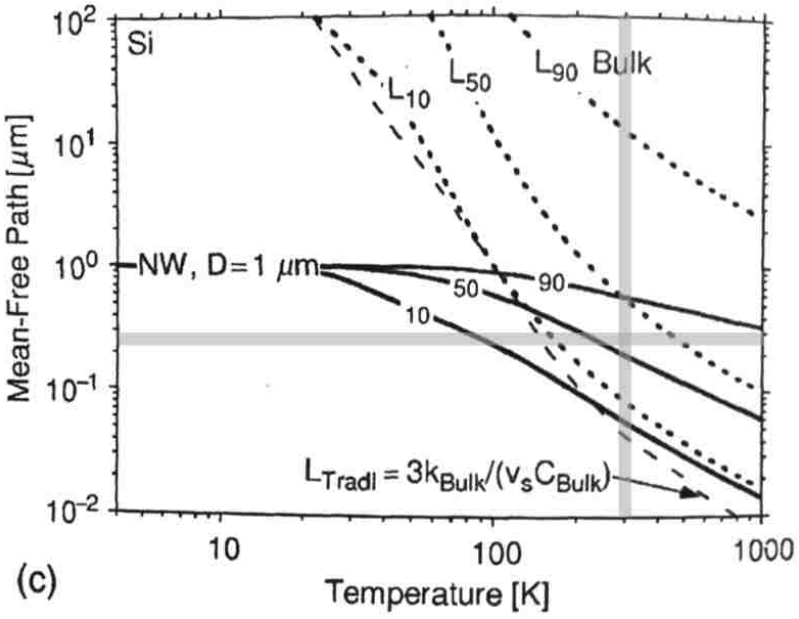

Figure 2.3: Temperature dependence of the important mean free paths for bulk Si and a 1 μm nanowire. Vertical gray line drawn at 300 K and horizontal gray line drawn at 0.25 μm. L_p represents a cutoff mean free path that accounts for a percentage p of the total heat flux (Image taken from Chptr. 42 of Thermoelectrics Handbook edited by Rowe)[41].

Once the unit cells and critical lengths were determined, porosity values were set. Minimal porosity differences among the unit cells were more important than having a specific porosity value. It is known that removing material causes a decrease in thermal conductivity[42, 43, 44]. If the porosities of the unit cells are similar, then a comparison of the measured thermal conductivity values will also be independent of the porosity or at least have minimal dependence on porosity. Based on the unit cells and chosen critical length, there is a 2.8% maximum porosity difference among the unit cells.

2.3. Unit Cell Simulations

After choosing a set of unit cells and a critical length, simulations were run to see if there were differences in the density of states calculations for the square lattice and the supercells[25]. A crystal's density of states is one factor that affects its thermal conductivity. Chapter 3 provides details on various methods for calculating thermal

conductivity. Calculating the density of states is based on the work performed in Reference 25. In the work by Reinke et al. [25], the density of states was calculated by combining results from a lattice dynamics simulation and plane wave expansion analysis. Coherent scattering in the model is accounted for by using the dispersion calculated from plane wave expansion. In the analysis diffuse boundary scattering was taken into account, and it was dependent on the minimum feature length/critical length of the PnC.

Results from the simulations are shown in **Figure 2.4**. In this figure green represents the square lattice unit cell, and blue represents the unit cell being compared to square lattice. The graphs in **Figure 2.4** show the density of states integrated over frequency. Differences between the blue and green plots indicate a difference in the density of states for the various unit cells and thus a difference in the calculated thermal conductivity values. Both plots show similar results for high frequency and extremely low frequency phonons. At high frequencies, the wavelengths are short enough that the effect of the PnC is negligible. For extremely low frequency phonons, the wavelengths are long enough that the effect of the PnC is negligible.

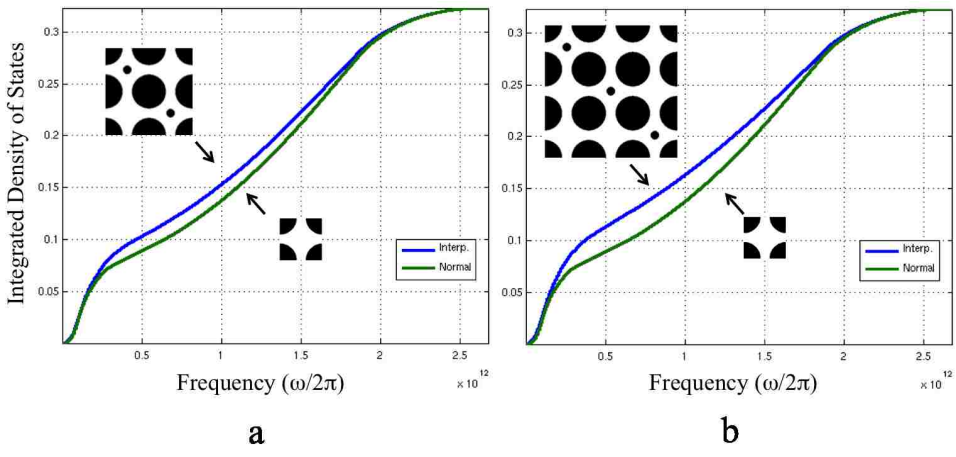

Figure 2.4: Integrated density of states calculations for the 2x2 supercell (a) and 3x3 supercell (b). Green line in both plots is for the square lattice while the blue line is for their respective supercells.

2.4. Length Definition Relationships and Porosity Calculations

All five unit cells were designed to have the same critical length between two large vias and between a large and small via (interpenetrating hole). The geometric relationships among the pitch, diameters, and the critical lengths are shown in the following three equations.

$$c_x = c_v = c \quad \textbf{(2.1)}$$

$$a = c + d_1 \quad \textbf{(2.2)}$$

$$\sqrt{2}a = d_1 + d_2 + 2c \quad \textbf{(2.3)}$$

With five unknowns and only three equations, two of the dimensions must be specified to determine the other two lengths.

As stated previously, porosity is an important geometrical parameter that affects thermal conductivity. Porosity is a measure of the amount of material removed, and it is defined as the ratio between the inclusions' area (volume) and the area (volume) of the unit cell with no inclusions. Since different units cells with the same critical length were used, it was impossible to keep the porosity constant. By using a relatively small interpenetrating via, the porosity difference among the unit cells was minimized. A comparison among the 2D porosities shows a maximum difference of 2.8% among all five unit cells. A list of equations for the various two dimensional filling fractions are shown in **Equations (2.4)** and **(2.5)** where r_1 and r_2 are the radii corresponding to diameters d_1 and d_2 . In **Equation (2.5)**, N represents the NxN supercell.

Square lattice $$\frac{\pi r_1^2}{a^2} \quad \textbf{(2.4)}$$

NxN Supercell $$\frac{\pi(Nr_1^2 + r_2^2)}{Na^2} \quad \textbf{(2.5)}$$

Porosity in three dimensions, which takes into account the thickness of the unit cell, follows a similar trend to that in two dimensions, but there is a difference in the porosity due to slanted sidewalls, which caused a deviation from a cylindrical hole to a frustum. This slight sidewall slant arose from the method by which the PnCs were fabricated. Details on fabrication are in Chapter 3. A list of equations for the various three dimensional filling fractions are shown in **Equations (2.6)**and **(2.7)**.

Square lattice $$\frac{\pi(R_1^2 + R_1 r_1 + r_1^2)}{3a^2} \quad \textbf{(2.6)}$$

NxN Supercell $$\frac{\pi[N^2(R_1^2 + R_1 r_1 + r_1^2) + N(R_2^2 + R_2 r_2 + r_2^2)]}{3(Na)^2} \quad \textbf{(2.7)}$$

In these two equations, the thickness is absent due to both the volume of the vias and silicon slab being linearly dependent on thickness. All of the variables are represented in **Figure 2.5**.

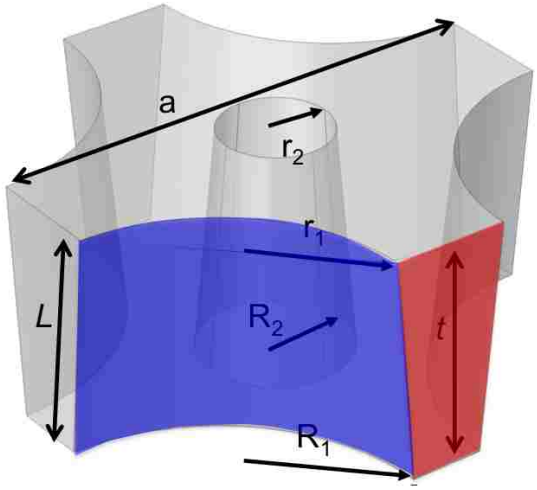

Figure 2.5: 3D diagram of a 1x1 supercell in 3D. All of the various dimensions used to calculate porosity in 3D are shown. Tapered sidewalls are due to fabrication technique. Blue region highlights sidewall surface area, and red region indicates trapezoidal area between the large vias.

A graphical representation of the various 2D porosities (black lines) is shown in **Figure 2.6**. In this plot, the *x*-axis represents the diameter of the large via, d_1, normalized

to the pitch, a. Using the dimensions listed in **Table 2.1**, d_1 is 0.77a. When d_1 is less than or equal to 0.77a, there is less than a 2.8% difference in the porosity (black y-axis on left side) among the various unit cells. **Figure 2.6** also plots the critical length, c, and the smaller via diameter, d_2, as a function of d_1. The blue y-axis on the right side plots c and d_2 normalized to a.

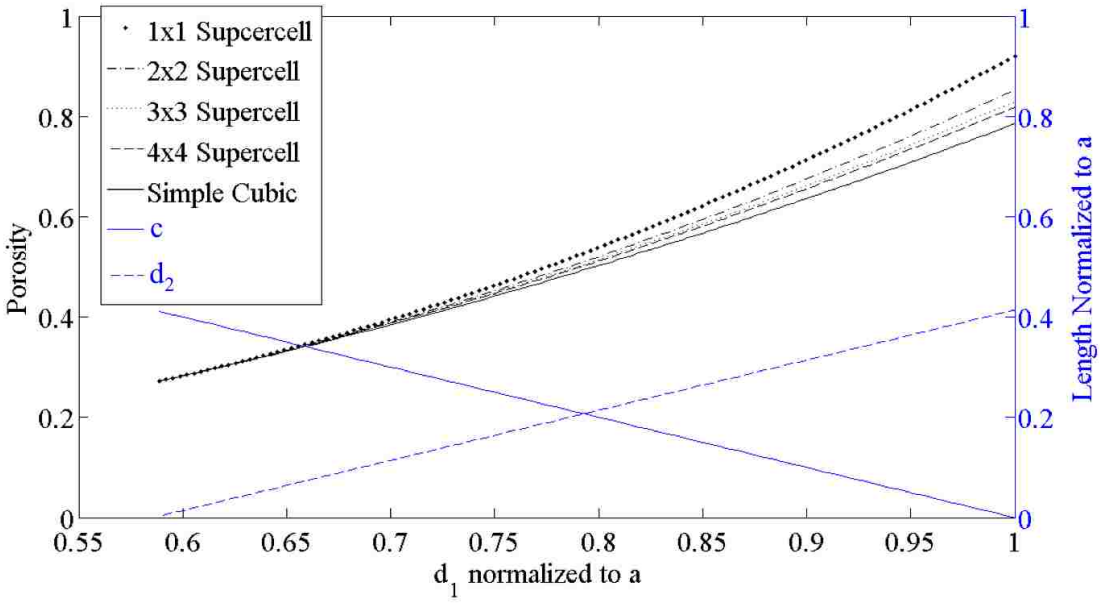

Figure 2.6: Comparison of filling fractions and limiting dimensions as a function of d_1 (large vias) for supercell patterns. Black lines represent filling fractions, and blue lines represent limiting cases for c (critical length) and d_2 (small vias).

Fabricating a PnC with a small critical length, c, or a small interpenetrating via diameter, d_2, is difficult. Smaller focused ion beam currents allow smaller vias to be milled, but the time required to mill each pattern increases, which also increases the chance for error. Another fabrication limitation is the via's aspect ratio, which is the ratio between the via's depth and diameter. The maximum aspect ratio for Si is 5:1 [45], but at this ratio the via resembles a frustum rather than a cylinder. Thus, one wants to fabricate a PnC where both c and d_2 are maximized to ease fabrication constraints. This was one reason the PnCs had both the critical length and interpenetrating via diameter close to

0.21a (this corresponds to d_1 equal to 0.79a), which is where the critical length and diameter of the interpenetrating via intersect. The FIB used for this research is capable of milling material with an ion beam that has a beam diameter of 7 nm at the Full Width at Half of the Maximum (FWHM). With such a small milling beam, achieving 250 nm for the critical length was realistic.

2.5. Surface Area

At first sight it appears there is an increase in the amount of surface area as one progresses from the 4x4 supercell to the 1x1 supercell. If surface area were considered as a measure of the amount of boundaries available for incoherent scattering, one would mistakenly use that as a plausible explanation for the observed reduction in thermal conductivity. While this is a valid observation, it is, however, incorrect for the following reasons. 1) The analytical expressions for the porosity prefactor as derived in References 42, 43, and 44 account for the shape, volume, and surface area of the scatterers. 2) In the fabricated samples there is an overall net loss of surface area with respect to a slab of equal thickness. Thus, if one were to rely on the surface area as a measure of the incoherent strength it would yield a larger thermal conductivity value for the perforated slab as compared with the unpatterned slab, which is not the case.

In general incoherent scattering is affected by two main characteristics of the scatterer: 1) its geometrical shape and size and 2) the edge-to-edge separation between neighboring scattering centers. The first is accounted for in a porosity prefactor that multiplies the intergral of **Equation (3.8)**, and the second is accounted for by the critical dimension, c, which is used in the incoherent scattering lifetime, τ. τ is equal to v/c,

where v is the phonon group velocity [25, 46]. Any further attempts to account for surface area would overestimate its actual effect.

Next it is shown that the addition of the supercells results in an overall decrease in surface area. When cylindrical holes are added to a slab of material, the change in surface area is dependent on the relationship between the slab's thickness, t, and the via's radius, r_1. The change, though, is not always positive or negative. For a slab or a plate with length l, width w, and thickness t, the total surface area, A, is the sum of the top surface, bottom surface, and the four sides (**Figure 2.7a**).

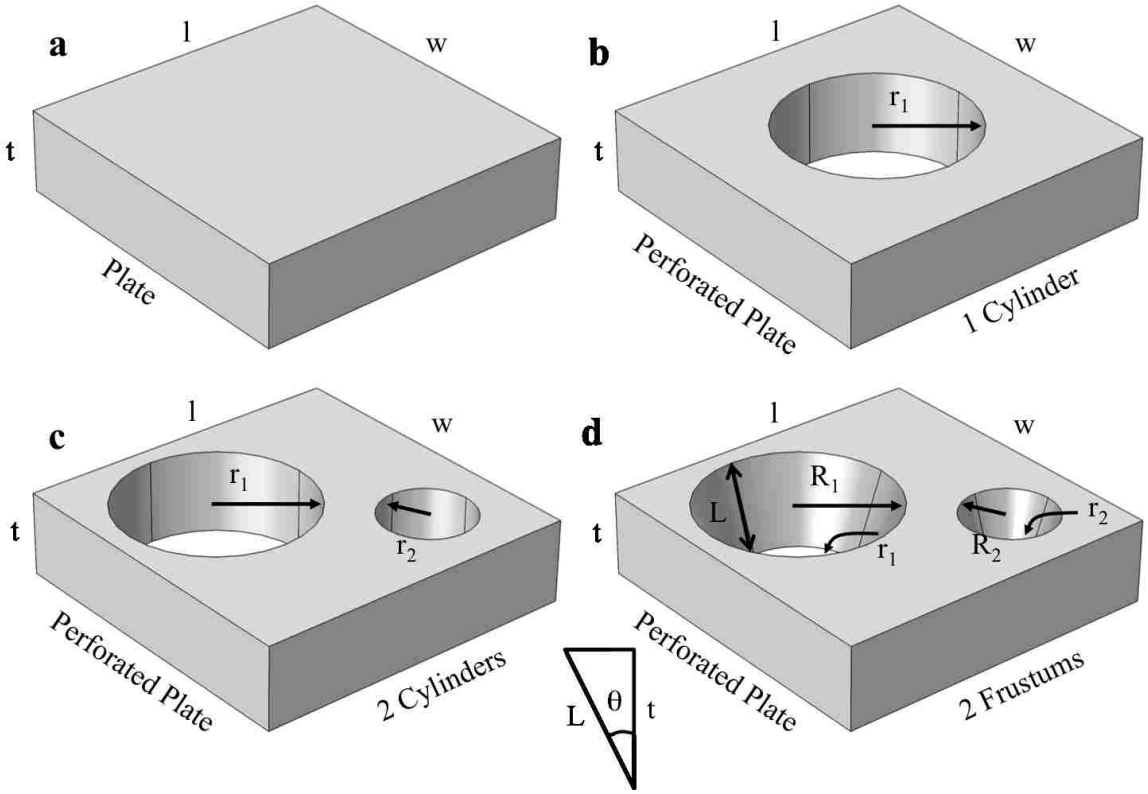

Figure 2.7: Progression of surface area calculation for supercells with frustums. a) Plate of material with no holes. b) Plate of material with a single cylindrical hole. c) Perforated plate with holes having different radii. d) Use of frustums rather than cylinders.

The surface area of the plate is

$$A_{plate} = 2(lw + lt + wt) \quad \textbf{(2.8)}$$

When a cylindrical hole is generated in the plate (**Figure 2.7b**), the surface area of the perforated plate will increase, stay the same, or decrease depending on the relationship between r_1 and t. For the perforated plate shown in **Figure 2.7b**, the surface area becomes

$$A_{perforated} = 2(lw - \pi r_1^2 + wt + lt + \pi r_1 t) \quad \textbf{(2.9)}$$

Now assume $l = w = a$. The surface area for the plate becomes

$$A_{plate} = 2(a^2 + 2at) \quad \textbf{(2.10)}$$

and the perforated plate's surface area is

$$A_{perforated} = 2(a^2 - \pi r_1^2 + 2at + \pi r_1 t) \quad \textbf{(2.11)}$$

By setting the surface area of the plate equal to the surface area of the perforated plate, the relationship reduces to

$$r_1 = t \quad \textbf{(2.12)}$$

When $r_1 < t$, the perforated plate has more surface area than the non-perforated plate, but when $r_1 > t$ the perforated plate contains less surface area.

Most of the unit cells in this study have two holes with different radii. When a second cylindrical hole with radius, r_2, is added, an attempt to find a convenient relationship among A, r_1, r_2, and t becomes non-trivial since there are now more variables than equations. **Figure 2.7c** shows a perforated plate with cylindrical holes having different radii. If the surface area of the plate is set equal to the surface area of a perforated plate with two holes, the relationship becomes

$$\frac{r_1^2 + r_2^2}{r_1 + r_2} = t \quad \textbf{(2.13)}$$

Equation (2.13) **is not useful unless additional information is known. Using the desired radii calculated from**

Table 2.1, the surface areas are equal when t = 362 nm. If the left side of **Equation (2.13)** is less (greater) than 362 nm, then the surface area of the perforated plate becomes less (greater) than the plate without holes.

Besides having two different radii (not including the square lattice case), the fabricated vias were frustums rather than cylinders (**Figure 2.7d**). Calculating the three-dimensional surface area of the various unit cells now becomes a summation of the top surface, bottom surface, four sides, and the sidewall areas of the frustums. For the perforated plate with frustums shown in **Figure 2.7d**, the surface area becomes (assuming $l = w = t$)

$$A_{frustums} = 2a^2 - \pi(R_1^2 + r_1^2 + R_2^2 + r_2^2) + 4at + \pi L(R_1 + r_1 + R_2 + r_2) \quad \textbf{(2.14)}$$

Setting the surface area of the plate equal to the surface area of the perforated plate with frustums results in

$$\frac{R_1^2 + r_1^2 + R_2^2 + r_2^2}{R_1 + r_1 + R_2 + r_2} = \frac{t}{\cos\theta} \quad \textbf{(2.15)}$$

Using the desired radii calculated from **Table 2.1**, the surface areas are equal when t = 368 nm, which is a slight increase from the perforated plate with cylindrical holes.

Surface area calculations for the supercells follow a similar approach, but instead of all vias located in the interior portion of the plate, some of the larger vias are located along the plate's edge. Now the surface area is the summation of the top surface, the bottom surface, the frustum's sidewall, and the trapezoidal areas between the large vias. **Figure 2.5** shows the various regions of a 1x1 supercell surface. Blue represents a

portion of the frustum's sidewall, and red represents the trapezoidal area between the large vias. The total surface area is then divided by the area of a Si slab with the same unit cell size to achieve a relative surface area, A_s. For the square lattice unit cell, the relative surface area, A_{sc}, is given by **Equation (2.16)**. All of the variables are represented in **Figure 2.5**.

$$A_{sc} = \frac{2a^2 - \pi(R_1^2 + r_1^2) + 4t(a - R_1 - r_1) + \pi L(R_1 + r_1)}{2a^2 + 4at} \quad \textbf{(2.16)}$$

For the supercells a generalized formula for the normalized surface area is given in **Equation (2.17)**. In this equation, N represents the NxN supercell.

$$A_{NxN} = \frac{2(Na)^2 - N\pi(NR_1^2 + Nr_1^2 + R_2^2 + r_2^2) + 4Nt(a - R_1 - r_1) + N\pi L(NR_1 + Nr_1 + R_2 + r_2)}{2(Na)^2 + 4Nat} \quad \textbf{(2.17)}$$

In each of the unit cells used for this work, the normalized surface area was less than one. In the limiting case, $\lim_{N\to\infty} A_{NxN} = 0.923$. Thus, it is not possible to increase the surface area relative to the slab with a given thickness of 366 nm. A graphical representation of the normalized surface area as a function of supercell size is shown in **Figure 2.8**. As the size of the supercell increases, the normalized surface area asymptotically approaches the limit of 0.923. This means adding the vias to the unit cell decreased the overall surface area.

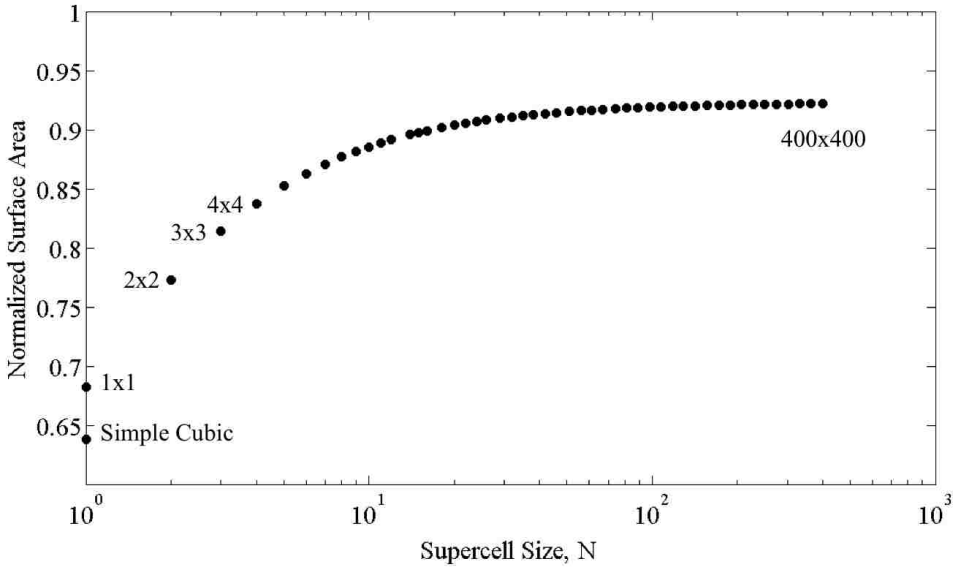

Figure 2.8: Graphical representation of the normalized surface area for NxN supercells. As the size of the supercell increases, the normalized surface area approaches the limit of 0.923.

In summary, these five unit cells with their corresponding dimensions allowed for a comparison of thermal conductivity values that was independent of the critical length and porosity. Previous work predicted that a lattice constant of 1.1 μm would provide further reduction in Si's thermal conductivity. A critical length of 0.25 μm is comparable to the mean free path of phonons in Si at 300 K, and calculations showed that phonons with mean free paths up to 0.25 μm account for a significant percentage of the total heat flux in Si. Last, the dimensions were achievable with the equipment available.

3. Modeling Thermal Conductivity of Phononic Crystals

This chapter focuses on describing various methods for predicting the thermal conductivity of phononic crystals. Each method can be traced back to the Boltzmann Transport Equation (BTE). A framework for how to get from the BTE to the various methods is provided, and details can be found in the references. In the last portion of this chapter, results from COMSOL, a finite element software package, will be presented.

3.1. Boltzmann Transport Equation and Callaway-Holland Model

Estimating the thermal conductivity of a phononic crystal in silicon can be performed by determining how the phonon distribution in the PnC evolves. Since thermal energy in Si is mainly transported by phonons, only the phonons are considered. A general equation for describing how a distribution of particles evolves and changes is the Boltzmann Transport Equation (BTE). By thinking of the phonons as particles, it is then possible to describe a distribution of the phonon "particles". A general form of the BTE is given by [36]

$$\frac{df}{dt} + \frac{d\boldsymbol{r}}{dt} \cdot \boldsymbol{\nabla}_{\boldsymbol{r}} f + \frac{d\boldsymbol{p}}{dt} \cdot \boldsymbol{\nabla}_{\boldsymbol{p}} f = \left(\frac{df}{dt}\right)_{scat} \quad (3.1)$$

where $f(\boldsymbol{r},\boldsymbol{p},t)$ is a distribution function of the particles and it is dependent on the distribution's position vector, $\boldsymbol{r}$, its momentum vector, $\boldsymbol{p}$, and time, t.* The terms on the left can be classified as drift terms, and the term on the right is the scattering term [26]. The terms on the left describe how the distribution changes with time, how it changes as a function of position, and how it changes as a function of momentum. If the particles

* A note on notation: Vector variables are given a ***bold*** font. For example, $\boldsymbol{v}$ is the velocity vector while v would be considered a scalar quantity.

experienced no collisions, then there would be no change in the distribution; it would be conserved. With collisions, however, the change in the distribution is equal to the scattering term on the right side of the equation.

The scattering term on the right of **Equation (3.1)** describes how the particle distribution changes over time due to collisions or scattering. This term can be thought of as the net rate of gaining particles at point (***r, p***) [36]. It is a difficult term to solve, and is typically replaced by a relaxation time approximation that describes how long it takes for a distribution in non-equilibrium to return to equilibrium [36]. A common way to determine the relaxation time approximation is by summing up reciprocal relaxation times for various processes [47]. This assumes that various processes are occurring in parallel at the same time and are independent of each other.

In order to get the BTE into a more useable form, additional assumptions are made. One assumption is to neglect the transient term, (*df/dt*), and treat the BTE as a steady state equation. When considering heat conduction by phonons, there is no external force, so the ***dp****/dt* term can be neglected as well. The simplified BTE now looks like

$$f = f_o - \tau \boldsymbol{v} \cdot \boldsymbol{\nabla} f_o \qquad \textbf{(3.2)}$$

where f_o is the Bose-Einstein distribution. Since the Bose-Einstein distribution depends on temperature, which is a function of position, ***r***, **Equation (3.2)** can be written as

$$f(\boldsymbol{r}, \boldsymbol{k}) = f_o - \tau \frac{df_o}{dT} \boldsymbol{v} \cdot \boldsymbol{\nabla} T \qquad \textbf{(3.3)}$$

By combining the BTE shown in **Equation (3.3)** with an expression for heat flux, one can derive an expression for thermal conductivity. For simplicity, consider the

heat flux passing through a plane in the *x*-direction. The heat flux in the *x*-direction, q_x, is given by

$$q_x = \sum_s \left[\frac{1}{V} \sum_{k_x} \sum_{k_y} \sum_{k_z} v_x \hbar \omega f \right] \quad \textbf{(3.4)}$$

In **Equation (3.4)**, the first summation takes place over all phonon polarizations, *s*. The remaining three summations are for indexing over all wave vectors. By transforming **Equation (3.4)** into an integral (assuming small spacing between adjacent *k*-states) and rearranging the terms, the heat flux is now

$$q_x = -\frac{dT}{dx} \left(\frac{1}{2\pi} \right)^3 \sum_s \int C v^2 \tau d\boldsymbol{k} \quad \textbf{(3.5)}$$

In **Equation (3.5)**, $C = \hbar \omega \frac{df_o}{dT}$, and is expressed in Joules per Kelvin. By combining terms, **Equation (3.5)** can be expressed as Fourier's Law in one-dimension (*x*-direction).

$$q_x = -\kappa \frac{dT}{dx} \quad \textbf{(3.6)}$$

In **Equation (3.6)**, κ is the thermal conductivity and is given by

$$\kappa = \left(\frac{1}{2\pi} \right)^3 \sum_s \int C v^2 \tau d\boldsymbol{k} \quad \textbf{(3.7)}$$

which is one form of the Callaway-Holland model.

The Callaway-Holland model can be used to predict the thermal conductivity of Si and PnCs [25, 46, 47, 48]. Each expression inside the integral is a function of both the wave vector, $\boldsymbol{k}$, and dispersion branch, *s*. Adding these dependencies gives

$$\kappa = \left(\frac{1}{2\pi}\right)^3 \sum_s \int C(\boldsymbol{k}, s)(v(\boldsymbol{k}, s) \cdot \boldsymbol{l})^2 \tau(\boldsymbol{k}, s) d\boldsymbol{k} \quad \textbf{(3.8)}$$

In **Equation (3.8)**, $\boldsymbol{l}$ is a unit vector, and it is dotted with $\boldsymbol{v}$ to define the direction of interest for phonon transport. This is a more general expression for $\boldsymbol{v}$ compared to the velocity in **Equation (3.7)**, which is only for the *x*-direction. In **Equation (3.8)** κ is determined by integrating over the wave vector, $\boldsymbol{k}$. This integration involves the phonon volumetric specific heat $C(\boldsymbol{k}, s)$, the square of the phonon group velocity, $v(\boldsymbol{k}, s)$, and the phonon scattering relaxation time, $\tau(\boldsymbol{k}, s)$. All three can be determined from the phonon dispersion relationship. The summation occurs over each dispersion branch, *s*. The Callaway-Holland model accounts for phonon boundary scattering processes through τ, which includes a term that accounts for scattering due to the thickness of the PnC and for scattering due to the critical length. Details on how to use the Callaway-Holland along with descriptions of the various parameters can be found elsewhere [25, 46, 47, 48]. The main point of briefly describing the BTE and Callaway-Holland models is to state that both are dependent on the phonon dispersion relationship and can account for boundary scattering. If the phonon dispersion of a material can be altered in some fashion such as using a phononic crystal, then it is possible to alter a material's thermal conductivity. Accurately predicting the effect, however, from these equations is dependent on making the correct assumptions to arrive at a dispersion relationship.

3.2. Fourier's Law

Fourier's Law provides a description of heat transfer with respect to position.

$$\boldsymbol{q} = -\kappa \boldsymbol{\nabla T} \quad \textbf{(3.9)}$$

In **Equation (3.9)** the vector, $\boldsymbol{q}$, is the heat flux, κ is the material's thermal conductivity, and $\boldsymbol{\nabla T}$ is the temperature gradient, which is a function of position. As with the Callaway-Holland model, Fourier's Law can also be derived from the BTE. Fourier's Law also assumes the system it is describing is in steady state and ignores any transient response. Thus, there is no time dependence in Fourier's Law. In **Equation (3.9),** κ is considered a bulk property of the system. Although it states nothing about how κ is determined from factors such as scattering, porosity, or critical length, it is a useful method for measuring a material's thermal conductivity [17, 49, 50]. If a system can be treated as a 1D approximation where a planar heat wave can be assumed, a one-dimensional form of Fourier's Law can be used to measure the thermal conductivity of a material. In one-dimension, say the *x*-direction, Fourier's Law becomes

$$q = -\kappa \frac{dT}{dx} \qquad \textbf{(3.10)}$$

Although the PnCs used in this work are 2D PnCs, the 1D form of Fourier's Law still holds. The system was set up such that heat entering and leaving the PnC was accurately modeled as a planar wave. Therefore, a 1D form of Fourier's Law was used as the basis for determining the thermal conductivity of PnCs.

3.3. Finite Element Method

For this work COMSOL was used to estimate the thermal conductivity of the various PnC designs based on volume reduction. COMSOL uses a continuum approach to solve the heat equation and bulk values for material properties. It does not take scattering, such as boundary or coherent scattering, into account. It is useful for determining the effect of material removal on reducing Si's thermal conductivity. A

simplified model such as the one derived by Russell [42] to predict the thermal conductivity of a porous piece of Si can be used, but it deviates from COMSOL modeling by 10%.

The schematic of the basic COMSOL setup to determine thermal conductivity is shown in **Figure 3.1**. On the left and right side of the PnC are domain regions. Heat flux is applied the left side of Domain A (red line), and a constant temperature is boundary is applied to the right side of Domain B (blue line). Periodic or insulating boundary conditions are applied to the top and bottom of the simulation (black lines). The interfaces between the domains and PnC are where various measurements are performed. Both heat flux and temperature are measured at the interface between Domain A and the PnC. A second temperature measurement occurs at the interface between the PnC and Domain B.

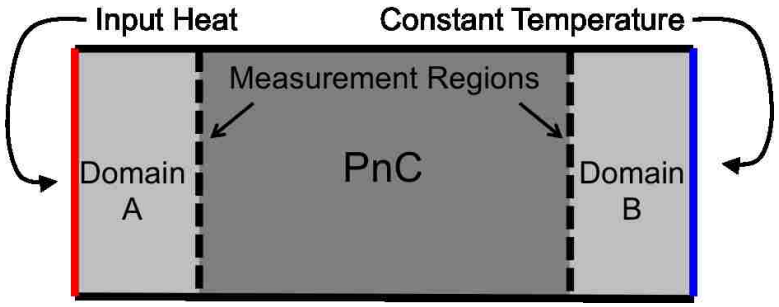

Figure 3.1: 2D diagram showing basic setup used in COMSOL for determining the effect of lattices on reducing silicon's thermal conductivity.

COMSOL is capable of solving the heat equation over the entire numerical space in a user defined 2D or 3D simulation. Due to the insulating boundaries the thermal energy flows from Domain A to Domain B. Applying a constant heat flux along the entire edge of Domain A sets up a planar wave of heat entering the system. Then by averaging over the nodes along the beginning and end of the PnC (dashed lines) the PnC's thermal transport can be approximated as a one-dimensional problem.

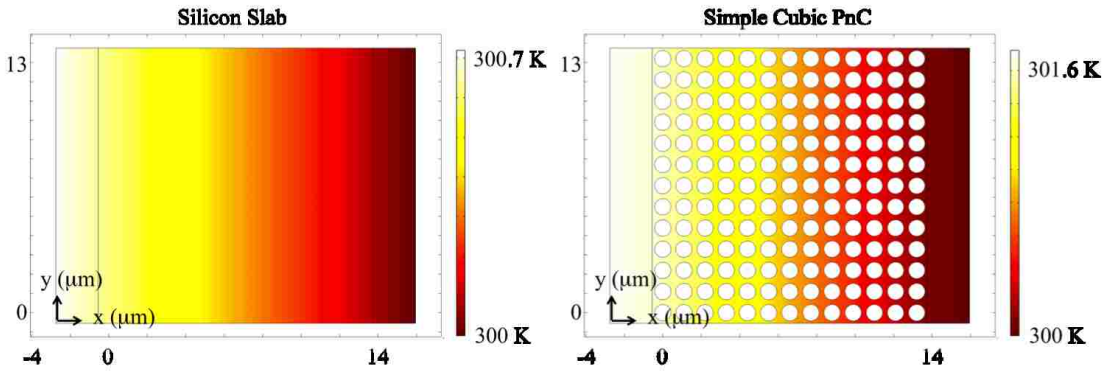

Figure 3.2: Surface temperature profiles for a Silicon Slab and a Square lattice PnC. Both profiles are planar, which validates the use of a 1D Fourier's Law approximation for determining thermal conductivity.

Figure 3.2 shows temperature profiles for a Si slab and the Square lattice PnC. Both simulations show a planar temperature profile. Verification of the 1D approximation is also shown by plotting temperature profiles along the *y*-axis on either side of the PnC. **Figure 3.3** plots the temperature profile immediately to the left (Hot Temperature) and right (Cold Temperature) of the Square lattice PnC. Both temperature profiles have a standard deviation of 0.002 K, which is 0.00067% of the mean temperature.

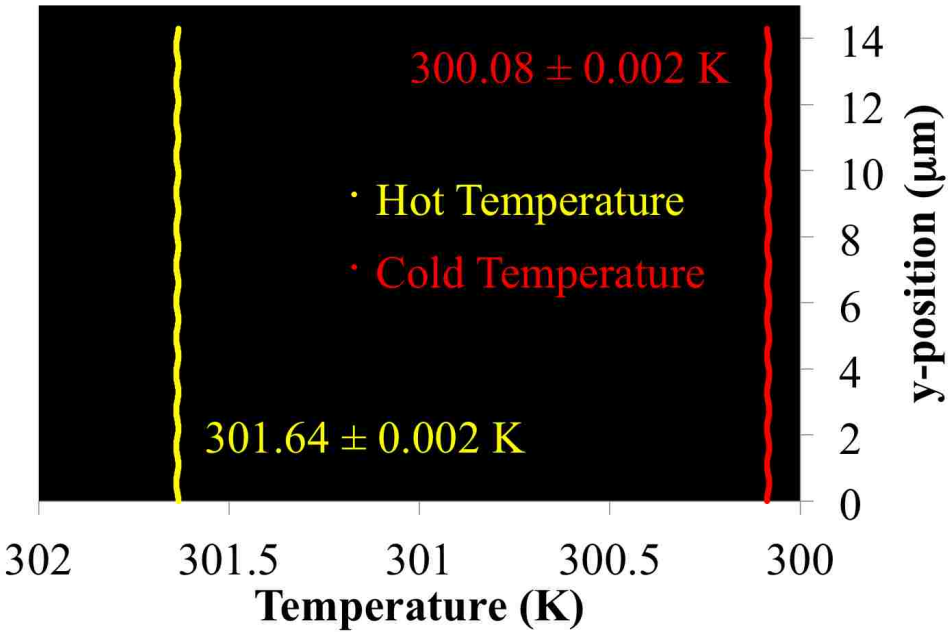

Figure 3.3: Graph of Square lattice PnC temperature values calculated by COMSOL that validates the 1D Fourier's Law approximation. Yellow is the *y*-axis immediately to the left of the PnC, and red is the *y*-axis immediately to the right of the PnC. Both have a standard deviation of 0.002 K.

Furthermore the temperature gradient can be approximated by a finite difference. Using these approximations Fourier's law becomes

$$q = -\kappa \frac{\Delta T}{\Delta x} \qquad (3.11)$$

where q is the heat flux in the x-direction, Δx is length of the PnC region, and ΔT is temperature difference across the PnC. The 1D approximation is investigated because of it applicability to the experimental apparatus described in Chapter 5.

Both two-dimensional (2D) and three-dimensional (3D) steady-state simulations were performed to estimate the effect of each crystal's porosity on silicon's thermal conductivity. The effects will be gauged by a relative thermal conductivity, κ_{rel}, which is the ratio of the PnC's thermal conductivity to the thermal conductivity of silicon. Initially a 2D analysis was performed. It was important to establish the proper mesh conditions and size of the PnC region such that neither affected the thermal conductivity. First, the

PnC region was a single square lattice unit cell with repeating boundary conditions on the upper and lower sides of all three regions (Domain A, Domain B, and PnC). Next the size of the mesh was refined to reach a mesh-independent value. After determining the proper mesh size, the length of the PnC region was extended to 10 unit cells and then to 20 unit cells to observe any effect of the length on the thermal conductivity. **Figure 3.4** shows the progression from 1 unit cell to 20.

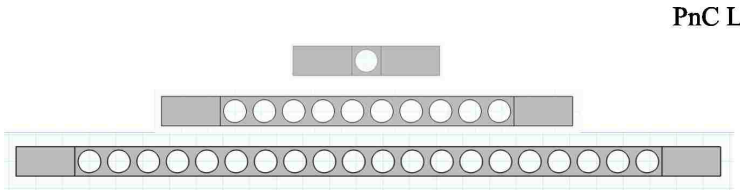

Figure 3.4: Progression of PnC lengths for validating thermal conductivity values independent of PnC length.

A small increase in the calculated thermal conductivity occurred from 1 to 10 unit cells, but there was no change between 10 and 20 unit cells. Next, the width of the PnC region increased from 1 to 13 unit cells with insulating boundaries to simulate the actual width of the fabricated PnCs. This introduced a minimal change to the thermal conductivity. Results for obtaining the proper mesh conditions are shown in **Table 3.1**. After determining the proper mesh conditions, the remaining lattices were simulated, and the results are shown in the bottom portion of **Table 3.1**. A graphical representation of the 2D results is shown in **Figure 3.5**. This figure also includes relative thermal conductivity values based on Russell's work [42], which is shown in **Equation (3.12)** where ϕ is the material's porosity.

$$\frac{\kappa_{porous}}{\kappa_{solid}} = \frac{1-\phi^{2/3}}{1-\phi^{\frac{2}{3}}+\phi} \qquad (3.12)$$

As stated previously, Russell's analytic model underestimates the effect of porosity on thermal conductivity by about 10%.

Table 3.1: 2D COMSOL results. Light gray boxes show effect of mesh resolution on κ_{rel}. Gray boxes show effect of PnC width and boundary conditions on κ_{rel}. Dark gray boxes show the results of the various lattices types.

Lattice	Mesh	Boundary Conditions	PnC length (μm)	PnC Width (μm)	d_1 (nm)	d_2 (nm)	κ_{rel}	Porosity
Square lattice	Finer	Periodic	1.1	1.1	850	-	0.348	0.469
Square lattice	Extra Fine	Periodic	1.1	1.1	850	-	0.348	0.469
Square lattice	Extremely Fine	Periodic	1.1	1.1	850	-	0.348	0.469
Square lattice	Extra Fine	Periodic	11	1.1	850	-	0.354	0.469
Square lattice	Extra Fine	Periodic	22	1.1	850	-	0.354	0.469
Square lattice	Finer	Insulation	14.3	14.3	850	-	0.354	0.469
1x1 Supercell	Finer	Insulation	14.3	14.3	850	206	0.335	0.497
2x2 Supercell	Finer	Insulation	14.3	14.3	850	206	0.344	0.483
3x3 Supercell	Finer	Insulation	14.3	14.3	850	206	0.348	0.478
4x4 Supercell	Finer	Insulation	14.3	14.3	850	206	0.350	0.476
Square lattice	Finer	Insulation	14.3	14.3	850	-	0.354	0.469

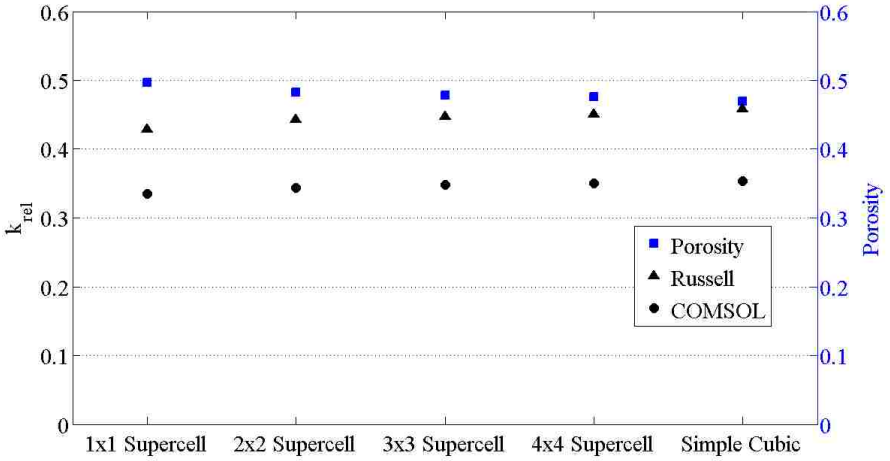

Figure 3.5: Plot of 2D COMSOL results. For porosity (blue squares), there is a maximum difference of 2.8% between all values. With respect to the relative thermal conductivity calculated by COMSOL (black circles), there is maximum difference of 1.9%. The analytical model by Russell (black triangles) underestimates the effect of porosity on the relative thermal conductivity calculated by COMSOL.

The PnCs are fabricated with a focused ion beam (FIB), which introduces non-vertical sidewalls. Based on this, it is important to incorporate the sidewall slope into the simulation to properly account for the amount of material removed and therefore better estimate how the of pattern's porosity affects Si's thermal conductivity. This requires a 3D study of the PnCs. In the 3D study, a frustum of a right circular cone was used to account for the sidewall slope induced by the FIB. Analysis of the vias fabricated with the FIB showed a 3° sidewall slope for both the large and small vias, (see Section 4.3). **Figure 3.6** is an image from COMSOL showing the difference between a cylindrical inclusion and a frustum of a cone.

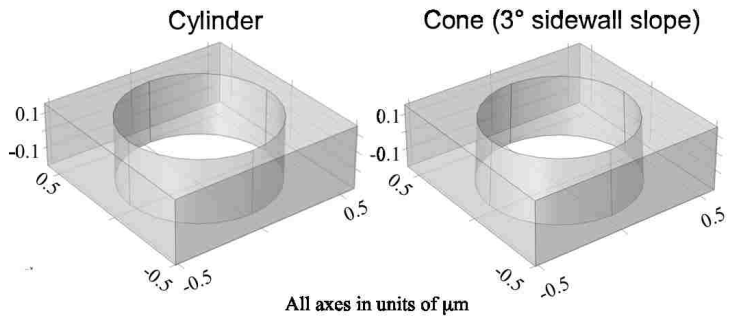

Figure 3.6: COMSOL snapshots showing the difference between a cylinder and a frustum of a cone with a 3° sidewall slope.

As with the 2D analysis, initial 3D simulations with cylinders established the proper mesh conditions. Next, the width of the PnC was increased from 1 to 12 unit cells, and this did not change the thermal conductivity. This work established the fact that the mesh, length, and width of the PnC region in 3D do not alter the thermal conductivity.

Next, the sidewall slope of the vias milled with the FIB was incorporated into the simulations. A graphical representation of the results is shown in **Figure 3.7**. The 3D results that incorporate the sidewall slopes and PnC widths are listed in **Table 3.2**.

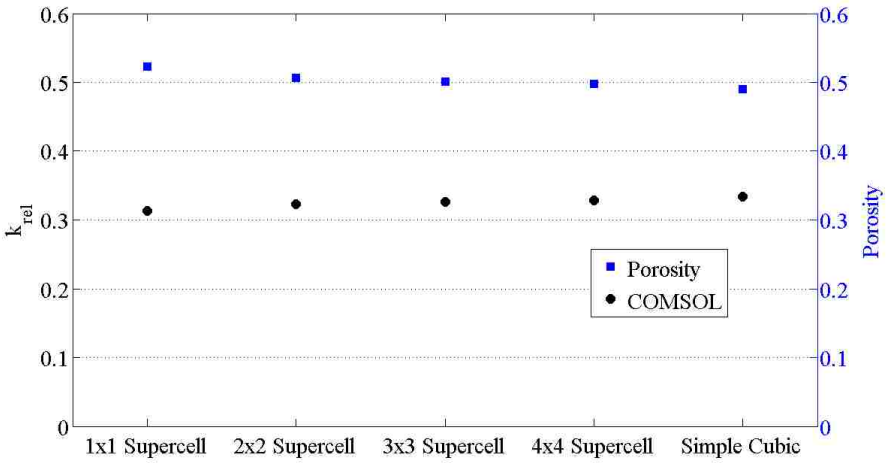

Figure 3.7: Plot of 3D COMSOL results. For porosity (blue squares) in 3D, there is a maximum difference of 3.3% between all values. With respect to the relative thermal conductivity (black circles), there is maximum difference of 2.1%.

Table 3.2: 3D COMSOL results. Light gray boxes show effect of mesh resolution on κ_{rel}. Gray boxes show the effect of PnC width and boundary conditions on κ_{rel}. Dark gray boxes show the results of the various lattices types which also incorporates thickness and a 3° sidewall slope for the vias/frustums. A tetrahedral mesh was used for each simulation.

Lattice	Mesh	Boundary Conditions	PnC Length (μm)	PnC Width (μm)	d_1 (nm)	d_2 (nm)	t (nm)	κ_{rel}	3D Porosity
Square lattice	Extra Fine	Periodic	11	1.1	850	-	500	0.354	0.469
Square lattice	Finer	Periodic	11	1.1	850	-	500	0.354	0.469
Square lattice	Finer	Insulation	14.3	14.3	850	-	500	0.355	0.469
1x1 Supercell	Finer	Insulation	14.3	14.3	850	202	362	0.313	0.523
2x2 Supercell	Finer	Insulation	14.3	14.3	850	206	362	0.323	0.507
3x3 Supercell	Finer	Insulation	14.3	14.3	850	206	362	0.326	0.501
4x4 Supercell	Finer	Insulation	14.3	14.3	850	206	362	0.328	0.499
Square lattice	Finer	Insulation	14.3	14.3	850	-	362	0.334	0.490

4. Fabrication of phononic crystals using FIB

This chapter is dedicated to describing how phononic crystals were fabricated with a tool called a focused ion beam, or FIB. All of the FIB milling and nanoFIBrication (using a FIB to fabricate on the nano-scale) in this work was performed on a dual-beam Quanta 3D FEG manufactured by FEI. The dual-beam refers to the system having both a FIB and scanning electron microscope (SEM).

4.1. Focused Ion Beam Basics

A focused ion beam (FIB) is a system that generates a focused stream of charged particles (ions). Ions are extracted from a material, accelerated, and then focused into a narrow beam with a Gaussian density distribution by using various apertures and electro-magnetic fields (octopoles). **Figure 4.1** shows a schematic of the basic components in a FIB.

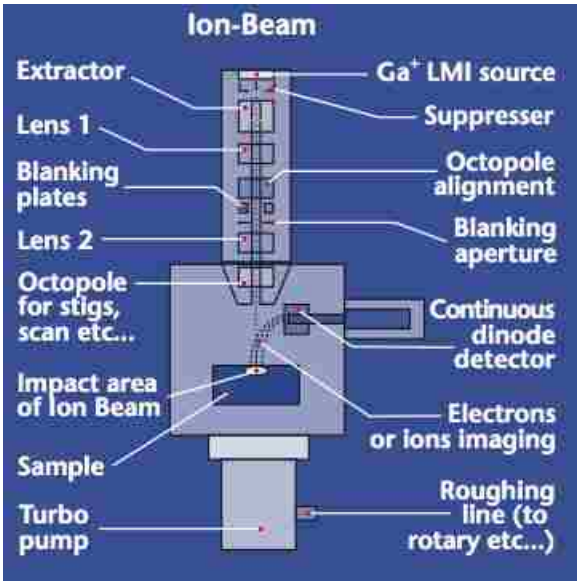

Figure 4.1: Schematic of a focused ion beam (FIB). Ions are extracted and then focused by multiple apertures and electromagnetic fields onto a sample. All of the FIB components and sample are under vacuum to prevent degradation (Image courtesy of FEI).

A common source for generating ions is called a liquid metal ion source (LMIS). **Figure 4.2** shows a drawing of a LMIS [51]. Liquid metal from a reservoir is allowed to flow on to the tip of a sharp needle. The most common metal used is monoisotopic gallium due to its low melting point, low vapor pressure, low reactivity with other elements, produces mainly singly charged ions, and it has enough mass to dislodge material at an acceptable rate [52]. As the liquid metal rests at the tip of the needle, an extractor lens with a large accelerating voltage pulls positively charged ions from the liquid. Typical accelerating voltages are between 5 and 30 kV.

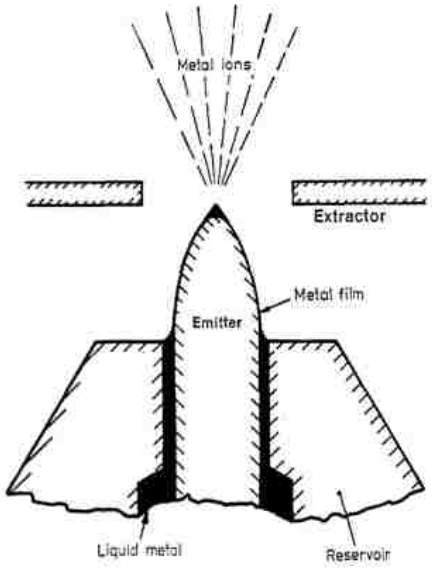

Figure 4.2: Drawing of a liquid metal ion source (LMIS). [51] Liquid metal wets a sharp tip and an extractor lens extracts ions from the metal by using a high accelerating voltage in the kV range.

Once the focused beam of ions leave the ion column, they interact with the sample surface. When a single Ga^+ ion strikes the sample surface, it can have enough energy and momentum to cause other atoms at the sample surface be removed, or sputtered away. The mean number of atoms removed for a single ion striking the sample surface is known as the material's sputter yield. A material's sputter yield is a dependent on the type of ion bombarding the surface, the ion's accelerating voltage, and the angle of

incidence. Increasing the accelerating voltage increases the sputter yield. As the angle of incidence changes from 0° to approximately 80° (with respect to normal), the sputter yield increases then quickly drops from 80° to 90°. A plot of sputter yield vs. angle for various materials is shown in **Figure 4.3**. The ion species is Ga^+ at 30 kV. Sputter yields were calculated using a Monte Carlo simulation package named TRIM (Transport of Ions in Matter). TRIM calculates the stopping and range of ions into matter using a quantum mechanical treatment of ion-atom collisions [53]. The solid lines in **Figure 4.3** are interpolated values.

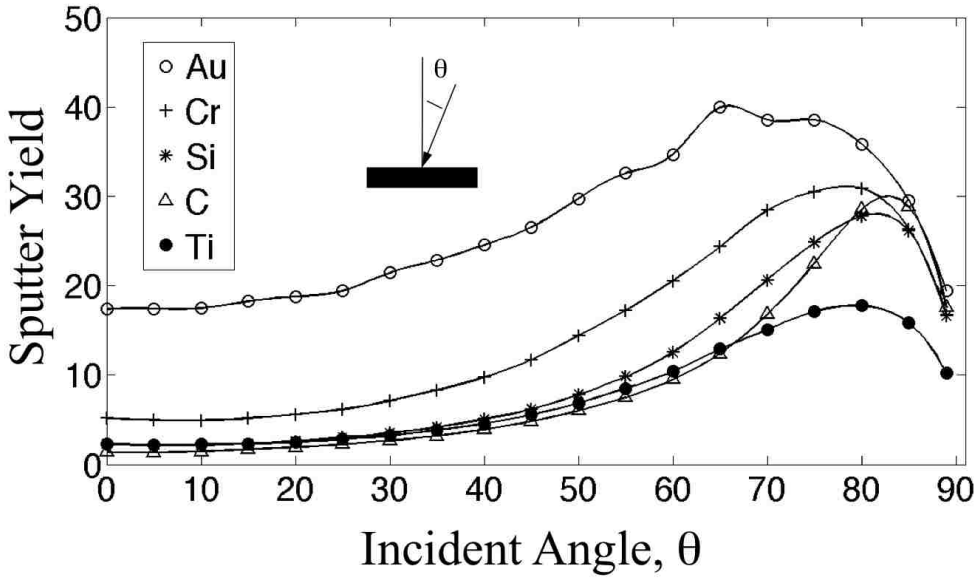

Figure 4.3: Sputter yields for various materials as a function of angle. Incident ion is Ga^+ at 30 kV. Sputter yields were calculated using a Monte Carlo simulation package named TRIM. Solid black lines are interpolated values.

4.2. Aspect Ratio

Milling vias in a sample cannot go on indefinitely. There are limits to how deep a via can be milled. As the depth of the via increases, it becomes more difficult for milled material at the bottom of the via to overcome the incoming ion flux and the sputter yield decreases [54]. Eventually the milled material can no longer escape and a maximum depth is reached. For unassisted milling, where no gas-assisted-etching occurs, the maximum

ratio between the via depth and its diameter is 5:1 [45]. This ratio is called the aspect ratio. At high aspect ratios, however, the via becomes Gaussian shaped and resembles the ion beam profile. An example of a 5:1 aspect ratio via milled in Si with the FIB is shown in **Figure 4.4**. The via diameter varies with depth, and a cylinder rather than a cone is the ideal shape of the vias for the 2D PnCs used in this work.

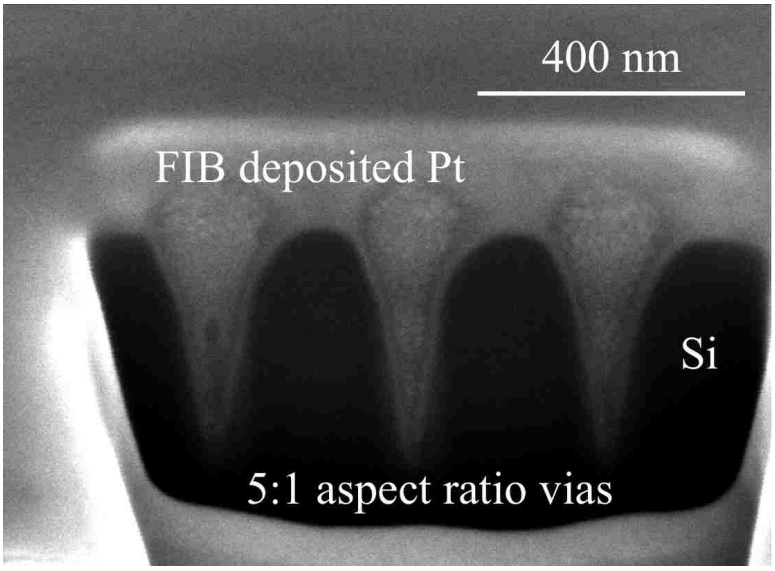

Figure 4.4: SEM image showing cross-section of 5:1 aspect ratio vias milled in Si with a FIB. A protective layer of Pt was deposited on the vias prior to cross sectioning.

Achieving vias with vertical, or near vertical, sidewalls can be accomplished in various ways. One method makes use of gas-assisted etching, but this requires additional equipment and gases such as chlorine [55, 56]. Another method is to simply reduce the aspect ratio of the via being milled. Aspect ratios in this work are less than 1.8:1. Last, use of a hard protective layer (low sputter yield material) on top of a soft (high sputter yield material) substrate can also help achieve near-vertical sidewalls. More discussion on this technique is in the next section.

4.3. Micro-fabrication and Si Preparation

Prior to milling PnCs with the FIB, it was necessary to micro-fabricate Si matrices. Two different paths were used. In the first path Si matrices were freely suspended prior to using the FIB to fabricate nano-scale devices, which is called nanoFIBrication for short. The other path allowed suspension of the PnC after milling with the FIB. Both paths use a top-down approach; start with bulk material and remove the unnecessary material.

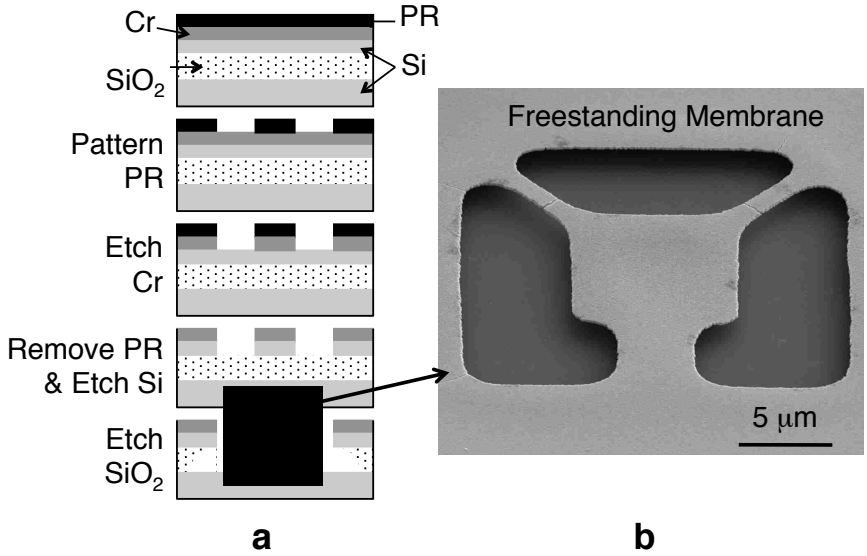

Figure 4.5: Fabrication process for creating a thin-freestanding membrane for PnCs. a) Cross sectional view of fabrication process. b) Released freestanding membrane.

For the first path, the first step in fabricating PnCs was creating a thin device layer on a silicon-on-insulator (SOI) wafer. Studies show that thin membranes produce a band gap that is unaltered by slab modes [57]. More specifically, the membrane must be thinner than the lattice spacing. For example, a 33 GHz PnC (33 GHz refers to where the bandgap is centered) requires a device layer less than or equal to 100 nm. In order to thin the initial 450 nm thick device layer of the SOI wafer down to a thickness of 100 nm or less, thermal oxide layers were grown from the Si and subsequently etched away until the

desired thickness was attained. Initial variation of the device layer (±25 nm) caused similar variation in the final membrane thickness. After thinning, outlines of the PnC were patterned on the wafer. The process for creating the PnC outlines is show in **Figure 4.5a**.

A drawback to nanoFIBricating vias in a thin free-standing membrane is the profile of the vias. For a 100 nm thin Si membrane, damage to the Si layer generated a conical shape, or trumpet-like appearance [58]. A cross-section of the vias is shown in **Figure 4.6b**. As the Ga^+ ions exit a thin membrane, they spread out and cause damage in a conical shape as shown by simulations in **Figure 4.6a**.

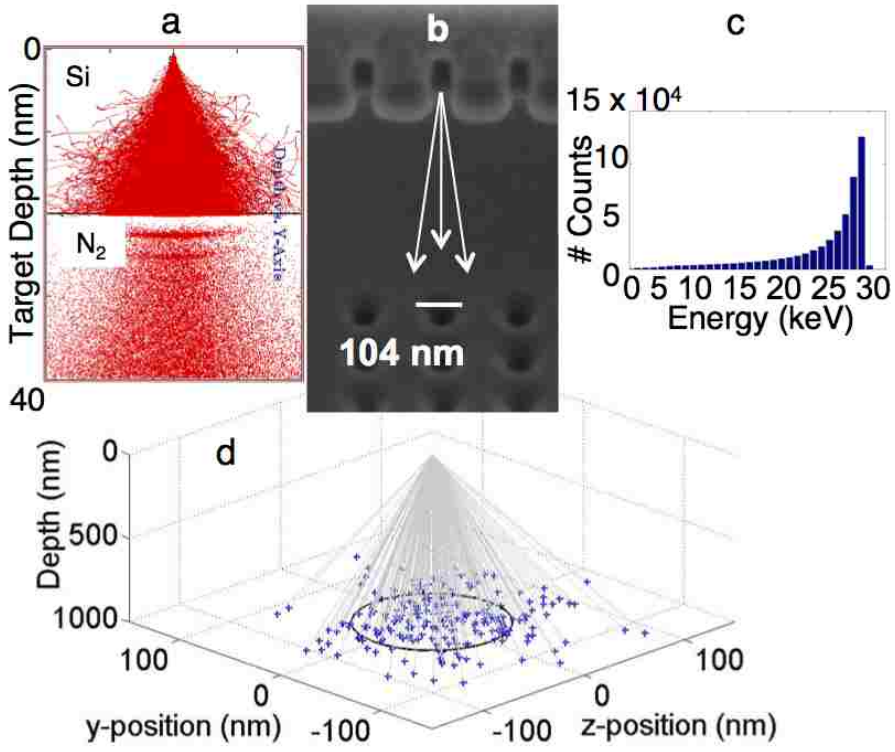

Figure 4.6: Explanation of observed trumpet-like appearance when milling freestanding thin films. a) Image from TRIM showing Ga^+ ion induced damage to 20 nm thick layer of Si with N_2 gas on underside of Si. b) SEM image of vias generated in both the Si membrane and substrate. c) Distribution of Ga^+ ion energies as they exit the freestanding Si membrane. d) Results from post-processing of TRIM data. Gray lines show trajectory of Ga^+ ions ejected from the bottom of the freestanding Si surface. Blue crosses at the bottom of the y-z plane represent locations of Ga^+ ions in Si substrate. The black circle has a radius of 56.3 nm and is equal to the mean distance of the Ga^+ ions in the substrate from the *x*-axis (Depth).

The second method for fabricating Si matrices is similar to the first method, but the release step is performed after milling with the FIB. The process flow is shown in **Figure 4.7**. With this method, there is no trumpet-like appearance. Removal of the protective layer is also simpler since the possibility of stiction failure [59, 60, 61, 62] cannot occur during this step.

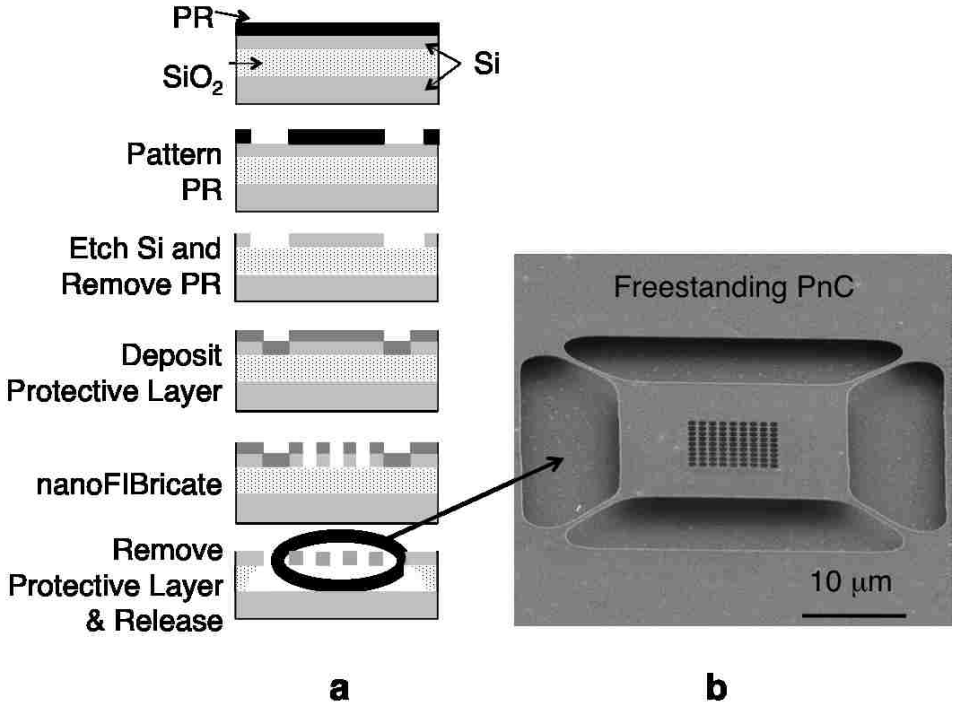

Figure 4.7: Second fabrication method for creating a thin-freestanding PnC. a) Cross sectional view of the fabrication process. b) SEM image of a released freestanding PnC.

In both methods mentioned above, a protective layer is placed on top of the Si. The protective layer minimizes Ga doping in Si, which can affect both electrical [63, 33] and thermal properties [30] of Si. Since the goal of this effort is to determine how a PnC affects the thermal conductivity of Si, it is important to minimize any additional variables that are known to affect the thermal properties of Si.

Choosing the proper protective layer is dependent on a number of factors. It must be relatively easy to add and remove. The protective layer needs to be compatible with

the fabrication process. It must also be relatively thin. If it is too thick, then the ion beam will have a difficult time penetrating both the protective layer and Si. Another consideration is electrical conductivity. If it is not conductive, then the incoming charged ions would be affected. As charge builds up on the sample surface, the ion beam will become distorted and will no longer mill the desired area. Last, it should have a sputter rate that is less than Si.

The best types of materials to be used as a protective layer are metals. Metals make a good protective layer for multiple reasons. They are easy to deposit, they are easy to find an etchant with a high selectivity between a given metal and Si, they are highly conductive which improves imaging in the SEM, and only a thin layer is required to block Ga^+ ions from penetrating into Si. For example TRIM calculations of Ti show that 30 kV Ga^+ ions have a mean penetration depth of 18 nm into a 100 nm thick layer of Ti. A graph of the results is shown in **Figure 4.8**. Ni has a smaller penetration depth of 9.7 nm, but Ni reacts with the fluorine in a hydrofluoric acid vapor and leaves a thin, greenish layer of NiF_2 on the PnC. Ti, on the other hand, has the advantage of being etched by hydrofluoric acid. Since hydrofluoric acid is required for removing the buried oxide (BOX) layer and thus releasing the PnC, Ti makes a good choice for a protective layer. To ensure no Ga reaches the Si, a 50 nm thick layer of Ti is used as the protective layer for fabricating PnCs with the FIB.

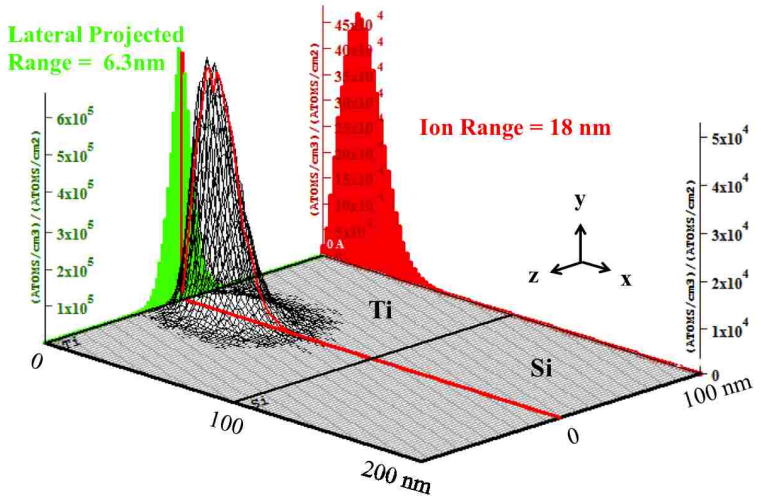

Figure 4.8: TRIM calculations of 30kV Ga^+ ion penetration into 100 nm thick layer of Ti on top of 100 nm layer of Si. No ions reach the Si layer. The mean ion penetration depth in the x-direction (red) is 18 nm. The lateral projected range (green) is 6.3 nm.

As mentioned previously, the protective layer should have a sputter rate that is less than Si. This is because the relative sputter rate of the protective layer with respect to Si can affect the profile of the via in Si. If a "soft" material is used, the Gaussian-shaped ion beam will quickly remove the softer material on top of the "harder" Si. As more and more of the "softer" material is sputtered away, a larger percentage of the wings of the Gaussian-shaped ion beam will also sputter the Si. The resulting profile is non-ideal and potentially exposes more of the Si surface around the via. Unlike the "soft-on-hard" material set, a "hard-on-soft" material set will protect the Si from the outer edges of the Gaussian-shaped ion beam and allow more of the central portion of the ion beam to mill the softer layer away. This results in the sidewalls of the via in the "softer" material being more vertical. A side-by-side comparison of simulation results for both possibilities is shown in **Figure 4.9**.

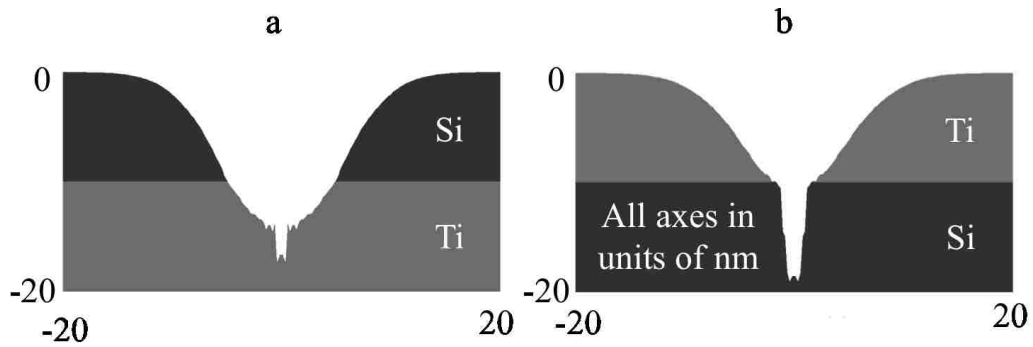

Figure 4.9: Simulations showing cross-sections of via profiles using Ti and Si. a) Simulation of soft-on-hard (Si on Ti). b) Simulation of hard-on-soft (Ti on Si).

In these simulations Ti was the "hard" material and Si was the "soft" material. Simulations were performed in MATLAB® and took into account the sputter yield's angular dependence. Direct observation of sidewall profiles generated by the "hard-on-soft" material set of Ti and Si is shown in **Figure 4.10**. Sidewall slopes of 3° were observed.

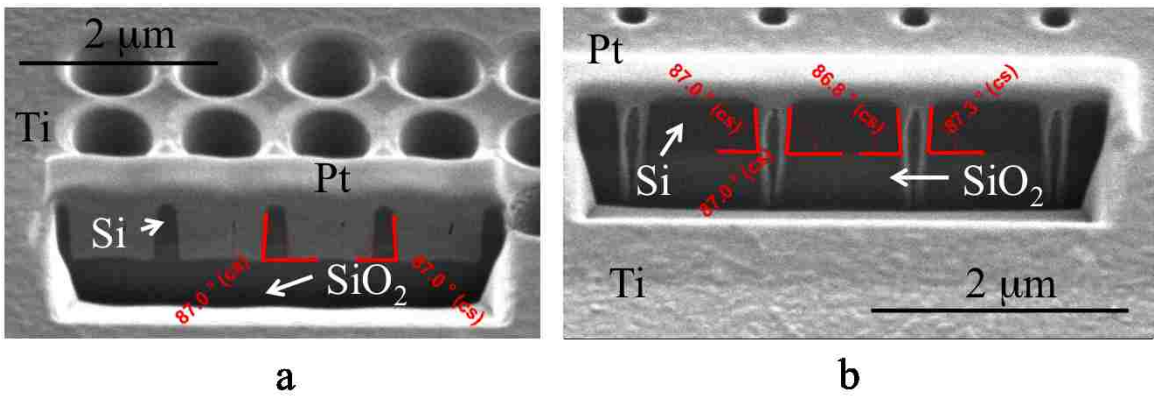

Figure 4.10: SEM images showing cross-sections of a "hard-on-soft" material set (Ti on Si). a) Large vias with a diameter of 850 nm. b) Small vias milled with a diameter of 210 nm. Both the large and small vias showed a sidewall slope of 3°.

A third approach to PnC fabrication with the FIB uses a stencil to protect the Si. The steps required for this approach are shown in **Figure 4.11**. This process starts off with released Si membranes. Second, the PnC crystal pattern is milled in to a released membrane. This will be the stencil for the actual PnC. Next, the stencil is cut out and then placed on top of another Si membrane. With the stencil in place to protect the Si

from inadvertent Ga doping, the pattern is milled a second time. The last step is to remove the stencil (**Figure 4.11b**). This approach is time consuming, and the sidewalls of the inclusions have a slope of 4°. A comparison between the sidewall profile of the Si stencil and the Si PnC is shown in **Figure 4.12**. The sidewall slope of the stencil is approximate 8°. By using the stencil technique, the sidewall slope improved by 4°.

Two potential drawbacks to this approach relate to re-deposition. The first is the potential to generate a ring of material around the milled via, and this is shown in **Figure 4.12b**. As Si atoms are being sputtered from the via, they can become trapped between the stencil and Si membrane and re-deposit on to the region around the via. Second, a re-deposited layer of material can form that physically connects the stencil to the Si membrane. This effectively *welds* the two layers together, which makes it impossible to remove the stencil. Due to the conical shape of the vias generated with the first method and the amount of time required for the third method, the second method of milling the vias prior to release was used to fabricate the supercells.

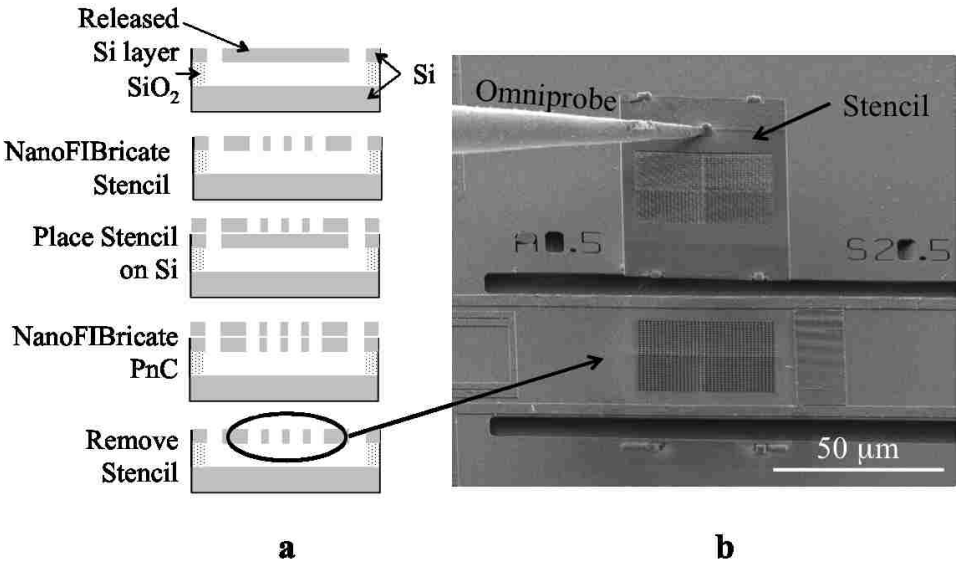

Figure 4.11: Third fabrication method for creating a thin-freestanding PnC using a nanostencil. a) Cross sectional view of fabrication process. b) Stencil being removed with Omniprobe to show PnC milled into free-standing Si membrane. SEM image taken at a tilt of 52°.

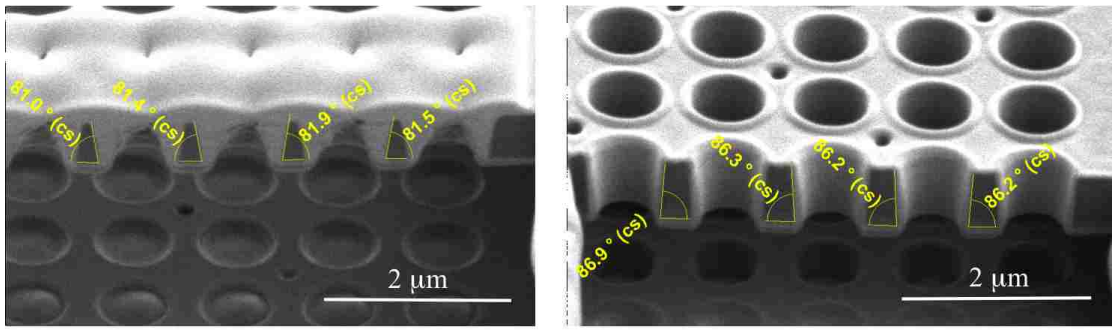

a **b**

Figure 4.12: SEM images taken at a tilt of 52° showing cross sections of square lattice pattern. a) Cross-section of vias milled into stencil. b) Cross-section of PnC vias milled using stencil technique. Dark grey vias at the bottom of the image are vias milled into the substrate.

Prior to depositing the protective layer of Ti on to the Si, the Si underwent a wafer thinning process. Si for the PnCs came from the same SOI wafers used in Reference 17. The 500 nm thick n-type device layer was doped with phosphorus, had a resistivity of 50 ± 12.5 Ω-cm, and it had a <100> orientation. Its BOX layer was 3 µm thick. Deposited on top of the device layer was 100 nm of amorphous Si (a-Si). In order to remove any potential effects of the a-Si, all samples underwent a thermal oxidation process to remove the a-Si. Removal was performed in two steps. Electron backscatter diffraction (EBSD) analysis of the Si surface showed whether or not all of the a-Si was removed (**Figure 4.13**). A single color represents a single crystal orientation whereas a multi-colored surface is comprised of many crystal orientations. After 150 min. of thermal oxidation, EBSD results showed that the a-Si had not been removed. An additional 60 min. fully removed the a-Si layer. After verifying the a-Si layer was fully removed, a 50 nm Ti protective layer was sputtered on to the Si surface for milling the two-dimensional patterns with the FIB.

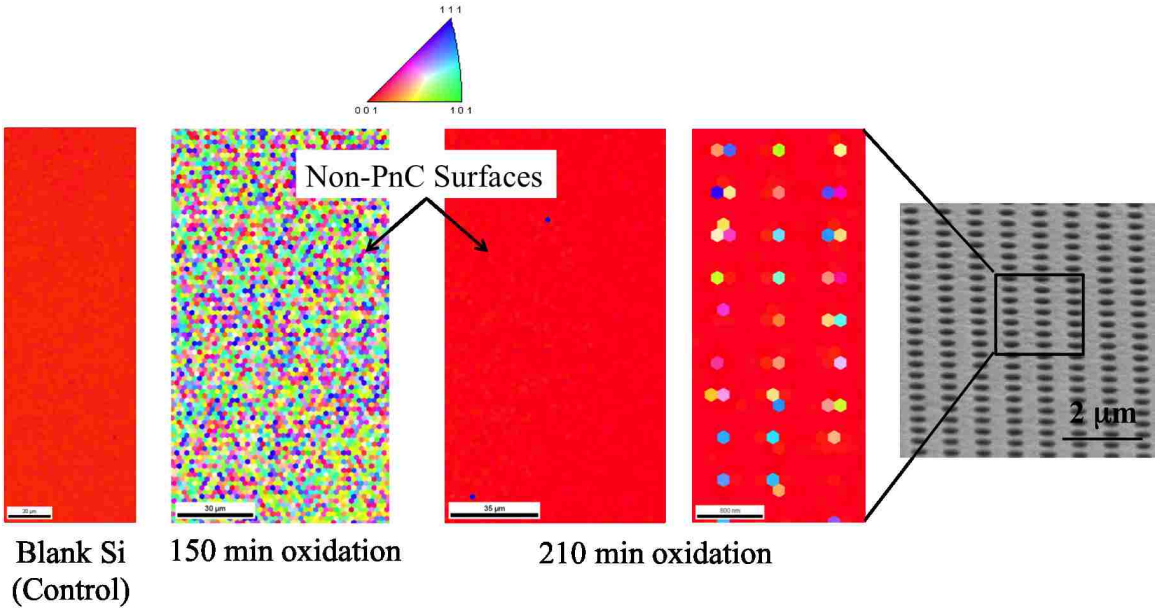

Figure 4.13: Results from EBSD: A solid red color indicates a single crystal orientation. A control sample of a blank Si wafer is shown on the far left side. After 150 min. of thermal oxidation, amorphous Si was still present. An additional 60 min. removed the a-Si layer. EBSD analysis was performed on both a non-PnC surface and PnC surface.

4.4. Generating PnC Software Masks

No matter which technique is used to nanoFIBricate a PnC, use of the FIB in all three instances requires generation of a software mask. A software mask controls the position of the FIB, and there are three methods for generating the mask. The three methods are the patterning toolbox, bitmap, and stream file. Each method has certain advantages and disadvantages. All three methods, however, use the same principles for adding or removing material.

In order for the system to remove material, one must specify the ion beam's location and the amount of time at each location. When specifying the beam's location, it is important to note the diameter of the beam. Suppose one wants to mill a line with a width d and length L (middle of **Figure 4.14**). Assume the width of the ion beam that will be used to mill the line is also d. If there is no overlap of the beam's diameter, then the 'line' that is milled will simply be a row of discrete points (top of **Figure 4.14**). If,

however, the beam location for successive milling points is equal to 50 % of the beam's diameter, then a continuous line will be milled (bottom of **Figure 4.14**).

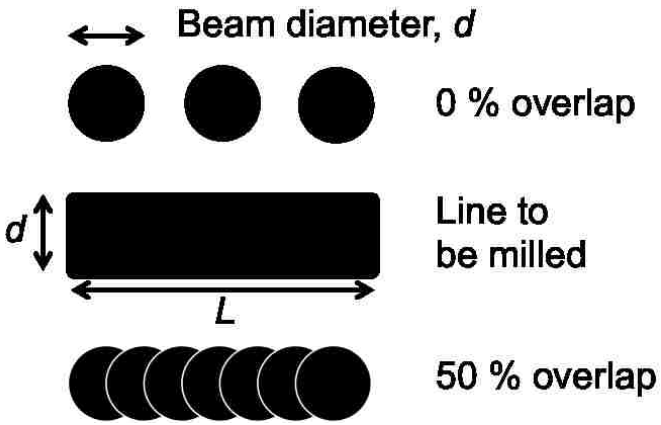

Figure 4.14: Schematic showing the relationship between beam diameter and overlap. 0% overlap of the beam diameter results in a discontinuous line while 50% overlap results in a continuous line.

This same argument for beam overlap applies to any shape to be milled such as a circle, square, rectangle, etc. Pattern depth is determined by the amount of time the beam is at each milling point and limited by the maximum aspect ratio possible. The milling time is determined by dwell time and number of passes. Dwell time refers to the amount of time the ion beam will stay at a single milling point before proceeding to the next milling point. The number of passes refers to how many times a particular pattern will be milled.

4.4.1. Patterning toolbox

The patterning toolbox is the easiest method for creating a small number of patterns. In the toolbox are a number of commonly used shapes and patterns. Using the mouse one can quickly point and click on the screen to create a pattern of the desired size at the desired location. Fine-tuning of the shape and its depth is as simple as typing in the desired parameters. Another useful feature is automatic re-sizing. If a pattern is drawn at a magnification of 500x and the user increases the magnification to 1000x, the size of the pattern scales with the magnification automatically. One major disadvantage of the

patterning toolbox is the inability to create elaborate patterns with varying depth or fine detail.

4.4.2. Bitmap

Bitmap patterning uses a 24-bit RGB bitmap image to create more elaborate patterns.[64] Each pixel consists of a red, green, and blue component. Currently, the red component is not used. The green component determines if the beam is blanked. Any value other than zero activates the beam. The blue component determines the dwell time per pixel. A value of zero sets the dwell time to 100 ns while a blue value of 255 sets the dwell time to the maximum dwell time specified by the user. Although bitmap patterning allows for more elaborate patterns to be milled, creating an elaborate bitmap with the desired parameters can be difficult. One must specify all of the RGB values for each pixel in the image.

4.4.3. Stream File

Patterning with a stream file provides complete control of the beam. When using the toolbox or a bitmap, scanning a pattern is limited to a raster or serpentine path (the exception is a circle using the patterning toolbox which does allow a circular scan). With a stream file the scanning pattern is controlled by the stream file itself and can be arbitrary. The different scan types are shown in **Figure 4.15**.

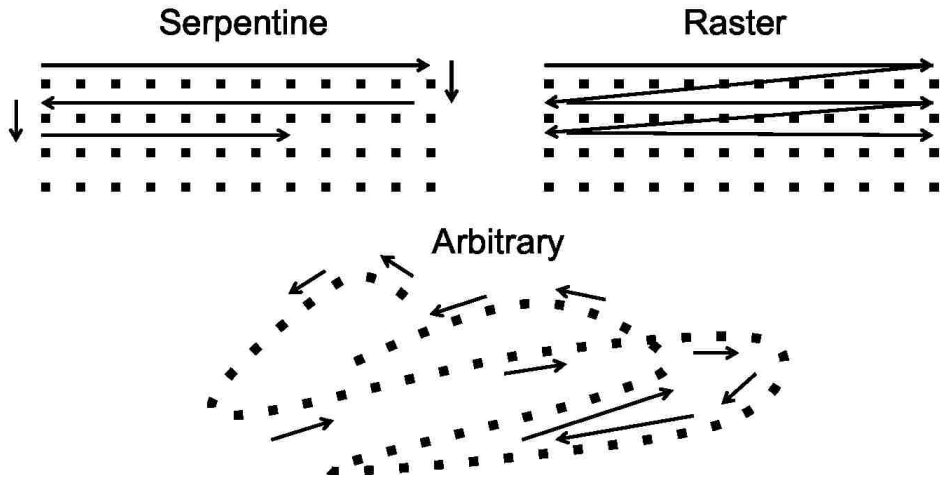

Figure 4.15: Scan patterns. Patterning with the toolbox or with a bitmap is limited to a serpentine or raster scan while a stream file has the capability to make an arbitrary pattern.

A stream file is an ASCII text file that addresses pixel location directly.[64] The patterning field of view is divided into 4096 steps. The range in *X* is 0-4095, and *Y* is from 280-3816. *Y* values outside this range will be off the image area and may not scan correctly. **Table 4.1** shows the contents of a typical stream file. The first line in a stream file must be the letter '*s*'. The second line defines the number of loops, and third line indicates the total number of *X*-*Y* coordinate pairs. All remaining rows are comprised of three space-delimited columns. The first column represents dwell time (units of 0.1 μs) and the second and third columns are the *X* and *Y* coordinates, respectively. In **Table 4.1**, the stream file is comprised of 10 points, and it will be repeated 32 times. The first point is at (2048, 2048), and the ion beam will dwell for 8.5 μs before proceeding to the next point at (2060, 2043). Stream files can be generated using programs such Microscoft® Excel, MATLAB®, or any suitable text processor.

Table 4.1: Steam file contents.

s		
32		
10		
85	2048	2048
85	2060	2043
85	2064	2039
85	2066	2034
85	2067	2030
85	2068	2026
85	2068	2022
85	2067	2019
85	2066	2015
85	2065	2012

There are many intricacies in using a stream file. Since pixels are addressed directly, the physical dimensions of the stream file change with magnification or Horizontal Field Width (*HFW*). For example, if *HFW* = 100 μm, then the horizontal spacing, *a*, between the first two *x* coordinates listed in **Table 4.1** is 293 nm. However, if the *HFW* is changed to 150 μm then the spacing becomes 439 nm. Vertical spacing, or spacing in the *y*-direction, is the same as the *x*-direction. **Equation (4.1)** describes the relationship among *a*, *HFW*, and ΔX_{pixels}, which is the number of horizontal pixels between two successive milling points.

$$a = \frac{HFW}{4096\ pixels} * \Delta X_{pixels} \qquad (4.1)$$

4.4.4. Stitching Patterns Together

Theoretically it is possible to generate a single software mask to fabricate each unique PnC, but in reality it is not possible. Overall, the goal is to achieve less than 10 nm of accuracy for the critical length, and milling accuracy is related to HFW. Performing the milling with a single software mask would require a 70 μm HFW, which

corresponds to 17 nm per pixel. The pixel error at this width is greater than the desired accuracy. Also, there would only be 30% overlap between two adjacent pixels since the diameter of the FIB is 24 nm at 100 pA beam current. Drift is another issue, and any drift would destroy the entire pattern. In terms of milling time, a single pattern takes roughly 10 hrs. of milling. It is highly unlikely there would be no drift over this period of time.

Another possibility is to mill a single unit cell and stitch each one together. Stitching patterns together requires alignment of the new pattern to the old pattern(s). Depending on the supercell, milling a single unit cell would require a HFW between 1.4 and 7 μm, which corresponds to 0.3 and 1.7 nm/pixel. For the largest unit cell, which is the 4x4 supercell, this would require a minimum of 90 patterns stitched together. Although this is possible, this increases the chance of user error due to the number of stitches and aligning four patterns together in two dimensions.

In the end a compromise is reached between a large software mask and stitching error. The path forward is to generate a software mask equal to the width of the PnC (not the unit cell). This only requires stitching 10 patterns together, and the HFW is 18.6 mm with 4.54 nm/pixel spacing. Alignment also becomes easier since it only occurs along a line rather than in two-dimensions.

4.5. Phononic Crystal Characterization

All of the phononic crystal dimensions were based on SEM images and image processing with MATLAB®. PnC lengths, L, and widths, w, were determined from top-view images. Thickness measurements, t, were performed at a tilt of 85° and did not use MATLAB® image processing. Standard deviation values, σ, were also determined for each measurement. A listing of all the lengths, widths, thicknesses, and corresponding

standard deviations are shown in **Table 4.2**. Associated with each PnC was a Si slab, which was not milled by the FIB, and it acted as a reference measurement for each PnC. Determining the length of the silicon slab did not incorporate image processing with MATLAB®. Rather than σ values an error value is reported for each Si slab length, which is based on ± 2 pixels for each length measurement. The width of the Si slab, however, was determined by image processing. A more detailed description of the samples is given in Section 5.

Table 4.2: Listing of all the lengths, widths, thicknesses, and corresponding σ values for the supercells and Si slabs. Note: Recorded with each Si slab length is an error value based on ± 2 pixels.

Lattice Type	PnC *L* (μm)	PnC *w* (μm)	PnC *t* (μm)	Si Slab *L* (μm)	Si Slab *w* (μm)
Square lattice	134.1 ± 0.7	14.75 ± 0.16	0.363 ± 0.019	357.5 ± 1.3	2.71 ± 0.05
1x1 Supercell	133.4 ± 0.01	14.59 ± 0.02	0.362 ± 0.016	360.2 ± 1.3	3.05 ± 0.04
2x2 Supercell	137.1 ± 0.7	14.47 ± 0.11	0.37 ± 0.016	359.5 ± 1.3	2.98 ± 0.04
3x3 Supercell	133.3 ± 0.03	14.58 ± 0.17	0.366 ± 0.016	358.7 ± 1.4	3.09 ± 0.04
4x4 Supercell	133.4 ± 0.5	14.32 ± 0.07	0.368 ± 0.01	360.1 ± 1.4	3.02 ± 0.02
Average	**134.7 ± 1.3**	**14.5 ± 0.2**	**0.366 ± 0.003**	**359.2 ± 1.5**	**3.04 ± 0.17**

Width measurements for the PnCs and the silicon slabs used image processing. First, a region of interest, or *ROI*, was selected, and then its area was determined by counting the total number of pixels in the *ROI*. After determining each area, the width was calculated by dividing the area by the length of the *ROI*. Multiple measurements were performed on each sample to achieve a more accurate width measurement. **Figure 4.16** shows the main steps for how the image processing was carried out in MATLAB®.

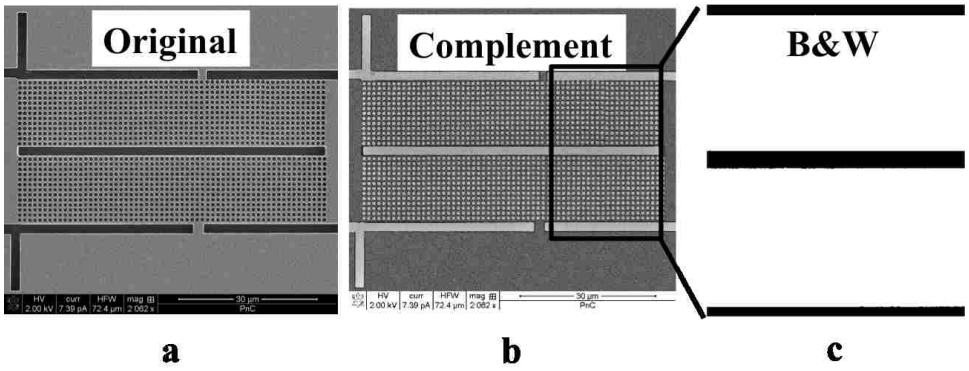

Figure 4.16: Main image processing steps used to determine width of PnCs and Si slabs. a) Original SEM image b) Complement of original image. A *ROI*, which is indicated by a black box, is selected from this image. c) Black and white image of two *ROIs*. Widths of each *ROI* are calculated by dividing the area of each white portion by its respective length.

Length measurements for the PnC also used image processing with MATLAB®. The main steps for determining PnC length are shown in **Figure 4.17**. After generating a complementary image of the original, a portion of the image is selected and converted to black and white. Vias on the far left and far right side of the PnC are selected, and the distances between corresponding centroids on the left and right are calculated. This is done for both portions of the total PnC. The final length incorporates the diameter of the vias.

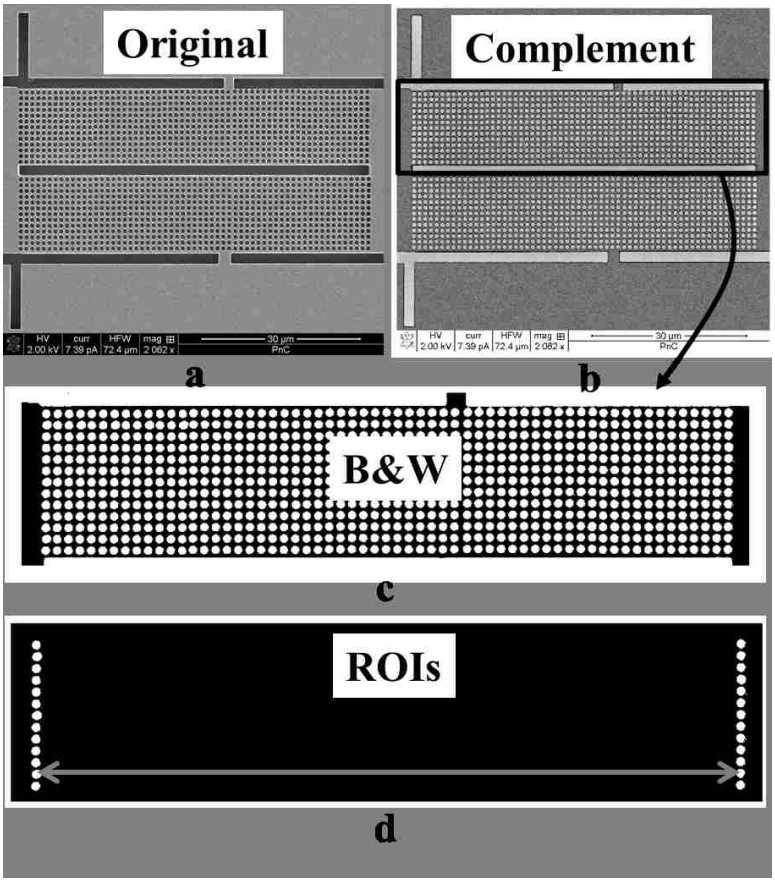

Figure 4.17: Main image processing steps used to determine length of PnCs. a) Original SEM image of the PnC. b) Complement of original image. A portion of the image is selected, which is indicated by a black box. c) The selected portion is converted to a black and white image, and vias on the far left and far right are selected as *ROI*s. d) Distances between the centroids on the left and right are then calculated to determine the length of the PnC.

In order to confidently compare the thermal conductivity values of the PnCs, it was extremely important to have minimal variation in the pitch, via diameters, and critical lengths over a single PnC along with minimal variation among all of the PnCs. A MATLAB® script was written to determine the diameter of multiple vias from SEM images along with the distances between nearest neighbor vias. First, the areas of the vias were estimated by counting the number of pixels for each via, and then the diameters were determined by the estimated via areas. Both the average diameter and standard deviation were calculated for the large and small vias. **Figure 4.18** shows the main steps for how the MATLAB® code works. A gray-scale SEM image of the phononic crystal is

loaded, its complementary image is generated, a portion of the image is converted into a black-and-white image, and finally regions of interest (ROIs) are used to determine the diameters of the vias.

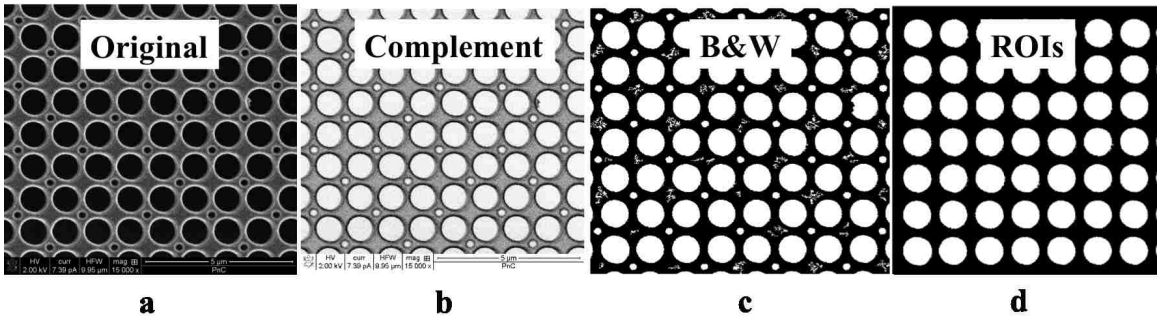

Figure 4.18: Image processing steps taken to determine via diameters. a) Original gray-scale SEM image of a 2x2 supercell. b) Complement of original image. c) Black and white image of a cropped portion of the complement image. d) Regions of interest (large vias) used for determining via diameters.

A list of all the measured pitch distances, large and small via diameters, and critical lengths for each of the lattices is shown in **Table 4.3**. Pitch lengths in the horizontal and vertical directions were determined by calculating the distances between the centroids of nearest neighbor vias. After determining the fabricated diameters and pitch lengths, both critical lengths could be calculated. Critical lengths, c_v and c_x, for each of the lattices is within 10 nm of the intended critical length of 250 nm. Standard deviation values based on the calculated via diameters and pitches are also listed in **Table 4.3**.

Table 4.3: Listing of measured pitches, via diameters, and their corresponding σ values for each lattice type. The table also includes both critical lengths for each lattice.

Lattice Type	Pitch (nm)	Large Via Diameter (nm)	Small Via Diameter (nm)	c_v (nm)	c_x (nm)
Square lattice	1100 ± 0.5	844 ± 3	-	256 ± 3	-
1x1 Supercell	1098 ± 1	842 ± 1	218 ± 3	256 ± 1	246 ± 2
2x2 Supercell	1100 ± 0.5	852 ± 9	210 ± 5	248 ± 9	247 ± 5
3x3 Supercell	1097 ± 1	844 ± 1	209 ± 3	253 ± 1	249 ± 2
4x4 Supercell	1096 ± 0.5	845 ± 5	204 ± 4	251 ± 5	250 ± 3
Average	**1098 ± 2**	**845 ± 6**	**212 ± 6**	**253 ± 3**	**248 ± 3**

Root-mean-square (RMS) roughness measurements of the Si surface were also performed at four stages of the phononic crystal fabrication process. Studies have shown that the roughness of a material's surface can reduce its thermal properties [49, 65, 66]. In the reference by Hochbaum [49], Si nanowires with diameters ranging between 115 and 50 nm had a mean roughness between 1 and 5 nm. This means the roughness was as much as 10% of the total diameter, which was the critical length. All RMS surface roughness measurements in this work were performed with an Atomic Force Microscope (AFM). A control measurement (Pre-fab Si) was the first measurement; it measured the roughness of the Si surface prior to any fabrication. Second was a slab of Si (Post-fab Si) that went through the entire fabrication process but was not processed with the FIB. The third AFM scan was performed on the wide Si slab attached to the end of the PnC after completing all fabrication steps, and this was called "Post-fab Si Slab." Last was an AFM scan of the PnC surface itself that went through the entire fabrication process (Post-fab PnC). Multiple AFM scans were made at each location. A 2nd degree polynomial was applied to level the raw data, which is the recommended technique for AFM data. **Figure 4.19** shows the results of the AFM scans along with their respective locations.

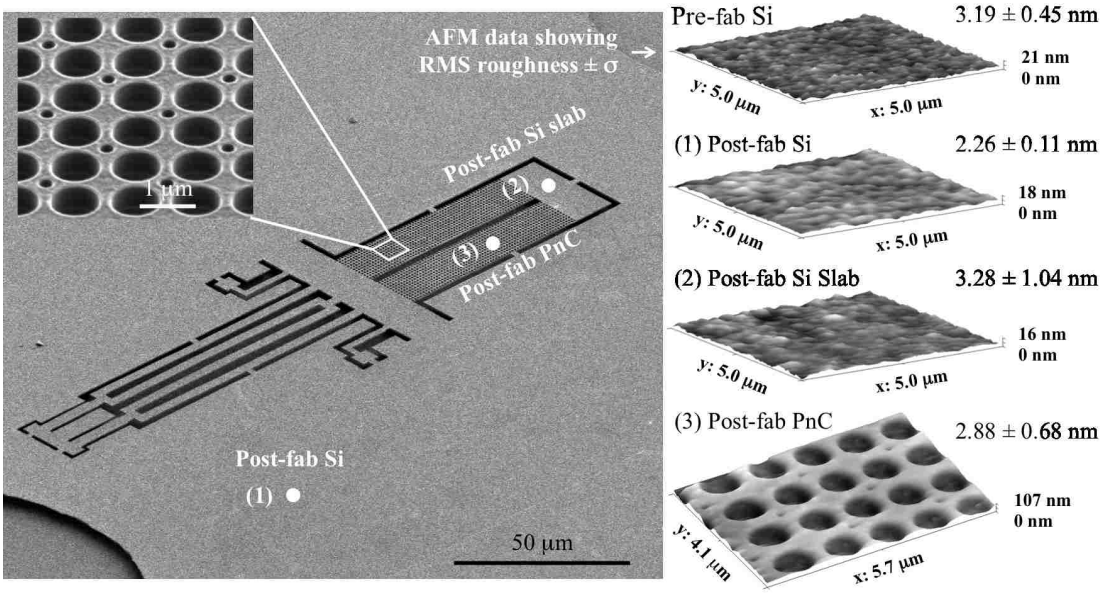

Figure 4.19: SEM image of a fully released phononic crystal after final processing at an angle of 52°. SEM image in the upper left is a zoom-in showing the surface of a 2x2 supercell at an angle of 52°. On the right are four AFM scans of various surfaces throughout the fabrication process. The number to the right of each scan is the average RMS value and standard deviation. Based on the average for all four roughness values, none of the values are more than 7 Ångstroms from the average.

Based on the average of all four RMS roughness values, none of the values were more than 0.7 nm from the average roughness of 2.90 nm, which is 1.16% of the critical length. These results show that the fabrication process does not alter the surface roughness of the Si. All of the PnCs were taken from a small Si wafer piece, each die from the Si wafer piece followed the same fabrication process, and each PnC was fabricated in the same manner. Therefore variation in the roughness of the samples is not considered a factor in interpretation of the thermal conductivity data.

5. Measurement of Thermal Conductivity of PnCs

This chapter is dedicated to describing the process of measuring the thermal conductivity of the Si/Air phononic crystals. A detailed description of the platform used to measure in-plane thermal conductivity will be given along with fabrication details. Also included is a description of how the measurements were performed. Since the platforms and PnCs were not co-fabricated, a portion of this chapter describes the transfer process.

5.1. Suspended Island Platform Description

The primary method for measuring the in-plane thermal conductivity of PnCs is carried out on a suspended island platform [67] (**Figure 5.1**). The goal of the design is to generate a thermally isolated heat source and a heat sink with one-dimensional heat flow between the source and sink via a phononic crystal. The platform design is based on previous work that measured the thermal conductivity of one-dimensional nanostructures [49, 50, 68, 69]. A thermal resistance schematic of the platform design is shown in **Figure 5.2**.

The platform consists of two silicon nitride (SiN_x) islands with a Pt resistance temperature detector (RTD) on top of each island. Joule heating of the Pt RTD generates heat on the fully suspended island. Determination of the heating island's temperature, T_H, is also performed with the Pt RTD. The other island, which is connected to the heating island by a device under test, or *DUT*, is anchored to the substrate and acts as a heat sink for the heat passing through the *DUT*. This island is called the sensing island, and its temperature, T_C, is measured with a Pt RTD as well. A detailed description of the fabrication process will be discussed later in this chapter.

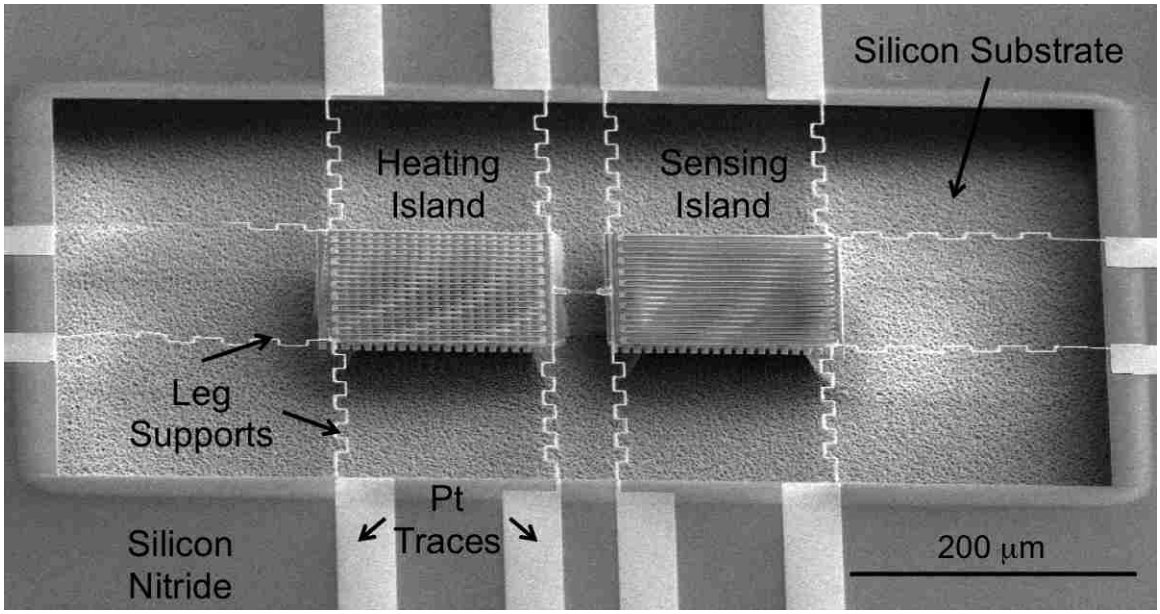

Figure 5.1: SEM image of platform used to measure in-plane thermal conductivity for phononic crystals. The platform is tilted 60 deg to show the undercut of both islands. The sensing island is partially undercut (no release holes) while the heating island is fully released (release holes).

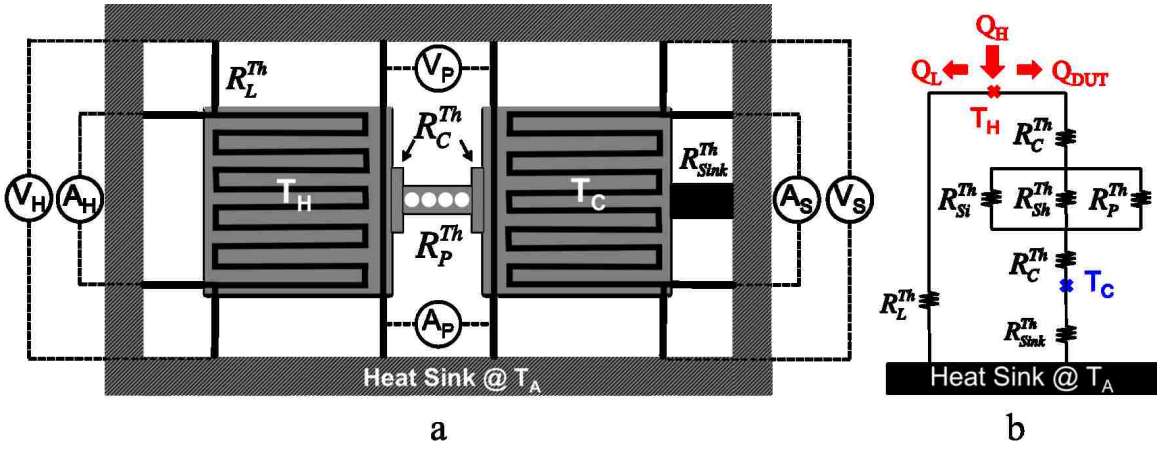

Figure 5.2: Schematics of the suspended island platform. a) Pictorial representation of a suspended island platform showing the thermal resistances, where voltages and currents are applied/measured, and each temperature location. b) Thermal circuit of suspended island platform showing all of the thermal resistances and measured temperature locations.

Each island is comprised of a 1 μm thick, low-stress (< 100 MPa tensile stress as reported by manufacturer) LPCVD silicon nitride (SiN_x) membrane, which acts as an electrically insulating support structure for the Pt RTD. The Pt RTD is a serpentine trace with a width of 2 μm and thickness of 0.2 μm. On top of the Pt RTD is a layer of

aluminum nitride (AlN). The AlN layer serves two purposes. First, its high thermal conductivity value (70 W/m-K) [70] with respect to SiN_x (3 W/m-K) [71] helps uniformly spread the heat generated by the Pt RTD across the platform. AlN is also an electrical insulator so it does not short the Pt RTD. Second, it protects the Pt traces from any FIB induced Ga doping which would alter the electrical resistivity of the Pt.

Both islands have six SiN_x leg supports or beams that are 2 μm wide. Pt traces 2 μm wide are also located on top of each leg. Two legs are used for measuring the voltage across the Pt RTD, two additional legs are used for measuring the current flowing through the Pt RTD, and the last two legs are for making electrical measurements across the PnC. All of the legs connected to the islands are designed to be equal to facilitate an easier estimation of the heat generated and lost on each leg. In the end, however, the total thermal resistance of the legs is measured directly to minimize reliance on estimated losses.

Ideally all of the heat generated by the heating island passes through the PnC to the sensing island. In actuality, this does not occur. In this setup the heat source is Joule heating of the Pt RTD, which requires electrical connections. The electrical connections require a support structure, so the electrical connections and support structure provide additional paths for heat to flow. Also, heat is not generated solely on the heating island. Heat is also generated on the two legs that supply the voltage to the heating island. Thus, it is important to minimize heat loss due to the legs and heat generated by the legs. Unfortunately these are competing processes. Minimizing heat loss requires each leg to have a high thermal resistance, R^{th}. The thermal resistance of each leg is given by

$$R_L^{th} = \frac{L_L}{\kappa_L A_L} \quad \textbf{(5.1)}$$

In **Equation (5.1)**, L is the length of the leg/beam, κ is the beam's thermal conductivity, and A is the beam's cross-sectional area. The L-subscript on each variable denotes a leg value. By increasing the length of the leg or decreasing the leg's cross-sectional area, one can increase the leg's thermal resistance.

Reducing the Joule heating on each leg, Q_L, which is given by

$$Q_L = I^2 R_L \tag{5.2}$$

requires minimizing the leg's electrical resistance, R_L. Recall that the electrical resistance of a beam of material is given by

$$R = \rho \frac{L}{A} \tag{5.3}$$

where ρ is the material's electrical resistivity. Decreasing the electrical resistance requires decreasing the leg's length or increasing the leg's cross-sectional area. Doing either one of these, however, decreases the leg's thermal resistance, which provides an easier path (smaller thermal resistance) for heat to flow to the ambient temperature heat sink.

Designing the suspended island platform takes both electrical and thermal resistances into account. Minimal heat generation on the legs/beams is achieved by making the electrical resistance of a leg at least one-tenth the electrical resistance of the Pt RTD. A long and narrow leg provides a high thermal resistance. These two requirements necessitate a relatively large suspended island. Achieving a uniform temperature over the surface of the island is aided by covering the island with AlN.

5.2. Fabrication Process

The fabrication process for the suspended islands is depicted in **Figure 5.3**. The platforms are fabricated from a silicon wafer with a 1 μm thick ultra low stress silicon nitride (SiN_x) film. The electrical connections and the Pt-RTDs on the islands are patterned using a lift-off process with an 80 nm Pt layer on top of a thin, 2 nm adhesive layer of nickel. The Ni and Pt are deposited by thermal evaporation to attain a high quality thin film platinum. The SiN_x is patterned using photolithography and etching. In this process an AlN mask is used with an O_2 and CF_4 plasma to etch SiN_x. Here the legs and main body of the islands with release holes are formed. It is notable that the cold island does not have release holes; therefore it will remain anchored to the substrate. The next step is patterning aluminum on the platforms to form the Al sample pads and bonding pads. To facilitate wire bonding the devices, 1 μm of aluminum is sputtered and lifted off. This layer also enhances the stages on the platform by decreasing contact resistance of the samples to be installed. At this stage the entire wafer except the islands is covered by photoresist, and the devices are partially released in XeF_2. Fully releasing the device at this point is detrimental to device yields due to the increased fragility of the device. However, a partial release is necessary to avoid blocking the release holes when the AlN is sputtered in the subsequent step. The next AlN layer protects the sensors from FIB and other sources of contamination. Additionally, it acts as a heat spreader on the sensor to increase the precision of the temperature readings. After deposition of AlN the devices are again partially released to ensure that the hot islands with the release holes will fully release, while the cold island is going to be anchored. Finally, the PR is stripped and the devices are fully released in XeF_2.

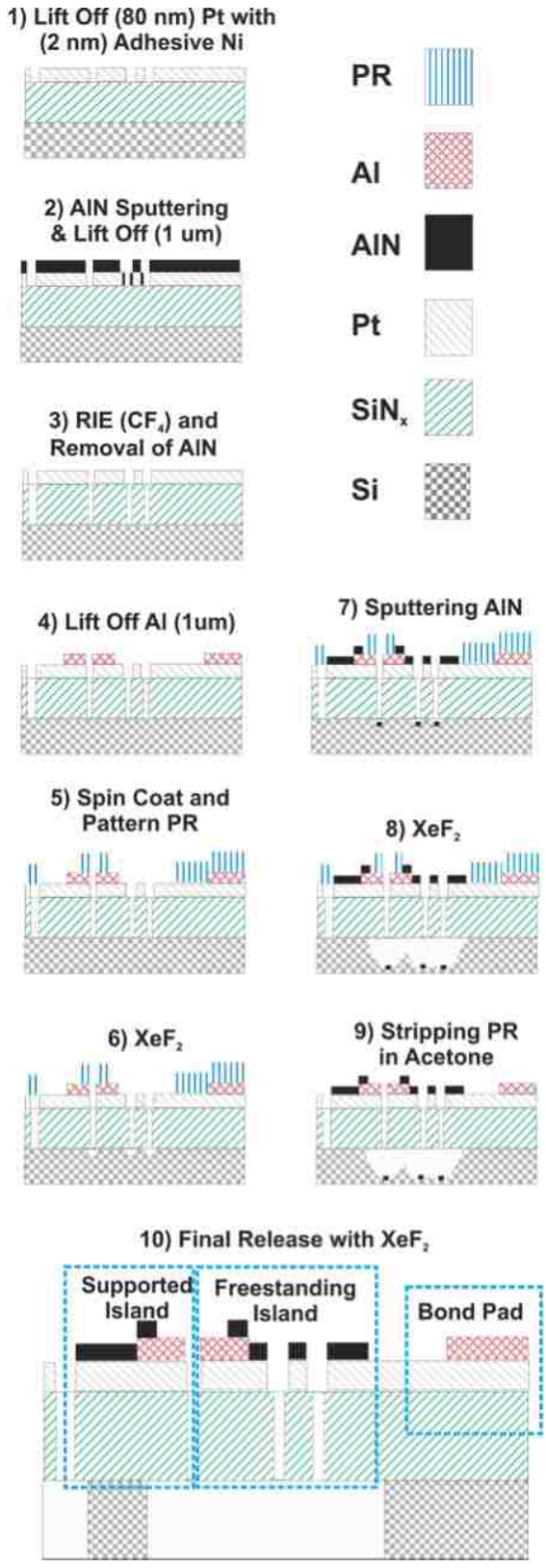

Figure 5.3: Fabrication process for suspended island platforms.

5.3. Temperature Measurements and Platform Calibration

Measuring the temperatures of each island is based on measuring the resistance of each island's Pt RTD. High accuracy electrical resistance measurements of RTDs on both the heater and sensing island are carried out using a 4-point probe technique. The relationship between electrical resistance, R, and temperature, T, is given by

$$R(T) = R_0 + R_0\alpha(T - T_0) \quad \textbf{(5.4)}$$

R_0 is the electrical resistance of the RTD at an initial temperature, T_0, and α is Pt's temperature coefficient of resistance (TCR). Calibration of the RTD's will be discussed in detail later. A voltage is applied to each island using two of the legs connected to each island. Two additional legs are used to measure the current passing through the RTD.

Over a small range of temperature, there is a linear relationship between a material's electrical resistance and temperature. The relationship is given by

$$R(T)=R_0 + R_0\alpha\Delta T \quad \textbf{(5.5)}$$

$R(T)$ is the electrical resistance of the RTD, T is the temperature, R_0 is the RTD's initial electrical resistance at T_0, and α is the temperature coefficient of resistance (TCR). During calibration $R(T)$ is measured, T is the independent variable, and α is determined from a plot of $R(T)$ vs temperature (**Figure 5.4**). A look at various TCR values stated in literature shows the importance of calibration. For bulk Pt the TCR is 0.0039083 K^{-1} [72]. This value changes, however, for Pt thin films. Zhang measured a TCR value of 0.0014 K^{-1} for a 28 nm thin film of Pt [73], and Shi measured a value ranging between 0.0018 and 0.0036 K^{-1} for a 30 nm thin film of Pt [50]. Without calibration, it would be impossible to know what TCR value to use.

Calibration of each platform is performed under vacuum pressure with temperature-controlled heater. Knowing both the temperature and electrical resistance of the Pt-RTD at a given temperature, the TCR for each platform can be determined from **Equation (5.5)** by solving the equation for α.

$$\alpha = \frac{(R - R_0)}{R_0 \Delta T} \quad \textbf{(5.6)}$$

Plotting the change in electrical resistance as function of the change in temperature yields a linear plot with the slope of the line equal to α. The temperature of the system is determined by a 4-point Pt RTD attached to the top surface of the ceramic chip carrier. The ceramic chip carrier is bonded to the copper heater with a thermally conductive silver paste. At each temperature voltage and current measurements are taken only after the system stays within ± 0.2 °C of the set temperature for two minutes. This is done to ensure equilibrium of the system. Multiple measurements are performed at each temperature, and the temperature is ramped up and down multiple times to achieve a statistical average. Calibration is performed at high vacuum (< 20 μTorr) to minimize heat loss through convection. Extensive work was done to show the effect of pressure on the calibration results. It was found that below 1 mTorr the recorded value for α does not change, i.e. convection no longer changes the measurement. Pressures less than 20 μTorr were chosen for experiments because this pressure is two orders of magnitude lower than the value where convection affects results. There is a 6% difference between performing calibration at atmospheric pressures and the μT region (**Figure 5.4**). This difference can lead to an incorrect temperature reading that varies by more than 1 K. In order to ensure linearity between resistance and temperature, the temperature rise on the heating island is

below 10 K and often kept near 5 K. Therefore an error of 1 K can be as much as 20% of the measured value.

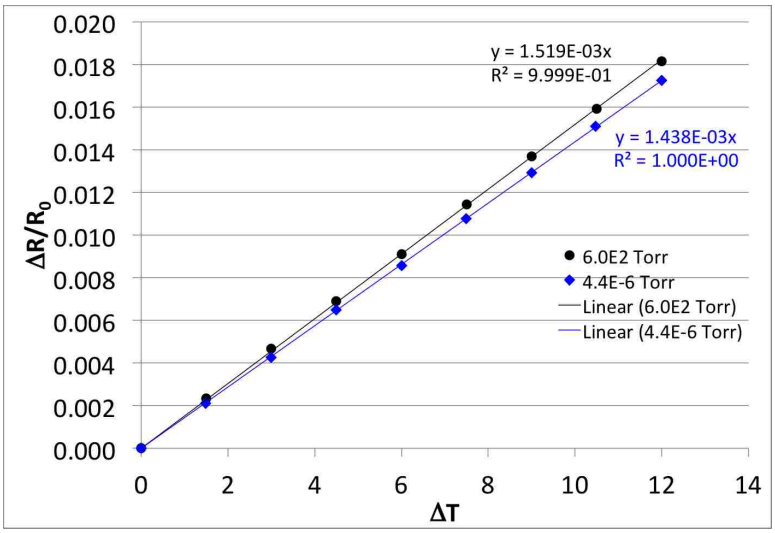

Figure 5.4: Effect of pressure on platform calibration. Atmospheric data is shown as black dots, and data taken at 4 μTorr is shown as blue diamonds. The slope of each line is equal to the measured TCR value. There is a 6% difference in the measured values.

5.4. Transfer Process

All of the PnCs mentioned were fabricated on a separate die or chip, and each one was transferred to a suspended island platform. SEM images taken during the transfer process are shown in **Figure 5.5**.

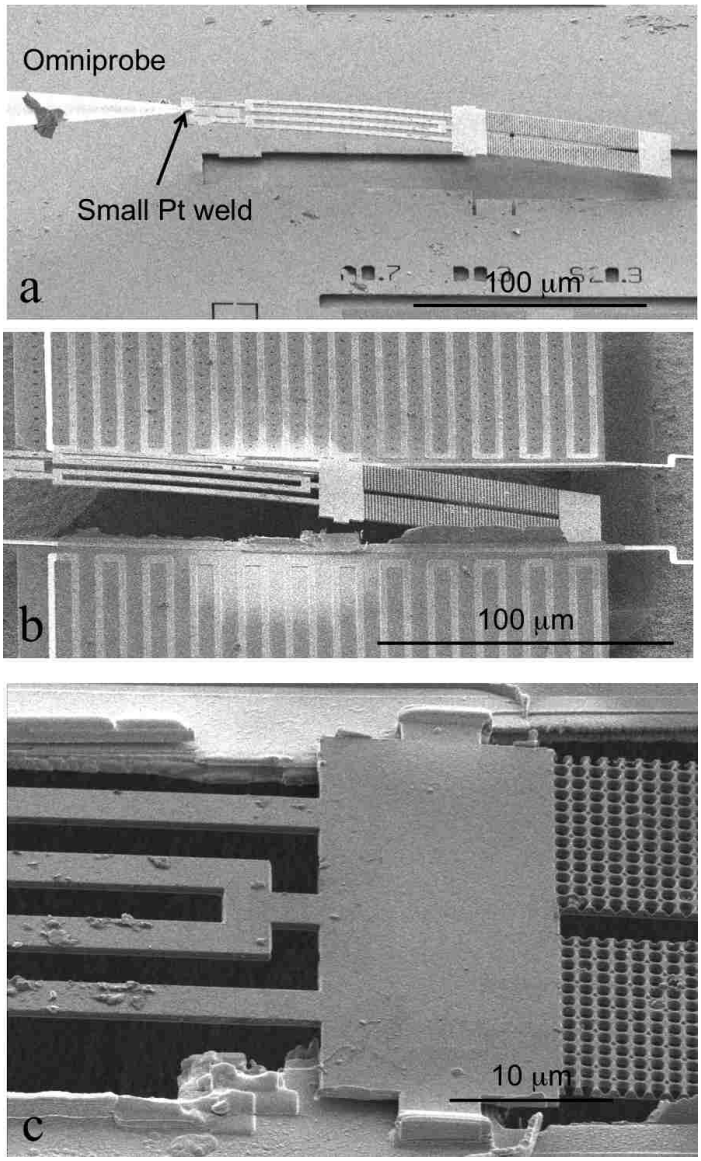

Figure 5.5: SEM images of the transfer process. a) A PnC is removed from its resting position with the Omniprobe by using a small Pt weld. b) The PnC is placed onto the contact pads of both heating islands. c) The PnC is welded in place with FIB-deposited Pt.

The transfer process was performed with the Omniprobe attached to the FIB system. An Omniprobe is a micron-sized tungsten probe that can be inserted into the FIB/SEM vacuum chamber. It acts as a tiny 'finger' with precise motion in *x*, *y*, and *z* directions. By using the FIB, Omniprobe, and Pt GIS, each PnC was attached to the Omniprobe by depositing a small amount of Pt and then transferred to the suspended island platform. **Figure 5.5a** shows the Omniprobe lifting a PnC from the die on which it was fabricated.

Next, the PnC is transferred with the Omniprobe to the suspended island platform and aligned with the heating and sensing island. **Figure 5.5b** shows the PnC, which is still connected to the Omniprobe, being placed on to the contact pads. Connecting the PnC to the platform also required deposition of Pt. Once the PnC was in place, Pt was deposited on the contact area to physically attach the PnC to the platform and make a thermal connection between the island and PnC, and **Figure 5.5c** shows the Pt welds connecting the PnC and contact pads. **Figure 5.6** shows an overview of a successful transfer of a PnC to a suspended island platform. The image on the right hand side is a close-up image of the connection that is made between the sample and platform.

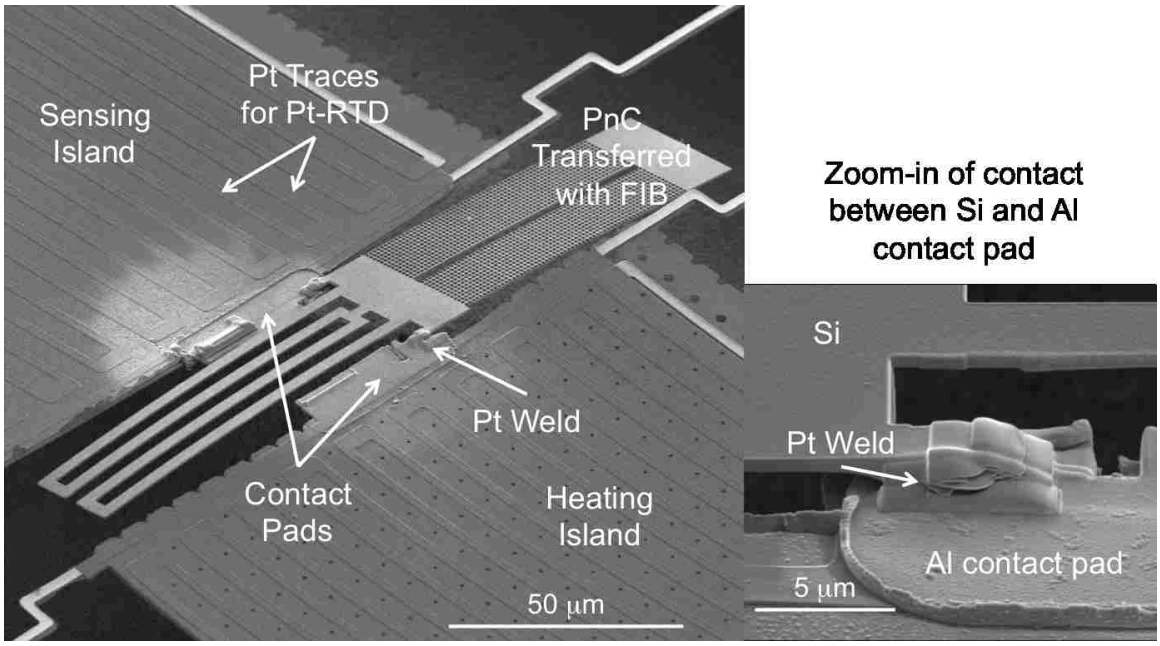

Figure 5.6: SEM images of a PnC connected to suspended island.

Once the PnC was successfully transferred, the next step is to measure the thermal conductivity of the PnC.

5.5. Sample Description

Each sample transferred to the suspended island platform contains three portions; a short, a Si slab, and a PnC. From a thermal resistance standpoint, all three portions are

in parallel. The short is necessary to measure the thermal contact resistance that occurs when the PnC is welded to the platform. It is designed to have a small thermal resistance with respect to the Si island and PnC. As is the case with electrical resistors in parallel, most of the heat will pass through the smallest thermal resistance with a minimal amount of heat passing through the larger thermal resistances. When the sample is welded to the islands, Pt is deposited with the FIB to anchor the sample in place, and the amount of thermal resistance that is created is unknown. Previous studies that used the suspended island technique measured the thermal conductivity of nanowires, which had a small cross-sectional area [49, 50, 68, 69]. Thus, the nanowire thermal contact resistance was negligible since thermal resistance is inversely proportional to cross-sectional area. In this case, however, the contact resistance cannot be neglected. The second portion of the sample contains a long Si slab. It was used as the reference sample for normalizing the thermal conductivity of the PnC, which is the third portion of the sample.

5.6. Thermal Resistance Measurements

Measuring the thermal conductivity of the PnC is dependent on measuring multiple thermal resistances, R_M^{Th}.

$$\Delta T = \dot{Q}_H R_M^{Th} \quad \textbf{(5.7)}$$

In **Equation (5.7)**, ΔT is the measured temperature difference and $\dot{Q}_H$ is the applied power. Plotting ΔT vs. $\dot{Q}_H$ provides a value for R_M^{Th}. Whenever a measurement is made, the measured thermal resistance takes into account all of the thermal components. In the first measurement (**Figure 5.7a**), which is performed when there is no sample connecting the islands, the leg resistance, R_L^{Th} is measured.

$$R_{Ma}^{Th} = R_L^{Th} \quad \textbf{(5.8)}$$

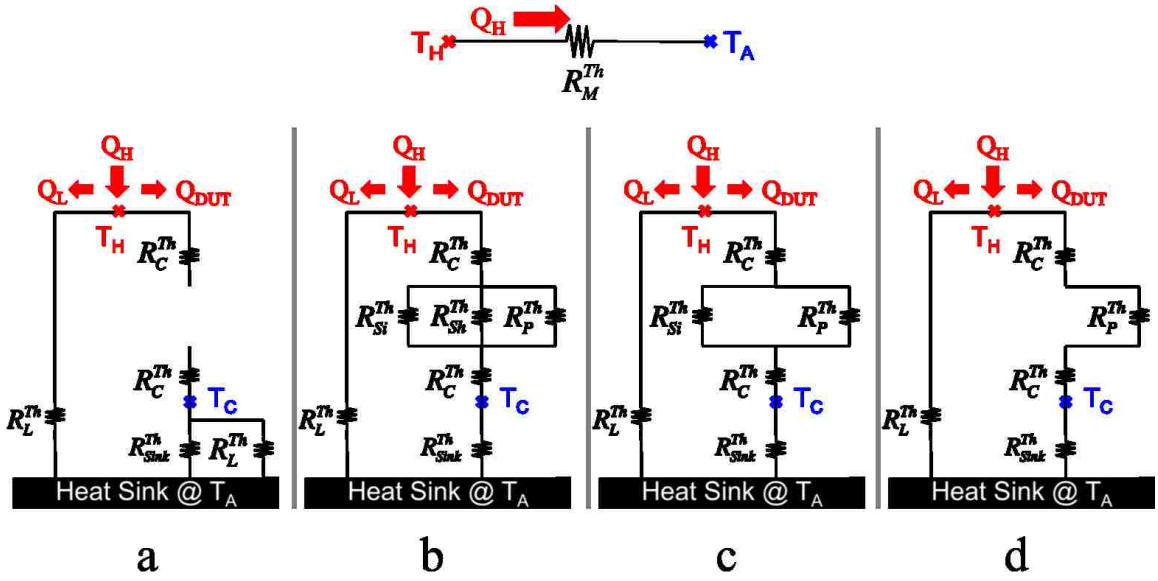

Figure 5.7: 4-step measurement process for determining the thermal conductivity of the PnC Top of figure represents simplified thermal resistance measurement a) Measure thermal resistance of leg b) Measure thermal resistance of contacts c) Measure thermal resistance of Si slab. d) Measure thermal resistance of PnC

The next measurement (**Figure 5.7b**) occurs with a sample connecting the two islands. This measurement is used to determine the contact resistance, R_c^{Th}.

$$\frac{1}{R_{Mb}^{Th}} = \frac{1}{R_L^{Th}} + \frac{1}{R_c^{Th}+R_{DUT}^{Th}} \approx \frac{1}{R_L^{Th}} + \frac{1}{R_c^{Th}} \qquad (5.9)$$

In **Equation (5.9)**, the *DUT* thermal resistance, R_{DUT}^{Th}, is comprised of the Si slab's thermal resistance, R_{Si}^{Th} , the short, R_{Sh}^{Th}, and the PnC, R_P^{Th}. The short is designed such that its thermal resistance is much smaller than the PnC or Si matrix, so that the thermal resistance of the sample is equivalent to the short. In the initial calculation, it is assumed that the short can be neglected. Measurements of the contact thermal resistance and short thermal resistance ultimately show that $R_c^{Th}$is at least 20 times greater than R_{Sh}^{Th}. Prior to the final analysis, however, the thermal resistance of the short is taken into account.

The third measurement (**Figure 5.7c**), is used to calculate the thermal resistance of the Si slab, R_{Si}^{Th}.

$$\frac{1}{R_{Mc}^{Th}} = \frac{1}{R_L^{Th}} + \frac{1}{R_c^{Th} + \frac{1}{\frac{1}{R_{Si}^{Th}} + \frac{1}{R_P^{Th}}}} \quad \textbf{(5.10)}$$

The fourth and final measurement (**Figure 5.7d**), is necessary to measure the thermal resistance of the phononic crystal, R_P^{Th}.

$$\frac{1}{R_{Md}^{Th}} = \frac{1}{R_L^{Th}} + \frac{1}{R_c^{Th} + R_P^{Th}} \quad \textbf{(5.11)}$$

With four **Equations (5.8)**, **(5.9)**, **(5.10)**, and **(5.11)** and four unknowns, R_L^{Th}, R_c^{Th}, R_{Si}^{Th}, and R_P^{Th}, each thermal resistance can be determined. Combining the thermal resistances with the measured geometries of the Si slab and the phononic crystal, thermal conductivity values for Si and the PnC can be calculated.

In between each measurement, the sample is taken to the FIB to make various cuts to alter the path of the heat flow. Between measurement 2 and 3, the short is cut so that the heat energy then flows through the Si slab and the PnC. After measurement 3, the Si slab is cut and leaves the PnC as the only path for the heat energy to flow. Care is taken during the cutting process to minimize exposure of the bare Si to additional ion implantation, which can potentially change the thermal conductivity of the sample. To avoid such damage, a minimal current of 30 pA is used for cutting the specimen. Moreover, during the transfer process, imaging with the FIB was minimized.

In order to estimate the effect of ion imaging that inevitably occurs during the transfer process, an experiment was performed on one of the samples after the necessary data had been collected. With the specimen welded between the islands, a portion of the Si slab was imaged for 5 minutes with 30 pA. This is much longer than the time a

specimen is typically imaged by the FIB during a transfer process. The measurements of thermal resistance before and after this intentional damage showed no difference. Another experiment was performed by milling one of the sides of the Si slab with the FIB, and again there was no change in Si's thermal resistance. Based on these two experiments, neither the transfer process nor the cutting of the sample between measurements induces detectable damage to the samples.

5.7. Measurement Setup

Images of the setup are shown in **Figure 5.8**. The wire bonded sample shown in **Figure 5.8a** contains the suspended island platform. Wire bonds connect the sample to the gold contacts on an 84-pin ceramic chip carrier. The chip carrier is mounted in a breakout board that allows for external connections to be made to the sample, and the entire setup is placed inside a vacuum chamber. Multiple ports located around the edge of the vacuum chamber allow connection of a turbo pump, connections to the temperature controller, and connectivity to various multi-meters and power supplies (**Figure 5.8**). LabVIEW is used to automate all of the data collection.

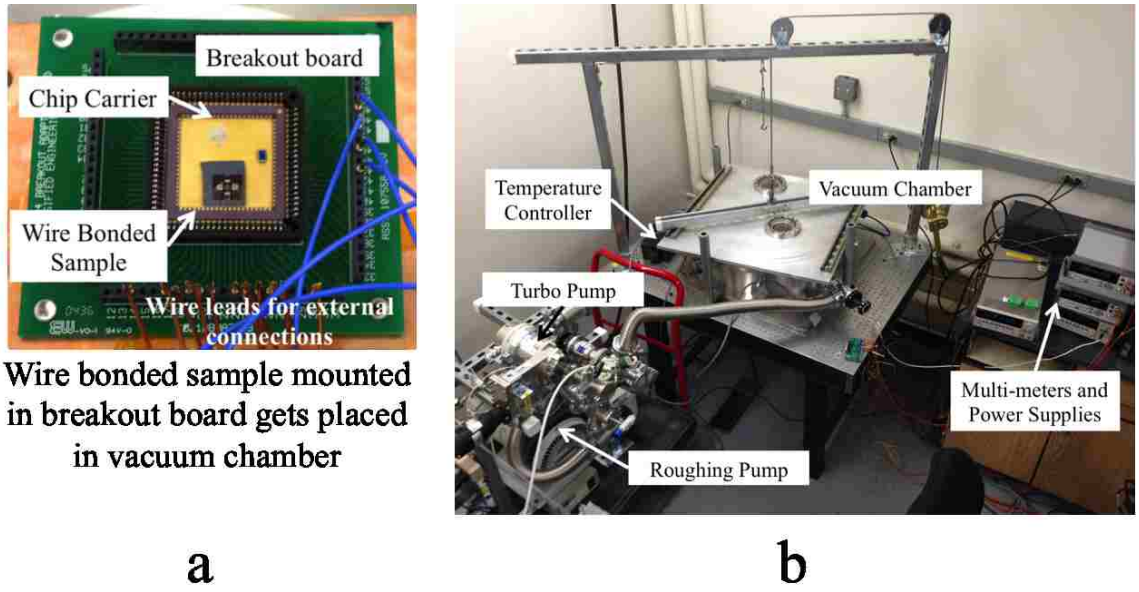

Figure 5.8: Overview of the breakout board assembly and vacuum chamber setup. a) Wire bonded sample mounted on a chip carrier inserted into the breakout board. b) Vacuum chamber setup with pumps and electrical components connected.

6. Measurement Results and Discussion

This chapter reports the fabrication results and thermal conductivity values. Fabrication results are discussed first. Next the thermal conductivity measurements are shown. The last part of the chapter discusses the significance of the measurements and their implications on coherent scattering of phonons in silicon.

6.1. Fabrication Results

First, it is important to note the variation in the porosity and critical lengths. If there is large variation in these lengths, then it is not possible to properly compare the thermal conductivity values of the unit cells together. Proof is given that there is minimal geometrical variation among the unit cells and also minimal variation on a single sample.

Excellent accuracy was achieved with the diameters of the vias milled with the FIB. **Table 6.1** lists the measured pitches, diameters, and corresponding critical lengths. There is a maximum difference of 8 nm in the critical length, c_v, and only 4 nm in the critical length, c_x. Based upon the mean value, however, there is a spread of only 5 nm in c_v and 2 nm in c_x. These last two lengths correspond to a critical length difference of 2% or less from their respective mean values.

Table 6.1: List of measured pitches and diameters for all unit cells.

Lattice Type	Pitch (nm)	Large Via Diameter (nm)	Small Via Diameter (nm)	c_v (nm)	c_x (nm)	3D Porosity, ϕ
Square lattice	1100 ± 7	844 ± 3	-	256 ± 3	-	0.484 ± 0.009
1x1 Supercell	1098 ± 1	842 ± 1	218 ± 3	256 ± 1	246 ± 2	0.520 ± 0.001
2x2 Supercell	1100 ± 6	852 ± 9	210 ± 5	248 ± 9	247 ± 5	0.510 ± 0.010
3x3 Supercell	1097 ± 1	844 ± 1	209 ± 3	253 ± 1	249 ± 2	0.498 ± 0.001
4x4 Supercell	1096 ± 5	843 ± 5	201 ± 4	253 ± 5	253 ± 3	0.494 ± 0.004
Average	**1100 ± 6**	**845 ± 6**	**211 ± 6**	**255 ± 9**	**249 ± 7**	**-**

Variation in dimensions over a single PnC showed similar results. Based on the measurement of 560 large vias and 360 small vias for the 2x2 supercell, the standard

deviations for c_v and c_x are 3.6 and 2.4%, respectively. Dimensions for the 2x2 supercell are listed in **Table 6.2**.

Table 6.2: List of measured diameters with standard deviations for the 2x2 supercell. Each supercell required 10 patterns to be stitched together.

Pattern	# Large Vias	Lattice Constant (nm)	Large Via Diameter (nm)	# Small Vias	Small Via Diameter (nm)	c_v (nm)	c_x (nm)
1	56	1100 ± 6	851 ± 8	36	217 ± 4	249 ± 14	243 ± 9
2	56	1100 ± 4	847 ± 5	36	207 ± 2	253 ± 9	251 ± 6
3	56	1099 ± 4	843 ± 4	36	205 ± 2	256 ± 8	254 ± 5
4	56	1099 ± 6	845 ± 7	36	206 ± 3	254 ± 13	252 ± 8
5	56	1099 ± 5	848 ± 6	36	207 ± 4	251 ± 4	250 ± 8
6	56	1100 ± 6	857 ± 7	36	218 ± 4	243 ± 13	240 ± 9
7	56	1100 ± 4	848 ± 5	36	206 ± 3	251 ± 8	250 ± 6
8	56	1100 ± 4	845 ± 5	36	205 ± 2	254 ± 9	252 ± 6
9	56	1100 ± 11	873 ± 14	36	212 ± 2	228 ± 25	238 ± 14
10	56	1099 ± 7	865 ± 10	36	216 ± 3	234 ± 17	237 ± 10
Avg		**1100 ± 6**	**852 ± 12**		**210 ± 6**	**247 ± 9**	**247 ± 6**

Three dimensional porosity values, based on the measured via diameters, showed a maximum difference of 3.3%. This is the exact same difference calculated in Chapter 3, which assumed no variation in the via diameters. A graph of the 3D porosity values, both desired (blue squares) and measured (black circles), is plotted in **Figure 6.1**. All measured values are within 0.8% of the desired porosities.

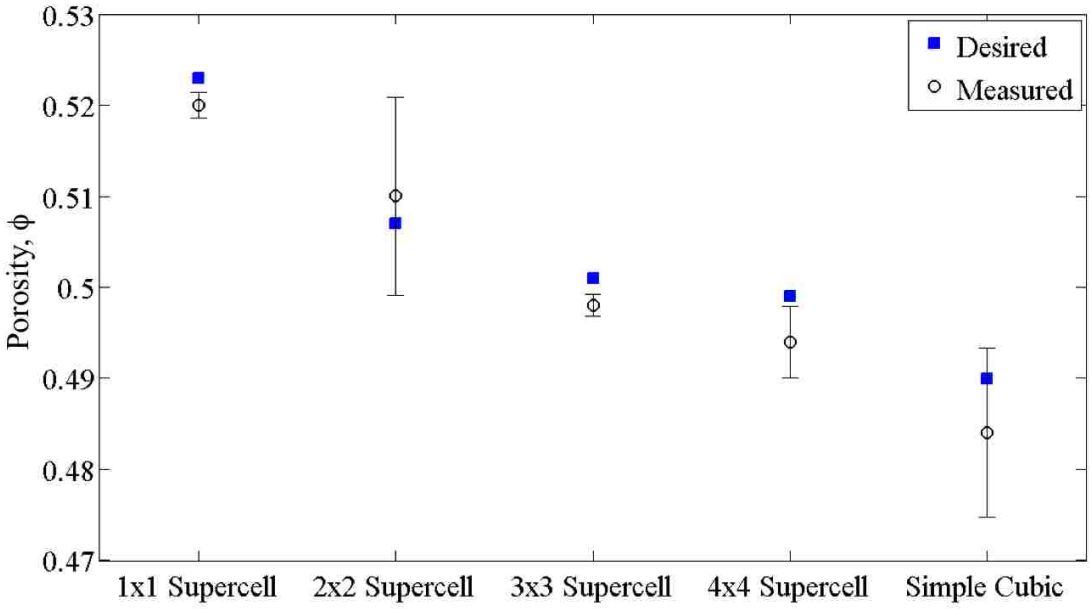

Figure 6.1: Plot of 3D porosity values with associated error. Desired values are blue squares and measured porosities are black circles. The maximum difference between porosity values is 3.3%. A comparison between desired and measured porosities for each PnC shows less than a 0.8% difference.

Next, it is shown that deposition of Ti protected the Si from ion implantation. After removing the Ti protective layer and releasing the sample with vapor HF, energy-dispersive x-ray spectroscopy (EDS) results with a 10kV electron beam showed no detectable Ga present even over the region where the pattern was milled (**Figure 6.2**).

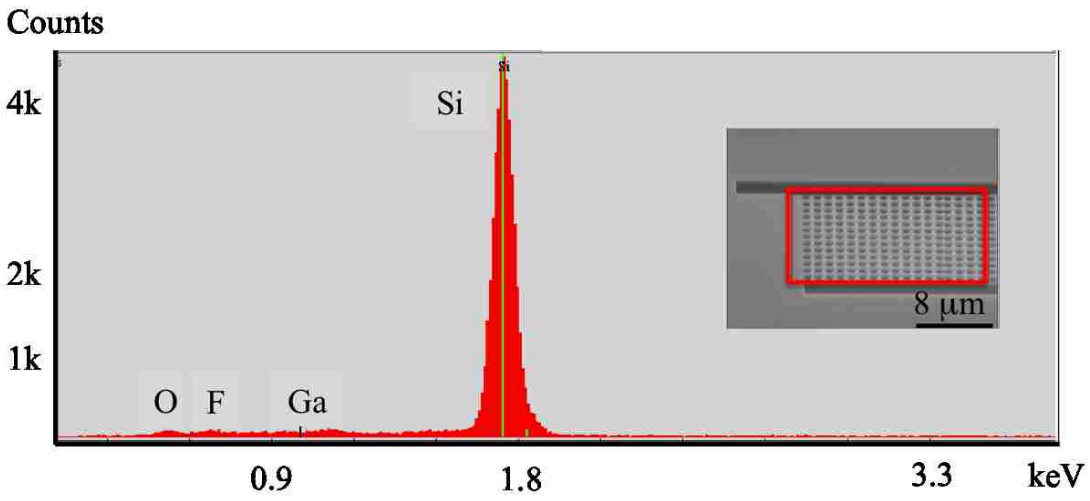

Figure 6.2: EDS results. The large red peak in the plot is the signal from Si. The Ga signature, which is almost non-existent, is slightly above 0.9 keV. The scanned area is the red box shown in the inset.

6.2. Measurement Results

Last, the thermal conductivity results are shown, which include the Si slab values and the phononic crystal values. **Table 6.3** lists the measured thermal conductivity values for each PnC along with its corresponding porosity. A plot of the relative thermal conductivity values is show in **Figure 6.3**.

Table 6.3: Measured thermal conductivity values including error. Table also lists each phononic crystal's porosity.

PnC	Porosity ϕ (3D)	κ_{Si} (W/m K)	% Error	κ_{PnC} (W/m K)	% Error	κ_{rel}	% Error
Square lattice	0.484	65.5	4.2	14.4	1.4	0.220	4.6
4x4 Supercell	0.491	61.1	4.0	12.8	2	0.210	4.0
3x3 Supercell	0.495	70.1	6.0	13.6	3	0.194	6.0
2x2 Supercell	0.510	64.3	6.0	12.4	3	0.192	5.0
1x1 Supercell	0.517	55.6	6.0	10.0	3	0.180	6.0

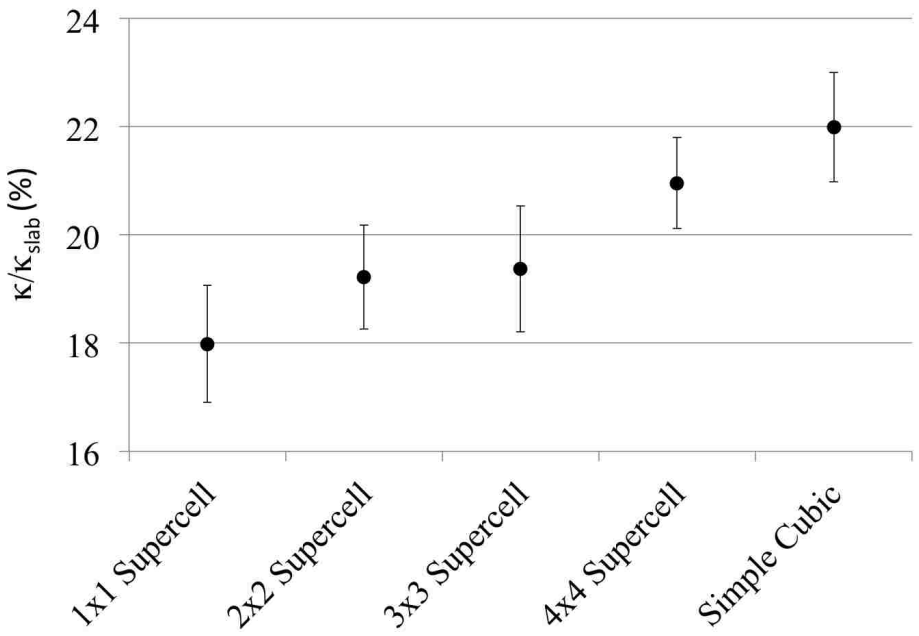

Figure 6.3: Plot of relative thermal conductivity values with associated error for each PnC.

In order to determine measurement variation for a given unit cell, two 3x3 supercells with thicknesses near 434 nm were fabricated. Due to fabrication and measurement difficulty, only two were fabricated. The measured supercell dimensions are listed in **Table 6.4**.

Table 6.4: Measured dimensions for the supercells used to evaluate variation for a given unit cell.

3x3 Supercell	t (nm)	a (nm)	Large Via Diameter (nm)	Small Via Diameter (nm)	c_y (nm)	c_x (nm)	3D Porosity, ϕ
A	432 ± 4	1097 ± 3	844 ± 3	217 ± 5	256 ± 5	247 ± 4	0.499 ± 0.004
B	436 ± 4	1099 ± 4	845 ± 2	217 ± 3	254 ± 4	246 ± 3	0.502 ± 0.004
Average	**434 ± 4**	**1098 ± 4**	**844 ± 3**	**217 ± 4**	**253 ± 4**	**246 ±4**	

A look at the maximum difference among all the critical lengths for these two supercells reveals a difference of 10 nm. Comparing a single critical length, say c_x, shows a difference of only 1 nm. Their porosity values differed by 0.3%. Due to their nearly identical dimensions, critical length and porosity can be neglected when comparing measured thermal conductivity values for these two supercells.

Measuring the thermal conductivity for the two 3x3 supercells, A and B, followed the procedure described in Chapter 5. All of the measured thermal conductivity values and their associated errors are listed in **Table 6.5**. The relative thermal conductivity of the two samples differed by 1.3%, which points to low variation across multiple samples. Based on the small variation of the relative thermal conductivities for these two supercells, it is assumed similar variations would occur for any other fabricated supercell.

Table 6.5: Measured thermal conductivity values, including error, for 3x3 supercells A and B.

3x3 Supercell	κ_{Si} (W/m K)	% Error	κ_{PnC} (W/m K)	% Error	κ_{rel}	% Error
A	73.3	15	10.6	3.0	0.144	16
B	56	5.0	8.9	5.0	0.157	6.0

6.3. Discussion of Results

A look at **Figure 6.3** shows a trend with the relative thermal conductivity values for the PnCs. The *x*-axis in the graph, however, is arbitrary since it lists the name of each PnC. Changing the order of the names would alter the trend. A more instructive graph plots relative thermal conductivity with respect to a measurable independent value such as critical length or porosity. Both parameters affect thermal conductivity, and both will be used.

Analysis of the thermal conductivity values needs to take into account the effect of porosity and phonon scattering. The phonon scattering includes incoherent boundary scattering and any possible coherent scattering. COMSOL takes into account the effect of porosity. Both incoherent and coherent phonon scattering can be accounted for in the hybrid lattice dynamics-continuum mechanics simulations [25].

All phononic crystals used in this work are comprised of a square lattice pattern with holes of fixed diameter, so it will serve as the basis pattern for comparing results.

By normalizing all values to the square lattice, it will be easier to observe the effect of the pattern on silicon's thermal conductivity. This is justified by the fact that all of the PnCs, not unit cells, are the same size and have nearly identical critical lengths.

When comparing thermal conductivity values to critical length, a decrease in the critical length leads to a lower thermal conductivity value. On a scale where a structure's critical length is similar to or smaller than the size of the bulk material's phonon mean free path, a decrease in the critical length leads to lower thermal conductivity values [17, 41, 49, 74]. In this regime, boundary scattering plays a critical role in a material's thermal conductivity. By confining the phonons within a small region, there is a greater chance for the phonons to scatter off the surface boundaries and reduce the thermal conductivity of the material. As the critical length decreases, the probability of phonon boundary scattering increases which results in a decrease in thermal conductivity. Over a small range of length values, the relationship between the expected thermal conductivity, κ_{PnC}^{c}, and critical length can be approximated as a linear function.

$$\kappa_{PnC}^{c} = \kappa_{ref} \frac{c}{c_{ref}} = \kappa_{ref} \left(1 + \frac{\Delta c}{c_{ref}}\right) \quad \textbf{(6.1)}$$

In Equation **(6.1)** *c* refers to the minimum critical length and the subscript *ref* refers to reference sample while the subscript *PnC* refers to the phononic crystal being compared to the reference sample. *Δc* is the difference in critical length between the PnC and the reference sample. In all cases the reference sample will be the square lattice phononic crystal. A graph showing the measured values as function of change in critical length is shown in **Figure 6.4**. If the scattering in the PnC were only incoherent scattering, then it is expected that the measured values would change monotonically as a function of critical length. Although there is variation in the thermal conductivity values with respect to

critical length, the trend in the measured values does not follow the expected results. As the critical length increases, the measured thermal conductivity values increase and then decrease. From this graph, changes in critical length do not accurately describe the variation in the measured thermal conductivity values.

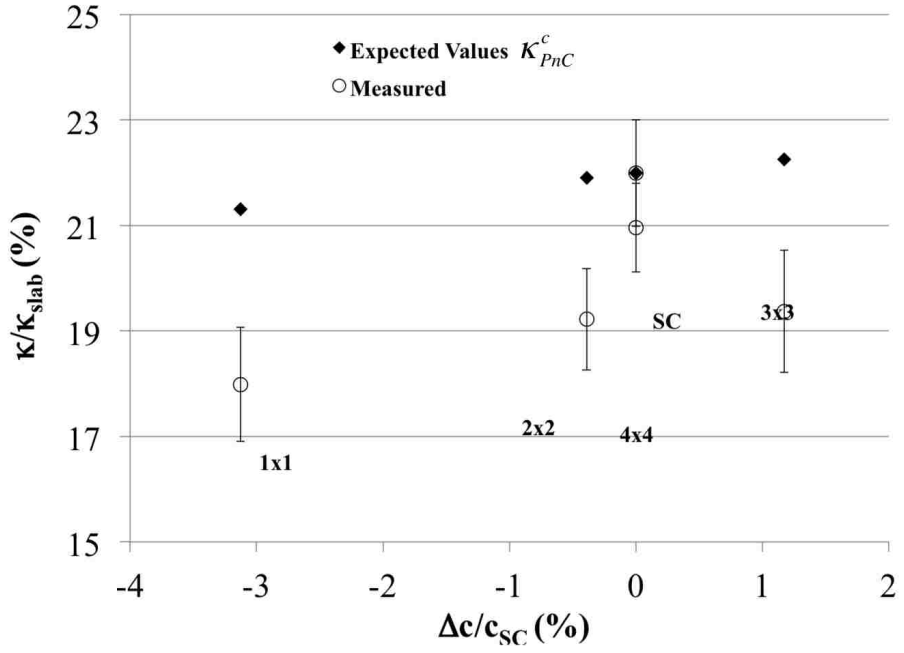

Figure 6.4: Graph of expected thermal conductivity values based on critical length. All expected values (black diamonds) are normalized to the critical length of the square lattice PnC. Measured values (black circles) with their respective errors are also plotted.

Porosity, ϕ, also alters silicon's thermal conductivity. As porosity increases, a material's thermal conductivity decreases. It is assumed that the phonons experience diffuse scattering at the boundaries of the vias, which was also assumed for previous microporous and nanoporous materials [15, 28, 37, 75]. Diffuse scattering at the pore boundaries can also be assumed based on the small fraction of phonons being specularly scattered [36, 75, 76]. There are various approximations to estimate the effect of porosity on a material's thermal conductivity [42 43, 44, 75]. In each of these references, no coherent scattering is assumed. Both References 28 and 37 used expressions, $f(\phi)$, from Russell [42]

and Eucken [43] to estimate the effect of porosity on micro/nanoporous solids. References 44 and 75 used a Maxwell-Garnett expression to determine the effective thermal conductivity of a porous material. A graph of the various approximations along with their porosity values is shown in **Figure 6.5**. In this graph all of the approximations are plotted as a function of change in porosity from the square lattice's (simple cubic) porosity. The *y*-axis shows the thermal conductivity values relative to a slab of silicon with a thickness equal to that of the PnC.

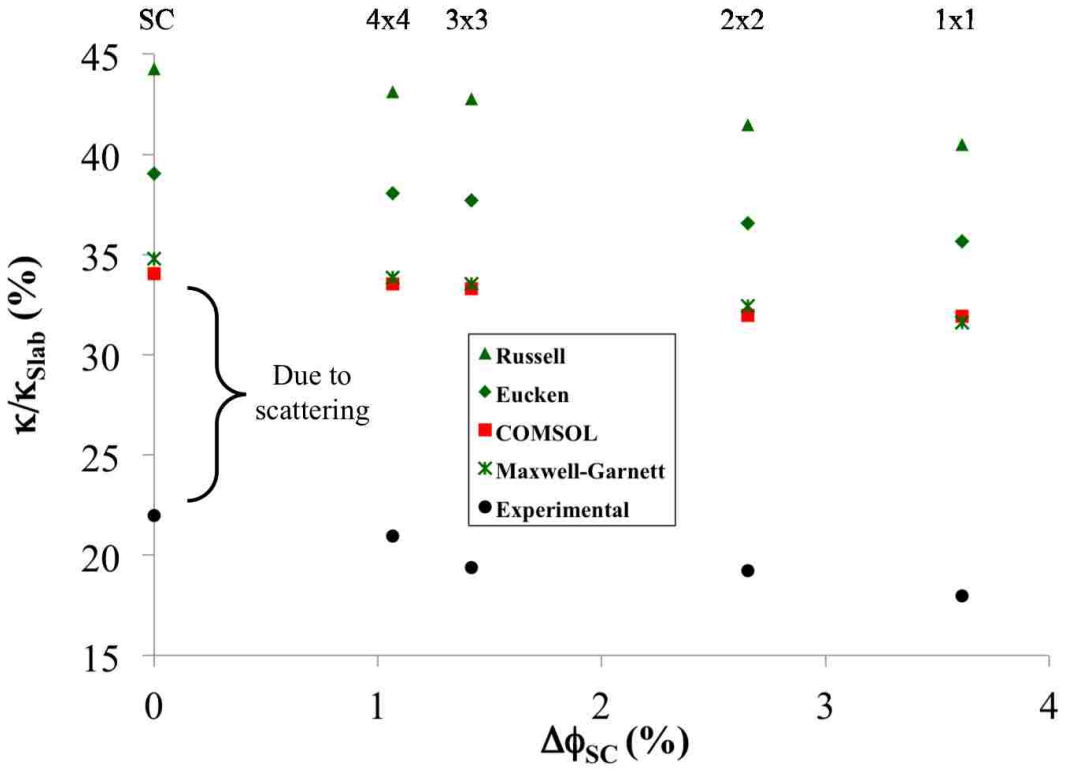

Figure 6.5: Graph showing the various approximations for estimating porosity's effect on thermal conductivity. The black dots are experimental values.

Maxwell-Garnett provided the best estimate of the effect of porosity since it closely followed the COMSOL results. The Maxwell-Garnett expression for a two-dimensional composite with circular pores is [44]

$$f(\phi) = \frac{1-\phi}{1+\phi} \quad \textbf{(6.2)}$$

The difference between the COMSOL results and the measured results is based on scattering, whether it is incoherent or coherent. Determining if there is any potential coherent scattering is the next step.

All of the fabricated PnCs have nearly identical critical lengths, and so it is safe to assume all of them have similar amounts of incoherent scattering. Recall that incoherent scattering is captured in simulations via a phonon scattering relaxation time that is dependent on critical length. If incoherent scattering is the only type of scattering affecting the thermal conductivity of the PnCs, then any differences among the fabricated supercells should be equal to differences in their porosities. Using the fact that the ratio of two relative thermal conductivity values is equal to the ratio of their porosity functions,

$$\frac{\kappa_{PnC}^{\phi}}{\kappa_{ref}^{\phi}} = \frac{f(\phi_{PnC})}{f(\phi_{ref})} \quad \textbf{(6.3)}$$

an expression for the expected thermal conductivity based on porosity, κ_{PnC}^{ϕ}, can be derived. This relationship is shown in **Equation (6.4)**.

$$\kappa_{PnC}^{\phi} = \frac{f(\phi_{PnC})}{f(\phi_{ref})}\kappa_{ref} \quad \textbf{(6.4)}$$

In a similar fashion to critical length, a linear relationship between porosity and thermal conductivity can be assumed over a small range of porosity values. The reference in **Equation (6.4)** will be the square lattice PnC. **Figure 6.6** shows a graph of the relative

thermal conductivity values (blue diamonds) as a function of change in porosity from the square lattice. The measured values with their corresponding errors (black circles) are plotted as well. As porosity increases, the measured values diverge from the expected values. Since porosity and incoherent scattering are taken in to account, the only thing left is coherent scattering. A look at the 1x1 supercell shows that its thermal conductivity is only 80% of the square lattice, and only 10% of that difference is accounted for through porosity and incoherent scattering. The remainder is due to coherent scattering, which stems from changes in the phonon dispersion. The change in the phonon dispersion is due to presence of the periodic supercell structure.

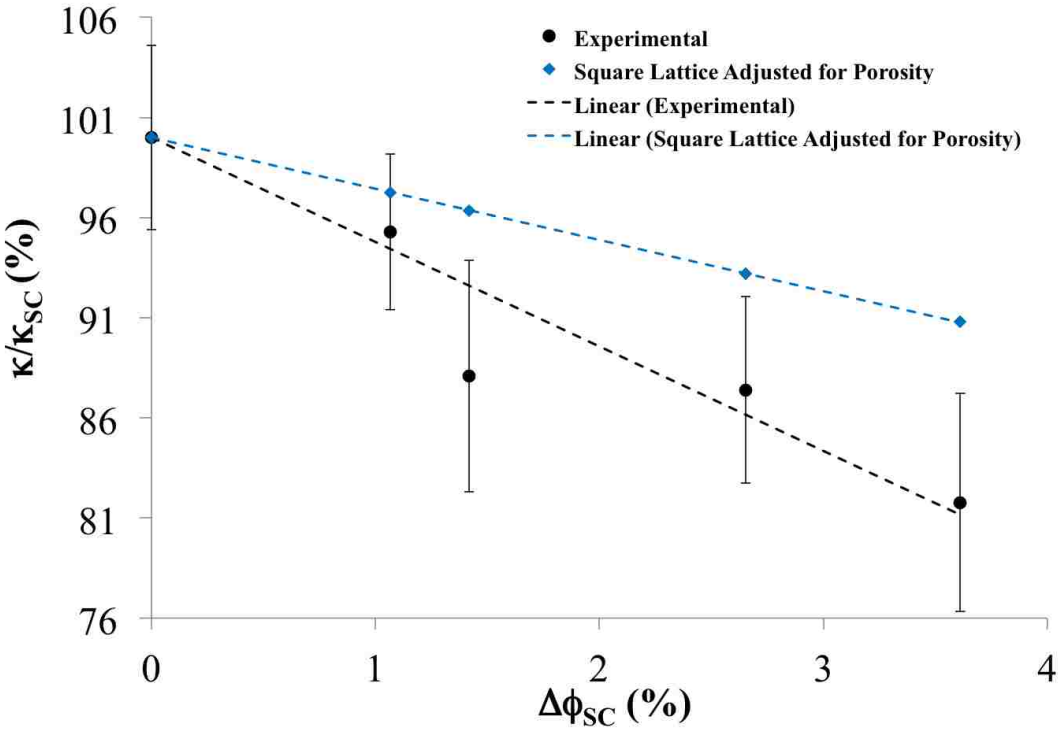

Figure 6.6: Experimental data normalized to the square lattice. Values adjusted by the porosity of the square lattice are shown as blue diamonds. Measured values (black circles) with their respective error are also plotted.

Results from the simulations are shown in **Figure 6.7**, and the open blue circles represent them. The "Hybrid Model Theory" results take porosity, diffuse boundary

scattering, and coherent scattering into account. The coherent scattering comes from the modified phonon dispersion of the various supercells, and the incoherent scattering is accounted for in the phonon scattering relaxation time, τ. For these results, the effect of coherence is over-estimated. Additional simulations will account for total incoherent scattering and porosity only while other simulations will account for pure coherent scattering and porosity. These combined results will help provide additional insight into the strength of each scattering type. Regardless of these simulations, it is already evident that coherent scattering plays a role in the thermal conductivity of PnCs.

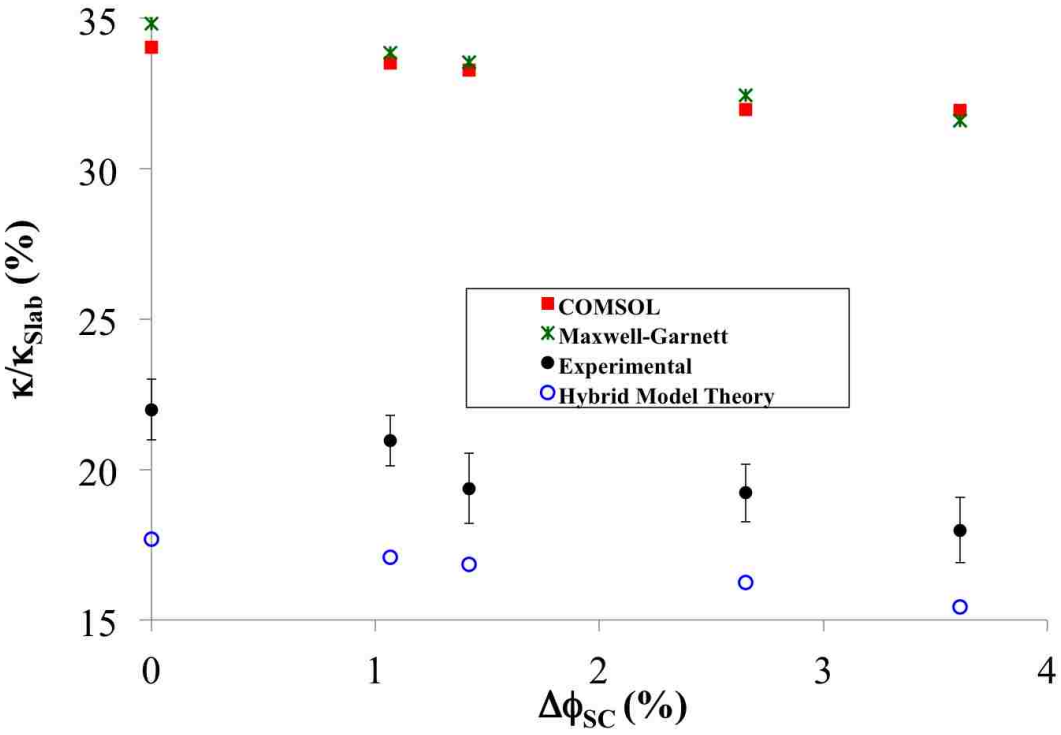

Figure 6.7: Comparison of theoretical models to experimental data. Open blue circles take into account both coherent and incoherent scattering, and the results overshoot by ~ 5%.

In a recent paper that looked at thermal transport in nanostructures and low-dimensional systems, it was stated that diffuse scattering by random interface roughness in a phononic crystal can potentially destroy the phase coherence required for phononic bandgap formation [77]. It is certainly true that diffuse scattering is occurring in these

fabricated PnCs, but the intent of the PnC is not to introduce a bandgap. Rather, the intent of the PnCs was to alter the phonon dispersion of silicon using various unit cells. In this experiment the unit cells were designed to preserve incoherent scattering by keeping the critical length constant. By using different unit cells, the amount of coherent scattering could be altered without affecting incoherent scattering. This allowed the impact of coherent scattering to be observed independently of incoherent scattering.

One may argue that it is unlikely for the PnCs fabricated in this work to significantly alter silicon's thermal conductivity based on the fact that high frequency phonons are the main carriers of heat energy through a semiconductor. Recent work, though, is showing that long wavelength phonons play an important role in heat transport [21, 38]. In reference 38, low-frequency, long-*mfp* phonons were estimated to carry 70% of the total thermal conductivity. This indicates it is highly probable for lower frequency, longer wavelength phonons to significantly alter a material's thermal conductivity.

The impact of the parameters c and ϕ are shown in **Figure 6.4**, **Figure 6.5**, and **Figure 6.6**, but they alone cannot predict the measured thermal conductivity values for the fabricated phononic crystals. As a reminder, all five unit cells were designed to have equal or similar critical lengths and porosities, in order to single out the effect of the unit cell on thermal conductivity. Deviations of the measured results from a purely incoherent scattering picture stem from the use of different unit cells. Each unit cell has a unique periodicity that alters the phonon dispersion in Si, and the differences arise because of the coherent scattering in each unit cell. If only incoherent scattering affected thermal conductivity, then the choice of the unit cell would not affect the thermal conductivity of PnCs beyond any differences in c or ϕ. The choice, however, does affect heat transfer

through the PnC. This means coherent phonon scattering does exist, and this work provides definitive evidence for its existence. This does not mean coherent scattering dominates thermal conductivity in phononic crystals. Incoherent scattering certainly plays a role in determining thermal conductivity, but it alone cannot explain the measurements in this work. Both coherent and incoherent scattering are required.

7. Conclusion

The work in this dissertation focused on investigating the existence of coherent phonon scattering in silicon. Since heat conduction in silicon is dominated by phonons, changes in Si's thermal conductivity were used to investigate the existence of coherent phonon scattering. Altering Si's thermal conductivity was accomplished by generating various periodic patterns in the Si. For these periodic patterns, the incoherent scattering strength was kept constant, and only coherent scattering was varied. The strength of incoherent scattering was directly related to the critical length. Keeping this constant kept incoherent effects equal among the various PnCs. Coherent scattering was varied by the use of five different 2D crystals. If incoherent scattering were the only kind of scattering present in a phononic crystal, then the use of different patterns (different unit cells) would not affect Si's thermal conductivity beyond any differences in critical length, porosity, or surface area. If coherent scattering did occur in Si/Air PnCs, then the fact that periodicity is present would alter the phonon propagation through the material.

Five different unit cells of Si/Air vias were used for the investigation. Dimensions for the unit cells were based on previous work that provided evidence for the existence of coherent scattering in Si. The critical length was also based on the estimated mean free path of phonons in Si at room temperature. Modeling of the various silicon structures employed a hybrid lattice dynamics-continuum mechanics technique. With this technique it was shown that the presence of the unit cells significantly altered the density-of-states in Si. By altering Si's density-of-states, which affects Si's thermal

conductivity, it was possible to measure the thermal conductivity of the various PnCs and use that information to look at coherent scattering in Si. Having different unit cells was not enough. The unit cells needed to have similar, if not equal, parameters such as critical length and porosity. Achievement of this came through the use of a 2D square lattice of vias in Si with a varying number of smaller vias located along the diagonal of the unit cell.

Fabrication of all five unit cells with less than 10 nm variation in their critical lengths was successfully achieved with a focused ion beam. The use of a hard, Ti protective layer protected the Si from Ga implantation during fabrication. By using a hard-on-soft technique, a 3° sidewall slope of the vias was achieved.

Thermal conductivity measurements of the PnCs used a micro-fabricated suspended island platform. Since the PnCs were not co-fabricated with the measurement platforms, the PnCs were attached to the platforms with FIB deposited Pt. Each PnC sample included three paths for the heat to travel. This provided a method by which the contribution of the platform legs and contact resistance could be subtracted from thermal conductivity measurements.

All of the PnCs showed a significant reduction in the thermal conductivity of Si. Incoherent scattering alone could not predict the observed reduction in thermal conductivity. Besides not being able to predict the overall reduction, incoherent scattering could not explain the relative thermal conductivity differences observed among the five unit cells which had nearly identical critical lengths, porosities, and surface areas. Based on the relative thermal conductivity measurements of five different unit cells with

the similar critical lengths, surface areas, and porosities, coherent phonon scattering is a real phenomenon that occurs in silicon.

8. Bibliography

1. Miyashita, T., Sonic crystals and sonic wave-guides. *Measurement Science and Technology* **16**, R47-R63 (2005).
2. Khelif, A., Choujaa, A. & Benchabane, S., Guiding and bending of acoustic waves in highly confined phononic crystal waveguides. *Applied Physics Letters* **84** (22), 4400-4402 (2004).
3. Olsson, R. H. I., El-Kady, I., Su, M., Tuck, M. & Fleming, J., *Microfabricated VHF acoustic crystals and waveguides*, presented at Transducers 2007, 2007.
4. Espinosa, F. & Jiménez, E. T. M., Ultrasonic Band Gap in a Periodic Two-Dimensional Composite. *Physical Review Letters* **80** (6), 1208-1211 (1998).
5. Vasseur, J. O. *et al.*, Phononic crystal with low filling fraction and absolute acoustic band gap in the audible frequency range: A theoretical and experimental study. *Physical Review E* **65**, 056608(6) (2002).
6. Soliman, Y. *et al.*, Phononic crystals operating in the gigahertz range with extremely wide band gaps. *Applied Physics Letters* **97**, 193502(3) (2010).
7. Mohammadi, S., Eftekhar, A. A., Hunt, W. D. & Adibi, A., High-Q micromechanical resonators in a two-dimensional phononic crystal slab. *Applied Physics Letters* **94**, 051906(3) (2009).
8. Goettler, D. *et al.*, Realizing the frequency quality factor product limit in silicon via compact phononic crystal resonators. *JOURNAL OF APPLIED PHYSICS* **108**, 084505(5) (2010).
9. Ziaei-Moayyed, M., Su, M., Reinke, C., I., E.-K. & Olsson, R. H. I., *SILICON CARBIDE PHONONIC CRYSTAL CAVITIES FOR MICROMECHANICAL RESONATORS*, presented at MEMS 2011, Cancun, Mexico, 2011.
10. Yang, S. *et al.*, Focusing of Sound in a 3D Phononic Crystal. *Physical Review Letters* **93** (2), 024301(4) (2004).
11. Torrent, D. & Sánchez-Dehesa, J., Acoustic cloaking in two dimensions: a feasible approach. *New Journal of Physics* **10** (2008).
12. Hsu, F.-C., Hsu, J.-C., Huang, T.-C. & Wang, C.-H., Reducing support loss in micromechanical ring resonators using phononic band-gap structures. *JOURNAL OF PHYSICS D: APPLIED PHYSICS* **44**, 375101(10) (2011).
13. Olsson, R. H. *et al.*, *Ultra High Frequency (UHF) Phononic Crystal Devices Operating in Mobile Communication Bands* , presented at Tech. Dig. IEEE Intl. Ultrasonics Symposium, 2009.
14. El-Kady, I., Olsson, R. H. I. & Fleming, J. G., Phononic band-gap crystals for radio frequency communications. *Applied Physics Letters* **92**, 233504(3) (2008).
15. Hopkins, P. E. *et al.*, Reduction in the Thermal Conductivity of Single Crystalline Silicon by Phononic Crystal Patterning. *NanoLetters* **11**, 107-112 (2011).
16. Yu, J.-K., Mitrovic, S., Tham, D., Varghese, J. & Heath, J., Reduction of thermal conductivity in phononic nanomesh structures. *Nature Nanotechnology* **5**, 718-721

(2010).

17. Kim, B. *et al.*, *Thermal Conductivity Manipulation in Single Crystal Silicon via Lithographically Defined Phononic Crystals*, presented at IEEE MEMS 2012, Paris, France, 2012.
18. Marconnet, A. M., Kodama, T., Asheghi, M. & Goodson, K. E., Phonon Conduction in Periodically Porous Silicon Nanobridges. *Nanoscale and Microscale Thermophysical Engineering* **16** (4), 199-219 (2012).
19. Weber, L. & Gmelin, E., Transport Properties of Silicon. *Applied Physics A* **53**, 136-140 (1991).
20. El-Kady, I. *et al.*, SAND Report, 2012.
21. Rowe, D. M. ed., *Thermoelectrics Handbook: Macro to Nano* (CRC Press, 2006).
22. Snyder, J. G. & Toberer, E. S., Complex thermoelectric materials. *Nature Materials* **7**, 105-114 (2008).
23. Kittel, C., *Introduction to Solid State Physics*, 6th ed. (John Wiley & Sons, 1986).
24. Lou, L.-f., *Introduction to Phonons and Electrons*, 1st ed. (World Scientific, Singapore, 2003).
25. Reinke, C. *et al.*, Thermal conductivity prediction of nanoscale phononic crystal slabs using a hybrid lattice dynamics-continuum mechanics technique. *AIP Advances* **1** (4), 041403-1-041403-14 (2011).
26. Tien, C.-L., Majumdar, A. & Gerner, F. M. eds., *Microscale Energy Transport* (Taylor & Francis, Washington, 1998).
27. Ju, Y. S. & Goodson, K. E., Phonon scattering in silicon films with thickness of order 100 nm. *Applied Physics Letters* **74** (20), 3005-3007 (1999).
28. Song, D. & Chen, G., Thermal conductivity of periodic microporous silicon films. *Applied Physics Letters* **84** (5), 687-689 (2004).
29. Yang, F. & Dames, C., Mean free path spectra as a tool to understand thermal conductivity in bulk and nanostructures. *Physical Review B* **87** (3), 035437(12) (2013).
30. Asheghi, M., Kurabayashi, K., Kasnavi, R. & Goodson, K. E., Thermal conduction in doped single-crystal silicon films. *Journal of Applied Physics* **91** (8), 5078-5088 (2002).
31. Glassbrenner, C. J. & Slack, G. A., Thermal Conductivity of Silicon and Germanium from 3K to the Melting Point*. *Physical Review* **134** (4A), A1058-A1069 (1964).
32. Wada, H. & Takeshi, K., Thermal Conductivity of Amorphous Si. *Japanese Journal of Applied Physics* **35**, L-648-L650 (1996).
33. Morin, F. J. & Maita, J. P., Electrical Properties of Silicon Containing Arsenic and Boron. *Physical Review* **96** (1), 28-35 (1954).
34. Liu, W. & Asheghi, M., Thermal conduction in ultrathin pure and doped single-crystal silicon layers at high temperatures. *Journal of Applied Physics* **98** (12) (2005).
35. McGaughey, A. J. & Jain, A., Nanostructure thermal conductivity prediction by Monte Carlo sampling of phonon free paths. *Applied Physics Letters* **100** (6), 061911(3) (2012).

36. Chen, G., *Nanoscale Energy Transport and Conversion* (Oxford University Press, New York, 2005).
37. Hopkins, P. E., Rakich, P. T., Olsson, R. H. I., El-Kady, I. F. & Phinney, L. M., Origin of reduction in phonon thermal conductivity of microporous solids. *Applied Physics Letters* **95** (2009).
38. Luckyanova, M. N. *et al.*, Coherent Phonon Heat Conduction in Superlattices. *Science* **338**, 936-939 (2012).
39. Ma, J. *et al.*, Coherent Phono-Grain Boundary Scattering in Silicon Inverse Opals. *NanoLetters* **13** (2), 618-624 (2013).
40. Li, D. *et al.*, Thermal conductivity of individual silicon nanowires. *Applied Physics Letters* **83** (14), 2934-2936 (2003).
41. Dames, C. & G., C., in *Thermoelectrics Handbook: Micro to Nano*, edited by Rowe, D. (CRC Press, 2006), Vol. II, pp. 42-1-42-16.
42. Russell, H. W., Principles of Heat Flow in Porous Insulators. *Journal of the American Ceramic Society* **18** (1935).
43. Eucken, A. *Forschung auf dem Gebiete des Ingenieurwesens* **Ausgabe B** (Band 3), 353 (1932).
44. Nan, C.-W., Birringer, R., Clarke, D. R. & Gleiter, H., Effective Thermal Conductivity of Particulate Composites with Interfacial Thermal Resistance. *Journal of Applied Physics* **81** (10), 6629-6699 (1997).
45. FEI (2003).
46. Holldand, M. G., Analysis of Lattice Thermal Conductivity. *Physical Review* **132** (6), 2461-2471 (1963).
47. Callaway, J., Model for Lattice Thermal conductivity at Low Temperatures. *Physical Review* **113** (N), 1046-1051 (1959).
48. Davis, B. & Hussein, M., Thermal characterization of nanoscale phononic crystals using supercell lattic edynamics. *AIP Advances* **1**, 041701(15) (2011).
49. Hochbaum, A. *et al.*, Enhanced thermoelectric performance of rough silicon nanowires. *Nature* **451**, 163-168 (2008).
50. Shi, L. *et al.*, Measuring Thermal and Thermoelectric Properties of One-Dimensional Nanostructures Using a Microfabricated Device. *Journal of Heat Transfer* **125** (5), 881-888 (2003).
51. Prewett, P. & Jefferies, D., Characteristics of a gallium liquid metal field emission ion source. *Journal of Physics D: Applied Physics* **13** (9), 1747-1755 (1980).
52. Orloff, J. ed., *Charged Particle Optics*, 2nd ed. (CRC Press, 2009).
53. Ziegler, J. F., Biersack, J. P. & Ziegler, M. D., *SRIM The Stopping and Range of Ions in Matter*.
54. MoberlyChan, W. J., Felter, T. E. & Wall, M. A., Surface Rippling & Ion Etch Yields of Diamond Using a Focused Ion Beam: With or Without Enhanced-Chemistry, Aspect Ratio Regulates Ion Etching. *Microscopy Today* **14** (6), 28-34 (2006).
55. Ray, V. & N., A., *FIB imaging and High Aspect Ratio endpointing for advanced circuit modification system*, presented at EFUG 2002, Rimini, Italy, 2002.

56. Ray, V., *Fluorocarbon Precursor for High Aspect Ratio Via Milling in Focused Ion Beam Modification of Integrated Circuits*, presented at 30th International Symposium for Testing and Failure Analysis, Worcester, Massachusetts, 2004.
57. Su, M. F., Olsson, R. H., Leseman, Z. C. & El-Kady, I., Realization of a phononic crystal operating at gigahertz frequencies. *Applied Physics Letters* **96**, 053111 (2010).
58. Goettler, D. *et al.*, Realization of a 33 GHz phononic crystal fabricated in a freestanding membrane. *AIP ADVANCES* **1** (4) (2011).
59. Leseman, Z. C., Koppaka, S. B. & Mackin, T. J., A Fracture Mechanics Description of Stress-Wave Repair in Stiction-Failed Microcantilevers: Theory and Experiments. *Journal of Microelectromechanical Systems* **16** (2007).
60. Leseman, Z. C., Carlson, S. P. & Mackin, T. J., Experimental Measurements of the Strain Energy Release Rate for Stiction-Failed Microcantilevers Using a Single-Cantilever Beam Peel Test. *Journal of Microelectromechanical Systems* **16**, 38-43 (2007).
61. Delrio, F. W. *et al.*, The Role of van der Waals Forces in Adhesion of Micromachined Surfaces. *Nature Materials* **4**, 629-634 (2005).
62. Goettler, D., Thesis, 2008.
63. Linares, L. C. & Li, S. S., An Improved Model for Analyzing Hole Mobility and Resistivityin p-Type Silicon Doped with Boron, Gallium, and Indium. *Journal of The Electrochemical Society* **128** (3), 601-608 (1981).
64. FEI, Quanta 3D FEG User Opeartion Manual (2008).
65. Chen, G., Size and Interface Effects on Thermal Conductivity of Superlattices and Periodic Thin-Film Structures. *Journal of Heat Transfer* **119**, 220-229 (1997).
66. Hopkins, P., Phinney, L., Serrano, J. & Beechem, T., Effects of surface roughness and oxide layer on the thermal boundary conductance at aluminum/silicon interfaces. *Physical Review B* **82** (8), 085307(5) (2010).
67. Alaie, S., Goettler, D. F.., Abbas, K., El-Kady, I. & Leseman, Z. C., Microfabricated Suspended Island Platform for the Measurement of In-Plane Thermal Conductivity of Thin Films and Nanostructured Materials with Consideration of Contact Resistance. *Review of Scientific Instruments* (Submitted).
68. Shi, L., PhD Thesis, 2001.
69. Kim, P., Shi, L., Majumdar, A. & P, M., Thermal Transport Measurements of Individual Multiwalled Nanotubes. *Physical Review Letters* **87** (21), 2155021-2155024 (2001).
70. Choi, S. R., Kim, D., Choa, S., Lee, S. & Kim, J., Thermal Conductivity of AlN and SiC Thin Films. *International Journal of Thermophysics* **27** (3), 896-905 (2006).
71. Sultan, R., Avery, A. D., Stiehl, G. & Zink, B. L., Thermal conductivity of micromachined low-stress silicon-nitride beams from 77 to 325 K. *Journal of Applied Physics* **105**, 043501(7) (2009).
72. International Electrotechnical Comission, Standard.
73. Zhang, X. *et al.*, Thermal and electrical conductivity of a suspended platinum nanofilm. *Applied Physics Letters* **86**, 1719121-1719123 (2005).

74. Asheghi, M., Leung, Y. K., Wong, S. S. & Goodson, K. E., Phonon-boundary scattering in thin silicon layers. *Applied Physics Letter* **71** (13), 1798-1790 (1997).
75. Prasher, R., Transverse thermal conductivity of porous materials made from aligned nano- and microcylindrical pores. *Journal of Applied Physics* **100** (6), 064302(7) (2006).
76. Ziman, J. M., *Electrons and Phonons* (Oxford University Press, 1960).
77. Shi, L., Thermal and Thermoelectric Transport in Nanostructures and Low-Dimensional System. *Nanoscale and Microscale Thermophysical Engineering* **16** (2), 79-116 (2012).